

# **Fabrication and Characterization of CuInSe<sub>2</sub>/CdS/ZnO Thin Film Solar Cells**

by

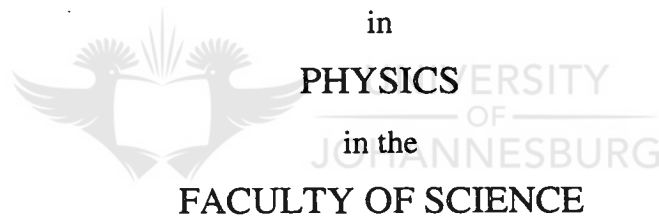
Manuel Luis Chenene

**DISSERTATION**

submitted in the fulfillment of the  
requirements for the degree

**MAGISTER SCIENTIAE**

in



FACULTY OF SCIENCE

at the

**RAND AFRIKAANS UNIVERSITY**

Supervisor: Professor V. Alberts

Co-Supervisor: Professor R. Swanepoel

June 1999

## ACKNOWLEDGEMENTS

My grateful thanks to:

- My supervisors, Professor V. Alberts and Professor R. Swanepoel for their guidance and advice.
- My supervisor at Eduardo Mondlane University – Maputo, Professor B. Cuamba for his valuable discussions and comments during this study.
- Professor M.J. Witcomb of the University of the Witwatersrand for his assistance with SEM studies.
- Professor E. Bucher of the University of Konstanz for making their research facilities available to me.
- M. Klenk, O. Schenker, S. Kühne and J.H. Schön of the University of Konstanz for their assistance with characterization techniques.
- My fiancé Olga for her patience and support.
- My parents, Luis and Maria and brothers for their support and encouragement.
- The Solar Energy Research Programme, Department of Physics, Faculty of Sciences of the Eduardo Mondlane University for their advice and support.
- The Capacity Building Project, Credit 2436 (World Bank Project) at the Eduardo Mondlane University and the SIDA/SAREC for their financial support.

**I thank God for standing by me.**

# CONTENTS

	Page
ACKNOWLEDGEMENTS	
ABSTRACT	
SAMEVATTING	
LIST OF FIGURES	
LIST OF TABLES	
<b>CHAPTER1</b>	
INTRODUCTION	01
<b>CHAPTER 2</b>	
THIN FILM SOLAR CELLS DEVICES BASED ON CuInSe <sub>2</sub>	04
2.1 Introduction	04
2.2 Design and Fabrication of CuInSe <sub>2</sub> Based Solar Cell Devices	05
2.3 Advantage of Chalcopyrite Thin Films for Photovoltaic Applications	07
2.4 Material Properties of Ternary Chalcopyrite Semiconductor Thin Films	10
2.4.1 Introduction	10
2.4.2 Structural Properties of Ternary Chalcopyrite Semiconductors	10
2.4.3 Optical Properties of Ternary Chalcopyrite Semiconductors	13
2.4.4 Electrical Properties of Ternary Chalcopyrite Semiconductors	15
2.5 Preparation Methods for CuInSe <sub>2</sub>	16
2.5.1 Introduction.	16
2.5.2 Deposition Technologies	16
2.5.3 Diffusion and Reaction Kinetics of CuInSe <sub>2</sub> Film Growth	19
2.6 Semiconducting Transparent Thin Films	21
2.6.1 Introduction	21
2.6.2 Basic Properties of CdS and ZnO	21
References	23

## CHAPTER 3

FUNDAMENTAL PRINCIPLES OF SOLAR CELL DEVICES	26
3.1 Introduction	26
3.2 Outline of Solar Cell Development	26
3.3 Physical Principle of Sunlight Radiation	27
3.3.1 Physical Source of Sunlight	27
3.3.2 The Solar Constant	28
3.3.3 Solar Intensity at the Earth's Surface	29
3.4 <i>p-n</i> Junction Diodes and Solar Cell Parameters	31
3.4.1 Introduction	31
3.4.2 Electrostatics of <i>p-n</i> Junctions	31
3.4.3 Carrier Injection	35
3.4.4 Dark Characteristics	38
3.4.5 Solar Cell Output Parameters	43
3.5 Efficiency Limits	45
3.5.1 Introduction	45
3.5.2 Short-Circuit Current	45
3.5.3 Open-Circuit Voltage and Efficiency	47
3.6 Efficiency Losses	49
3.6.1 Introduction	49
3.6.2 Short-Circuit Current Losses	49
3.6.3 Open-Circuit Voltage Losses	50
3.6.4 Fill Factor Losses	52
References	55

## CHAPTER 4

EXPERIMENTAL PROCEDURES	56
4.1 Introduction	56
4.2 Substrate Preparation	56
4.3 Molybdenum Deposition	57
4.4 Absorber Formation	57

4.4.1	Precursor Formation	57
4.4.2	Selenization Processes	61
4.4.2.1	Selenization in elemental Se vapour	61
4.4.2.2	Selenization in H <sub>2</sub> Se/Ar gas	62
4.4.2.3	Rapid thermal processing (RTP)	64
4.5	Device Fabrication	64
4.5.1	CdS Buffer Layer Deposition	64
4.5.2	ZnO Window Layer Deposition	66
4.5.3	Ni/Al Front Contact Deposition	67
4.6	Characterization Techniques	67
4.6.1	Introduction	67
4.6.2	Structural Analysis	68
4.6.2.1	Introduction	68
4.6.2.2	Scanning Electron Microscopy (SEM)	68
4.6.2.3	Energy Dispersive X-Ray Spectroscopy (EDS) and X-Ray Fluorescence (XRF)	71
4.6.2.4	X-Ray Diffraction (XRD)	73
4.6.3	Optical Characterization	74
4.6.3.1	Introduction	74
4.6.3.2	Infrared Spectroscopy	74
4.6.3.3	Photoluminescence	76
4.6.4	Electrical Characterization	79
4.6.4.1	Introduction	79
4.6.4.2	Four-Point Probe	79
4.6.4.3	Hall Effect Measurements	81
4.6.5	Device Characterization	82
	References	84

## CHAPTER 5

RESULTS AND DISCUSSION	85
------------------------	----

5.1 Introduction	85
------------------	----

<b>5.2</b>	<b>Material Properties of CuInSe<sub>2</sub></b>	<b>85</b>
<b>5.2.1</b>	<b>Introduction</b>	<b>85</b>
<b>5.2.2</b>	<b>Structural Properties of Precursor Films</b>	<b>86</b>
<b>5.2.3</b>	<b>Structural Properties of Reacted Precursor Films</b>	<b>91</b>
<b>5.2.3.1</b>	<b>Reaction of metallic precursors to an elemental Se vapour</b>	<b>91</b>
<b>5.2.3.2</b>	<b>Reaction of metallic precursors to H<sub>2</sub>Se/Ar</b>	<b>103</b>
<b>5.2.3.3</b>	<b>Rapid thermal treatment (RTP) of metallic Alloys</b>	<b>107</b>
<b>5.2.4</b>	<b>Optical and Electrical Properties of CuInSe<sub>2</sub> Absorber Films</b>	<b>110</b>
<b>5.2.4.1</b>	<b>Introduction</b>	<b>110</b>
<b>5.2.4.2</b>	<b>Influence of film composition on the optical and electrical properties</b>	<b>110</b>
<b>5.3</b>	<b>Growth and Characterization of CdS and ZnO</b>	<b>114</b>
<b>5.3.1</b>	<b>Introduction</b>	<b>114</b>
<b>5.3.2</b>	<b>Optimization of CdS Layer Thicknesses</b>	<b>114</b>
<b>5.3.3</b>	<b>ZnO Material Properties</b>	<b>120</b>
<b>5.3.3.1</b>	<b>Introduction</b>	<b>120</b>
<b>5.3.3.2</b>	<b>Structural Properties</b>	<b>120</b>
<b>5.3.3.3</b>	<b>Electrical Properties</b>	<b>125</b>
<b>5.3.3.4</b>	<b>Optical Characterization</b>	<b>127</b>
<b>5.3.4</b>	<b>Optimization of CdS/ZnO Window Layer Material</b>	<b>131</b>
<b>5.3.4.1</b>	<b>Introduction</b>	<b>131</b>
<b>5.3.4.2</b>	<b>Optical Properties</b>	<b>131</b>
<b>5.3.4.3</b>	<b>Electrical Properties</b>	<b>132</b>
<b>5.4</b>	<b>Device Fabrication</b>	<b>132</b>
	<b>References</b>	<b>134</b>

## **CHAPTER 6**

<b>CONCLUSIONS AND SUGGESTIONS FOR FUTURE WORK</b>	<b>135</b>
--	------------

## Abstract

I-III-VI<sub>2</sub> compound semiconductors are important photovoltaic (PV) materials with optical and electrical properties that can be tuned for optimum device performance. Recent studies indicated that the efficiencies ( $\eta > 18\%$ ) of CuInSe<sub>2</sub>/CdS/ZnO thin film devices are in good agreement with that of standard silicon cells. In this study, CuInSe<sub>2</sub> absorber films with excellent material properties were produced by relatively simple and reproducible two-stage growth techniques. In these approaches, metallic precursors (Cu/InSe, InSe/Cu, Cu/InSe/Cu and InSe/Cu/InSe) were deposited by thermal evaporation from specially designed graphite heaters at temperatures around 200°C. In the second stage of the process, the alloys were exposed to elemental Se vapour or H<sub>2</sub>Se/Ar gas. A systematic study was conducted in order to determine optimum growth parameters for the different deposition processes. Optimum material properties (homogeneous and dense films with a high degree of compositional uniformity) were obtained when InSe/Cu/InSe precursors were selenized in elemental Se vapour or H<sub>2</sub>Se/Ar gas. Comparative studies also indicated that the reaction kinetics is enhanced when H<sub>2</sub>Se/Ar is used as chalcogen source. Fully selenized films were obtained at temperatures as low as 450°C in a H<sub>2</sub>Se/Ar atmosphere, compared to temperatures of 600°C in the case of Se vapour. The optical and electrical properties of the absorber layers were accurately controlled by small variations in the bulk composition of the films. A standard CdS/ZnO window layer technology was also developed in our laboratories and preliminary solar cell devices were fabricated and evaluated.

## Samevatting

I-III-VI<sub>2</sub> saamgestelde halfgeleiers is belangrike fotovoltaiëse (PV) materiale met optiese en elektriese eienskappe wat aangepas kan word vir optimale toestelwerksverrigting. Onlangse studies het getoon dat die doeltreffendhede ( $\eta > 18\%$ ) van CuInSe<sub>2</sub>/CdS/ZnO dunlagiesonselle in goeie ooreenstemming is met die van die standaard silikonsonsele. In hierdie studie is CuInSe<sub>2</sub>-absorpsielagies met uitstaande materiaaleienskappe gekweek deur middel van relatief eenvoudige en reproduseerbare tweestap-groeiprosesse. In hierdie prosesse is metaalalloeie (Cu/InSe, InSe/Cu, Cu/InSe/Cu en InSe/Cu/InSe) vanaf spesiaal ontwerpte grafietverhitters by temperature rondom 200°C termies opgedamp. Tydens die tweede fase van die proses is die metaalalloeie blootgestel aan elementêre Se damp en H<sub>2</sub>Se/Ar gas. 'n Sistematiese studie is onderneem om optimale groeiparameters te bepaal vir die verskillende deposisieprosesse. Optimale materiaaleienskappe (homogene en digte lagies met 'n hoë graad van uniformiteit in komposisie) is verkry wanneer InSe/Cu/InSe-alloeie geseleniseer is in Se damp of H<sub>2</sub>Se/Ar gas. Vergelykende studies het egter getoon dat die reaksiekinetika versnel wanneer H<sub>2</sub>Se/Ar gas as bron van selenium gebruik word. Volledig geseleniseerde lagies is by temperature so laag as 450°C in 'n H<sub>2</sub>Se/Ar atmosfeer verkry, in teenstelling met temperature van 600°C in die geval van Se damp. Die optiese en elektriese eienskappe van die absorpsielagies is akkuraat deur klein veranderinge in die komposisie van die lagies beheer. 'n Standaard CdS/ZnO-vensterlagie tegnologie is verder in ons laboratorium ontwikkel en voorlopige sonselle is vervaardig en geëvalueer.



## LIST OF FIGURES

- Figure 2.1: Schematic representation of a typical  $\text{CuInSe}_2$ -based solar cell device
- Figure 2.2: Band gap versus lattice constant for various chalcopyrite semiconductors.
- Figure 2.3: Absorption spectrum of  $\text{CuInSe}_2$  compared with other photovoltaic semiconductors.
- Figure 2.4: Crystal structures of (a) zinc-blende lattices and (b) chalcopyrite.
- Figure 2.5:  $\text{Cu}_2\text{Se}-\text{In}_2\text{Se}_3$  pseudobinary phase diagram.
- Figure 2.6: The wurtzite lattice of  $\text{ZnO}$ .
- Figure 3.1: Planckian black-body radiation distributions for different black-body temperatures.
- Figure 3.2: Principal features of the sun.
- Figure 3.3: Spectral distribution of sunlight.
- Figure 3.4: Isolated pieces of  $p$ -type and  $n$ -type semiconductor material with corresponding energy-band diagrams.
- Figure 3.5:  $p$ - $n$  junction formed by bringing the isolated  $p$ -type and  $n$ -type regions together. Also shown is the corresponding energy-band diagram at thermal equilibrium.
- Figure 3.6: Plot of the natural logarithms of the electron and hole concentrations corresponding to Fig. 3.5.
- Figure 3.7: (a) Space-charge density corresponding to Fig. 3.6.
- Figure 3.8: Plot of carrier concentrations when a voltage is applied to the  $p$ - $n$  junction.
- Figure 3.9: (a) Linear plot of the distributions of carriers throughout the  $p$ - $n$  junction diode under forward bias. (b) Corresponding semilogarithmic plot.
- Figure 3.10: (a) Minority-carrier current densities in a  $p$ - $n$  junction diode corresponding to Fig. 3.9. (b).
- Figure 3.11: Terminal properties of a  $p$ - $n$  junction diode in the dark and when illuminated.
- Figure 3.12: Ideal value of the fill factor as a function of the open-circuit voltage normalized to the thermal voltage,  $kT/q$ .
- Figure 3.13: (a) Photon flux in sunlight corresponding to the AM0 and AM1.5 energy distributions given in Fig. 3.3.

- Figure 3.14: Solar cell efficiency limits as a function of the band gap of the cell material.
- Figure 3.15: One of the major loss mechanisms in solar cells.
- Figure 3.16: Major features of a solar cell. Dimensions in the vertical direction are exaggerated compared to lateral dimensions for the purposes of illustration.
- Figure 3.17: Semilogarithmic plots of the dark current-voltage characteristics of a  $p-n$  junction diode in the dark, including the effect of recombination in the depletion region.
- Figure 3.18: Equivalent circuit of a solar cell.
- Figure 3.19: Effect of parasitic resistances on the output characteristics of solar cells.
- Figure 3.20: General curves for solar cell fill factors as a function of normalized open-circuit voltage.
- Figure 4.1: Evaporation system used in this study for the deposition of precursor alloys.
- Figure 4.2: Representation of the (a) substrate heater, (b) cylindrical-shaped evaporation sources and (c) stainless steel effusion cell which are important components of the vacuum system used in this study.
- Figure 4.3: Schematic representation of the precursor films deposited in this study.
- Figure 4.4: Representation of the stainless steel effusion cell which was used to create an uniform elemental selenium flux in vacuum.
- Figure 4.5:  $H_2Se/Ar$  reaction furnace used in this study for selenization of metallic precursors.
- Figure 4.6: Basic configuration of the DC magnetron sputtering unit used in this study for ZnO sputtering.
- Figure 4.7: Schematic of the scanning electron microscope.
- Figure 4.8: (a) Electron and photon signals emanating from tear-shaped interaction volume during electron-beam impingement on specimen surface. (b) Energy spectrum of electrons emitted from specimen surface. (c) Effect of surface topography on electron emission.
- Figure 4.9: Fourier transform infrared spectrometer schematic.
- Figure 4.10: Typical apparatus for photoluminescence measurements.
- Figure 4.11: Radiative transitions observed with photoluminescence.
- Figure 4.12: (a) Definition of resistivity and sheet resistance. (b) Four-point probe technique.

- Figure 4.13: The Hall effect phenomenon.
- Figure 4.14: Experimental configuration for testing solar cells and modules.
- Figure 5.1: SEM micrographs of a typical (a) Mo/InSe/Cu/InSe and (b) Mo/Cu/InSe/Cu precursor alloy.
- Figure 5.2: XRD patterns from (a) Mo/InSe/Cu, (b) Mo/Cu/InSe, (c) Mo/InSe/Cu/InSe and (d) Mo/Cu/InSe/Cu structures. The precursors were prepared at a substrate temperature of 200°C.
- Figure 5.3: SEM micrographs of CuInSe<sub>2</sub> films obtained by selenization of Mo/InSe/Cu or Mo/Cu/InSe/Cu precursors in Se vapour. The composition of this specific film is 22.39 at.% Cu, 26.13 at.% In and 51.48 at.% Se.
- Figure 5.4: XRD pattern from a selenized (in Se vapour at 600°C for 1h) precursor film in which the growth sequence was terminated with a Cu layer.
- Figure 5.5: SEM micrographs of a typical CuInSe<sub>2</sub> absorber film produced by treatment of a Mo/Cu/InSe bilayer in Se vapour at 600°C for minutes.
- Figure 5.6: XRD pattern obtained from a selenized Mo/Cu/InSe film in Se vapour.
- Figure 5.7: SEM micrographs of a typical CuInSe<sub>2</sub> film produced by reaction of a Mo/InSe/Cu/InSe precursor to Se vapour. The composition of this film is 23.21 at.% Cu, 26.10 at.% In and 50.69 at.% Se.
- Figure 5.8: Intensity versus mass per square of a repeatedly etched CuInSe<sub>2</sub> sample, prepared by the reaction of a Mo/InSe/Cu precursor to Se vapour. In (a) the K $\alpha$ <sub>1,2</sub> intensities are shown, while in (b) the L $\alpha$ <sub>1</sub> intensities. The variation in element concentration as function of total material mass is depicted in (c), while the variation in element concentration as function of total layer thickness is shown in (d).
- Figure 5.9: Intensity versus mass per square of a repeatedly etched CuInSe<sub>2</sub> sample, prepared by the reaction of a Mo/InSe/Cu/InSe precursor to Se vapour. In (a) the K $\alpha$ <sub>1,2</sub> intensities are shown, while in (b) the L $\alpha$ <sub>1</sub> intensities. The variation in element concentration as function of total material mass is depicted in (c), while the variation in element concentration as function of total layer thickness is shown in (d).
- Figure 5.10: SEM micrographs of a H<sub>2</sub>Se treated (at 450°C for 1h) Mo/InSe/Cu/InSe precursor.
- Figure 5.11: SEM micrographs of a H<sub>2</sub>Se treated (at 450°C for 1h) Mo/Cu/InSe/Cu precursor.
- Figure 5.12: XRD pattern obtained from a H<sub>2</sub>Se/Ar treated metallic precursor.

- Figure 5.13: Compositional uniformity of a typical  $\text{H}_2\text{Se}/\text{Ar}$  treated metallic precursor. The sample was repeatedly etched in bromium methanol, followed by XRF measurements.
- Figure 5.14: Morphological features of a rapid thermal treated metallic precursor.
- Figure 5.15: XRD patterns from a metallic precursor (a) prior to RTP treatment and (b) after RTP treatment.
- Figure 5.16: Composition versus total mass of material after different etching steps, followed by XRF measurements. The sample was prepared by RTP treatment of a metallic precursor alloy.
- Figure 5.17: PL spectra of a typical Cu-rich  $\text{CuInSe}_2$  sample. Measurements were carried out at 10K with 40 mW excitation power.
- Figure 5.18: PL spectra of various slightly In-rich  $\text{CuInSe}_2$  absorber films, prepared by the reaction of metallic precursors to Se vapour and  $\text{H}_2\text{Se}/\text{Ar}$ . Measurements were taken at 10K.
- Figure 5.19: Calculated transmission spectra for the system air/CdS/glass/CdS/air for various thicknesses of the CdS layers (thin lines). The heavy broken red lines are the experimental spectra for CdS films grown for different times.
- Figure 5.20: Transmission spectra of CdS films grown for different times with CBD on glass. The broken black line represents the spectrum of the glass substrate.
- Figure 5.21: SEM micrograph of an undoped ZnO film grown right under the centre of the target. In this figure  $1\mu\text{m}$  represents 1cm.
- Figure 5.22: SEM micrograph of an undoped ZnO film grown 80 mm away of the centre of the target. In this figure  $1\mu\text{m}$  represents 1cm.
- Figure 5.23: XRD patterns of ZnO films grown under the centre of target (A1), 50cm away from the target centre (A3) and about 80cm away from the target centre (A6).
- Figure 5.24: XRD patterns of ZnO films as function of different orientations in the plasma: F3 represents the flat position, the middle pattern the  $80^\circ$  orientation and the top pattern the  $90^\circ$  orientation (vertical).
- Figure 5.25: XRD patterns of ZnO layers grown at different substrate temperatures, from room temperature (N) up to  $200^\circ\text{C}$  (L).
- Figure 5.26: XRD patterns of ZnO films deposited right under the center of the target: unscreened (A1), screened (B1) and with external magnetic field (E1).
- Figure 5.27: Resistivity of samples grown in horizontal positions as function of distance from the center of the target. The data were collected by four-point probe measurements.

Figure 5.28: Transmission spectra of two undoped samples sputtered (a) directly under the target and (b) 30mm away from the centre of the erosion zone. The dotted red lines are the corresponding transmission spectra from clean glass substrates.

Figure 5.29: Transmission spectrum of a 2.5%  $\text{Al}_2\text{O}_3$ -doped ZnO film grown 30 mm away from the target center.

Figure 5.30: Refractive indices for undoped ZnO films deposited at a flat orientation are presented in graphs (a) and (b). The values for typical doped samples are shown in (c) and (d).

Figure 5.31: Optical band gap values for (a) undoped and (b) doped ZnO films.

Figure 5.32: Transmission spectrum of a CdS/ZnO window layer deposited on glass.



## LIST OF TABLES

- Table 2.1: Reported performances of laboratory-scale solar cells based on CuInSe<sub>2</sub> and its alloys.
- Table 2.2: Efficiencies of solar cell modules based on chalcopyrite thin films.
- Table 2.3: Summary of the important mechanical properties of CuInSe<sub>2</sub>.
- Table 2.4: Band gaps of ternary semiconductors and the difference  $\Delta E_G$  (band gap anomaly) with respect to the binary analogs.
- Table 2.5: Summary of the electrical properties of I-III-VI<sub>2</sub> compound semiconductors as function of material composition.
- Table 2.6: Examples of single-stage (SS) and two-stage (TS) processing methods for the growth of CuInSe<sub>2</sub> thin films and the corresponding efficiencies ( $\eta$ ) of solar cells fabricated on them.
- Table 2.7: Crystal structure of A<sup>II</sup> and B<sup>VI</sup> compounds.
- Table 4.1: Experimental details regarding the chemical and concentration of solutions used in the CBD process.
- Table 4.2: Summary of experimental parameters used during sputtering of ZnO.
- Table 5.1: Summary of CuInSe<sub>2</sub> X-ray diffraction data as shown in Fig. 5.6. For the purpose of comparison the theoretical expected values are also given.
- Table 5.2: Summary of the data obtained from an etched sample, followed by XRF measurements. The sample was prepared by reacting a Mo/InSe/Cu precursor to Se vapour at 600°C.

Table 5.3: Summary of the data obtained from an etched sample, followed by XRF measurements. The sample was prepared by reacting a Mo/InSe/Cu/InSe precursor to Se vapour at 600°C.

Table 5.4: Summary of composition and PL response from samples indicated in Fig. 5.18.

Table 5.5: Electrical properties of CuInSe<sub>2</sub> polycrystalline thin films as function of composition.

Table 5.6: Summary of the experimental CdS layer thicknesses for different deposition periods.

Table 5.6: Summary of the experimental CdS layer thicknesses for different deposition periods.

Table 5.7: Electrical parameters obtained from Hall measurements for ZnO samples as function of substrate temperature and orientation.

Table 5.8: Electrical data of CdS/ZnO window layer from Hall measurements.

Table 5.9: Summary of the performances from 3 cell structures.

# CHAPTER 1

## INTRODUCTION

Photovoltaic (PV) conversion of solar energy appears to be one of the most promising ways of meeting the increasing energy demands of the future in a time when conventional sources of energy are being depleted. In terms of human history, the life of the sun is effectively infinite, its energy is being radiated to the earth whether it is directly used or not, and the use of photovoltaics for direct conversion of solar energy introduces no direct contamination of the environment. Furthermore, it appears that major advances in the understanding and fabrication of semiconductor devices over the past 30 years have prepared the way for the kind of massive effort required if PV are to make a significant contribution to energy requirements of the future.

Despite rapid growth of the market, PV is still far from being an ideal energy source. High costs are presently the main obstacle for the world-wide generation of electrical power by PV cells. The first PV devices to have wide application were silicon single-crystal homojunction cells for utilization in the space program. The standard silicon technology has now been developed to an almost optimum efficiency and no further reduction in cost is therefore anticipated. Against this background, the majority of solar research programmes aim to develop high efficiency PV modules, which can be fabricated on large area substrates using low cost, high throughput processing technologies. As a result of these efforts, various promising materials such as I-III-VI<sub>2</sub> compound semiconductors, amorphous silicon and CdTe have been developed as absorber layers for high efficiency thin film solar cells. Although the basic physics of these thin-film devices are complex, they offer two important advantages: (i) because the required thickness of the active layers is of the order of two or three times the optical absorption length, the material cost remain a small part of the total cell cost, and (ii) the thin film configuration lends itself to large area, continuous flow processing.

Solid state devices based on copper indium diselenide (CIS) and its alloys have produced the highest efficiencies (> 18%) for any thin film solar cell. The material properties of these ternary compound semiconductors are complex and critically influence the device properties



of completed devices. A large number of vacuum and non-vacuum growth techniques are available to produce single-phase chalcopyrite thin films. In the highest efficient devices, the absorber films are produced by a single-stage co-evaporation process. This technique allows excellent control over the process parameters, but has several limitations for large scale applications. Two-stage growth processes have certain limitations in controlling the material quality of the CIS absorber films, but are very promising for large-scale applications. These important aspects, as well as other relevant focus areas of present research, are discussed in detail in **Chapter 2**.

In order to describe the properties and use of photovoltaic cells, it is important to consider the sequence of phenomena involved: from the radiation received from the sun, through the process of absorption of this radiation, generation and transport of charge carriers in the semiconductor, separation of charge by the junction, collection of these carriers at contacts to the device, and finally the criteria that controls the conversion efficiency of a solar cell device. These important theoretical aspects are summarized in **Chapter 3**.

An important part of this study was the development of a relatively simple and reproducible growth technique for the deposition of chalcopyrite thin films. This entailed the design of innovative growth systems, development of new growth schemes and optimization of process parameters. These important experimental details are dealt with in detail in **Chapter 4**. As important, was the accurate characterization of the semiconductor thin film. The structural, optical and electrical characterization techniques used in this study are also discussed in Chapter 4.

The experimental results that followed from this study are discussed in **Chapter 5**. Various growth schemes were considered during this study in order to produce device quality material. In each case a systematic study was conducted in order to determine optimum growth parameters. The quality of the CIS thin film absorbers was compared in terms of morphological properties, presence of secondary phases and the degree of compositional uniformity as function of sample depth. The optical and electrical properties of the films were evaluated as function of the bulk composition of the samples. Another important aim of this study was the development of a standard CdS/ZnO window layer technology in our laboratories. High quality CdS and ZnO films were deposited by means of a chemical bath

deposition process and DC magnetron sputtering, respectively. The structural, optical and electrical properties of these films were optimized for a given set of experimental parameters. Based on these fundamental studies we were able to produce preliminary solar cell devices.

Finally, in **Chapter 6** the results presented in Chapter 5 are summarized and final conclusions are drawn. Some suggestions for future research are also made in this Chapter.



## CHAPTER 2

### THIN FILM SOLAR CELLS DEVICES BASED ON $\text{CuInSe}_2$

#### 2.1 Introduction

For a number of years there has been considerable worldwide interest in the development of so-called thin film solar cells. Solar cell research programmes in general aim to develop high efficiency photovoltaic (PV) modules, which can be fabricated on large area, inexpensive substrates. These devices are typically fabricated on polycrystalline or amorphous absorber films with thicknesses in the 1-10 $\mu\text{m}$  range. Among the most successful polycrystalline compound materials, developed as absorber layers for high efficiency thin film solar cells, are CdTe, I-III-VI<sub>2</sub> ternary and quaternary compounds. Although these polycrystalline thin films have been recognised as presenting an opportunity for generating low cost electricity, most have regarded the technology as involving a sacrifice in performance in order to realize that goal. Recently, however, results obtained for small area cells and large area modules have been so impressive that they confound this thinking. It is now realized that polycrystalline thin film solar cells have the potential to meet or exceed the performance of the traditional commercial crystalline silicon technology at low cost.

Against this background, this study was focussed on the research and development of  $\text{CuInSe}_2/\text{CdS}/\text{ZnO}$  thin film solar cell devices. In this Chapter, the typical design and advantages of these cell structures are reviewed. A summary of the structural, optical electrical and preparation methods of  $\text{CuInSe}_2$  is also given. Finally, the material properties of CdS and ZnO will be discussed.

## 2.2 Design and Fabrication of CuInSe<sub>2</sub> Based Solar Cell Devices

The typical structure for a high efficiency I-III-VI<sub>2</sub> solar cell device is shown in Fig.2.1.

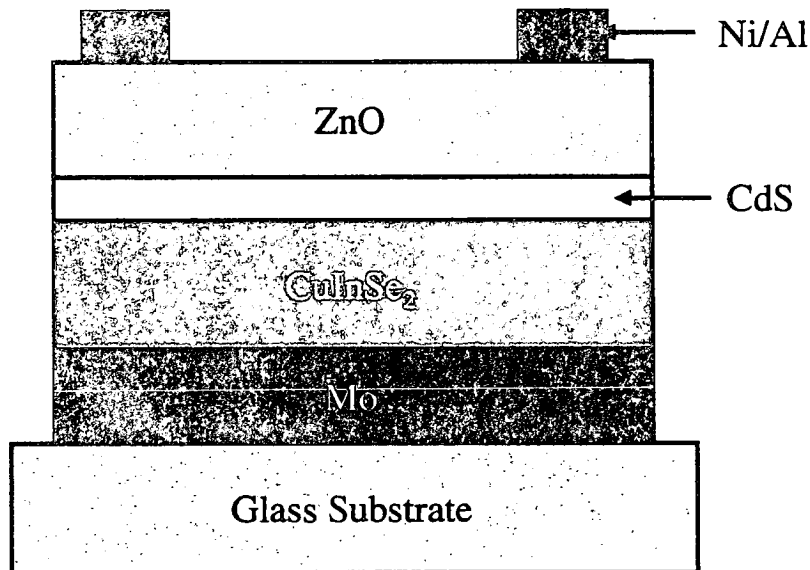


Figure 2.1: Schematic representation of a typical CuInSe<sub>2</sub>-based solar cell device.

The adhesion properties of CuInSe<sub>2</sub> vary on different glasses and it is widely reported that these polycrystalline materials adhere better to soda-lime rather than Corning glass. This observation is generally associated with a better match of thermal coefficients or diffusion of alkali metals from soda-lime glass into the layers (Basol et al., 1994). The first step in the fabrication process is the deposition of a thin (1-2  $\mu\text{m}$ ) molybdenum layer onto the glass substrate. This is done by means of electron-beam evaporation or sputtering. The presence of the Mo layer is important, not only as ohmic back contact to the solar cell, but also to improve the adhesion between the glass substrates and the active layers. Selection of Mo as the contact material to CuInSe<sub>2</sub> is due to its relative stability under CuInSe<sub>2</sub> film growth conditions (i.e. it does not chemically interfere with the growing films at the processing temperatures). However, the quality of the CuInSe<sub>2</sub> film (i.e. morphology, grain size and orientation) is directly affected by the quality of the underlying Mo layer. If deposited under sub-optimized conditions, the Mo layer exhibits either tensile or compressional stresses, which contribute to the commonly observed peeling of CuInSe<sub>2</sub> films at the Mo/CuInSe<sub>2</sub> interfaces. The key component of the solar cell assembly, depicted in Fig. 2.1, is the polycrystalline absorber film. The performance characteristics of this polycrystalline CuInSe<sub>2</sub> materials are strongly influenced by grain size, its orientation and loss mechanisms originating from grain boundaries. Besides losses due to insufficient diffusion lengths, photo-generated carriers can

recombine at grain boundaries and/or the hetero-interfaces (i.e. Mo/CuInSe<sub>2</sub>, CuInSe<sub>2</sub>/CdS, CdS/ZnO) due to lattice mismatches which cause interface states. Additionally, phase segregation (see Section 2.4.2), which can occur in compound semiconductors, may also influence the transport mechanisms. The material properties (structural, optical and electrical) properties of these polycrystalline thin films are critically influenced by the Cu/In atomic ratio of the films (Schön et al., 1997 and Alberts 1998). In general, Cu-rich and stoichiometric films exhibit a rough appearance with an average grain sizes between 1 and 2 μm. In-rich films are characterized by relatively smooth morphologies with grain sizes well below 1 μm. The carrier concentration of CuInSe<sub>2</sub> varies between 10<sup>14</sup> cm<sup>-3</sup> to 10<sup>19</sup> cm<sup>-3</sup> for In-rich and Cu-rich films, respectively (Alberts et al., 1998). The material properties and preparation methods of these polycrystalline absorber films are discussed in detail in Sections 2.4 and 2.5 respectively.

The p-n heterojunction is formed by the p-type CuInSe<sub>2</sub> absorber film and a n-type ZnO window layer. In order to improve device performance, a thin CdS buffer layer is included between the CuInSe<sub>2</sub> absorber film and ZnO window layer. The CdS buffer layer is lattice and electronically matched to the CuInSe<sub>2</sub> absorber film and its presence control the density of interface states and prevent the inter-diffusion of species (i.e. Cu, In or Se) from the absorber into the ZnO window layer, and vice versa. It is also known that these buffer layers significantly enhance the passivation of grain boundaries of the CuInSe<sub>2</sub> absorber films, resulting in higher open circuit voltages. The CdS buffer layers (approximately 50nm thick) are prepared by a chemical bath deposition (CBD) technique. The primary advantage of this CBD method is that complete surface coverage of the rough polycrystalline absorber films is obtained at very low thicknesses (5–10nm). Standard evaporation techniques require much higher thicknesses (> 1μm) to obtain complete surface coverage, resulting in a significant absorption in CdS and subsequently in a reduction in the blue response of completed cells. A more detailed discussion of the CBD growth technique is given in Section 4.5.1. ZnO is the ideal window material due to its wide band gap (3.2 eV), high temperature stability and the fact that it can be doped in any desired order. In order to optimize the CuInSe<sub>2</sub>/ZnO heterojunction, a 50nm highly resistive ZnO film is first deposited followed by the deposition of a highly conductive ( $N_D = 10^{18} - 10^{20} \text{ cm}^{-3}$ ) ZnO film of about 0.5μm. The ZnO window layers are deposited by means of sputtering (Section 4.5.2) at temperatures around 200 °C. The use of n<sup>+</sup>p heterojunctions (i.e. junctions with a significantly higher electron density in the ZnO

window layer than the hole density in the  $\text{CuInSe}_2$  absorber) shifts the electrical junction, i.e. the position within the space charge region where the density of electrons equals the density of holes, away from the metallurgical interface into the absorber. Therefore, photo-generated electrons crossing the metallurgical interface from the absorber into the ZnO window layers are majority carriers at this interface and thus are less affected by recombination. The solar cell structure is completed by the evaporation of  $1\text{-}2\mu\text{m}$  Al grid contacts onto the ZnO window layer. In order to reduce resistive losses a 50nm Ni layer can be included between the ZnO window layer and Al grid contacts.

### 2.3 Advantage of Chalcopyrite Thin Films for Photovoltaic Applications

The ternary  $\text{ABC}_2$  chalcopyrites ( $A = \text{Cu}$ ,  $B = \text{In}$  and  $C = \text{Se}$ ) form part of a large group of semiconducting materials with diverse structural, optical and electrical properties. These materials are attractive for thin film photovoltaic applications due to number of reasons:

- $\text{CuInSe}_2$  (CIS) is a direct band gap semiconductor with a gap energy of about 1eV. By partial substitution of In with Ga ( $\text{Cu(In,Ga)Se}_2$ ) and Se with S ( $\text{CuInS}_2$ ) the band gap value can be systematically shifted between 1.0 eV and 1.68 eV in order to obtain an optimum match with the solar spectrum. The high flexibility in the optical properties of these materials is demonstrated in Fig. 2.2.

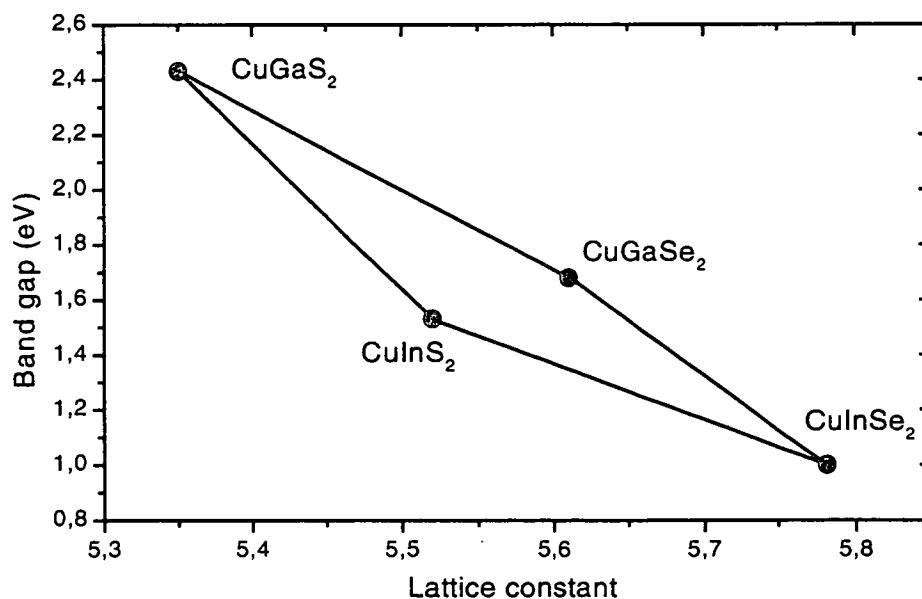


Figure 2.2: Band gap versus lattice constant for various chalcopyrite semiconductors.

- This material has the highest optical absorption coefficient ( $\alpha > 10^5 \text{ cm}^{-1}$ ) of all known thin film materials (Fig.2.3). This high value of  $\alpha$  implies that 99% of the incoming photons are absorbed within the first micron of the material. As a result, only 1-2 $\mu\text{m}$  of this material is required to effectively absorb the incoming photons, compared to bulk Si where at least 300 $\mu\text{m}$  of material is required.

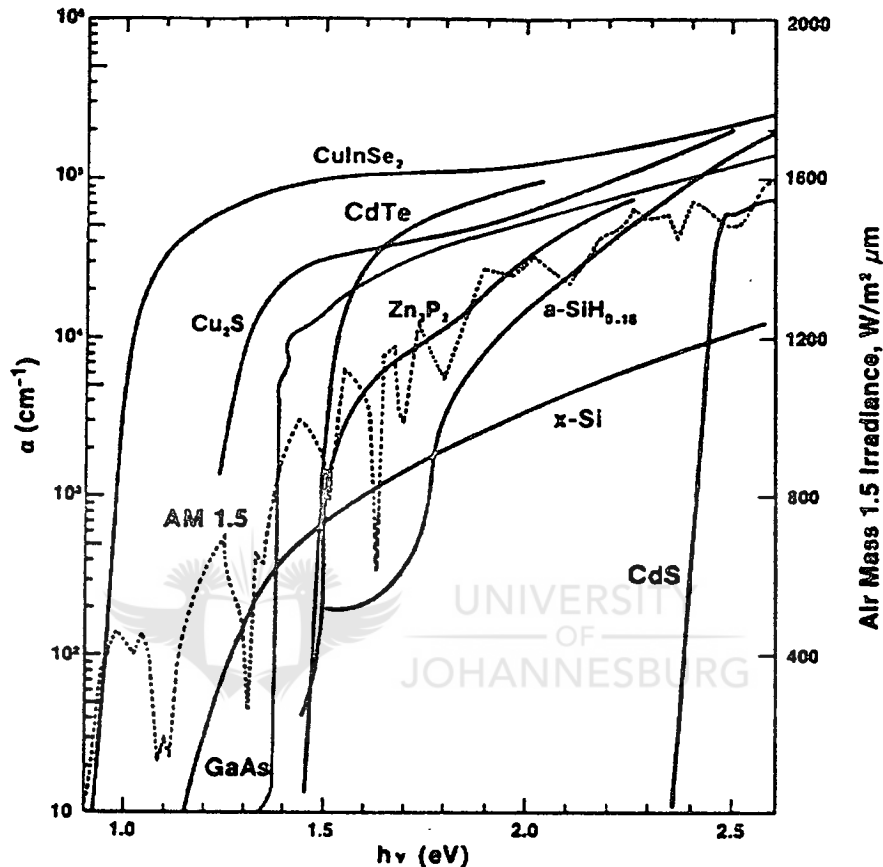


Figure 2.3: Absorption spectrum of  $\text{CuInSe}_2$  compared with other photovoltaic semiconductors. For comparison, the air mass (AM) 1.5 solar spectrum is also given (Jaffe and Zunger, 1984).

- All materials (Cu, In, Ga, Se and S) required to produce these photovoltaic devices are readily available. Low production costs are anticipated due to the fact that thin films of only a few microns are required and since these thin film configurations lend themselves to large area, continuous flow processing. For a moderate production line (1MW<sub>p</sub>/year) production cost below 1 USD/W is predicted (Gay, 1997).

- The electrical properties (i.e. conductivity, carrier concentrations and mobility of carriers) can be manipulated and controlled without any extrinsic doping (Section 2.4.4).
- A wide variety of industrial growth processes are available for the production of device quality CuInSe<sub>2</sub> (Section 2.5).
- Solid state devices based on CuInSe<sub>2</sub> and its alloys have produced the highest efficiencies ( $\eta$ ) for thin film laboratory-scale solar cells (Table 2.1). Module efficiencies (Table 2.2) are also in line with the reported values for polycrystalline Si modules.

<i>Type of Device</i>	<i>Area (cm<sup>2</sup>)</i>	<i><math>\eta</math> (%)</i>	<i>Reference</i>
<b>CuInSe<sub>2</sub>/CdS/ZnO/MgF<sub>2</sub></b>	0.262	14.8	Stolt et al., 1993
<b>Cu(In,Ga)Se<sub>2</sub>/CdS/ZnO/MgF<sub>2</sub></b>	0.414	17.7	Tuttle et al., 1995
<b>Cu(In,Ga)Se<sub>2</sub>/CdS/ZnO/MgF<sub>2</sub></b>	0.38	17.6	Hedström et al., 1993
<b>CuGaSe<sub>2</sub>/CdS/ZnO/MgF<sub>2</sub></b>	0.38	9.3	Vadenau et al., 1997
<b>CuInS<sub>2</sub>/CdS/ZnO/MgF<sub>2</sub></b>	0.38	12	Walter et al., 1994

Table 2.1: Reported performances of laboratory-scale solar cells based on CuInSe<sub>2</sub> and its alloys.

<i>Type of Device</i>	<i>Area (cm<sup>2</sup>)</i>	<i><math>\eta</math> (%)</i>	<i>Company</i>	<i>Reference</i>
<b>CIGS/CdS/ZnO/MgF<sub>2</sub></b>	3830	11.2	Siemens Solar Industries	Gay et al., 1994
<b>CIGS/CdS/ZnO/MgF<sub>2</sub></b>	90	13.9	ZSW	Diminier et al., 1996
<b>CIGS/CdS/ZnO/MgF<sub>2</sub></b>	51	14.1	Showa Shell	Kushiya et al., 1996

Table 2.2: Efficiencies of solar cell modules based on chalcopyrite thin films.

- CuInSe<sub>2</sub>-based solar cell devices have demonstrated good thermal, environmental and electrical stability. Preliminary tests indicated that the radiation tolerance of CuInSe<sub>2</sub> thin films is superior to that of single-crystalline Si or GaAs devices when tested under high energy electron and proton radiation (Michelson et al., 1985).



## 2.4 Material Properties of Ternary Chalcopyrite Semiconductor Thin Films

### 2.4.1 Introduction

The optimization of the material properties (structural, optical and electrical) of chalcopyrite thin films is an important prerequisite for the successful fabrication of highly efficient solar cell devices. The material properties of these thin films are also critically related to the growth conditions and therefore needs careful consideration. In this section the material properties of these chalcopyrite compound semiconductor are discussed in detail.

### 2.4.2 Structural Properties of Ternary Chalcopyrite Semiconductors

#### Crystallography of $\text{CuInSe}_2$

The crystal structure of the ternary chalcopyrites  $\text{ABC}_2$  ( $A = \text{Cu, B = In, Ga}$  and  $C = \text{Se, S}$ ) belongs to the non-symmorphic space group  $D_{2d}^{12}$  (eight atoms per primitive unit cell), which is a superlattice of the zinc-blende structure  $T_d^2$  (two atoms per primitive unit cell). However, there are three significant structural differences between ternary chalcopyrites and the zinc-blende structure (see Fig. 2.4 for comparison of the crystal structures).

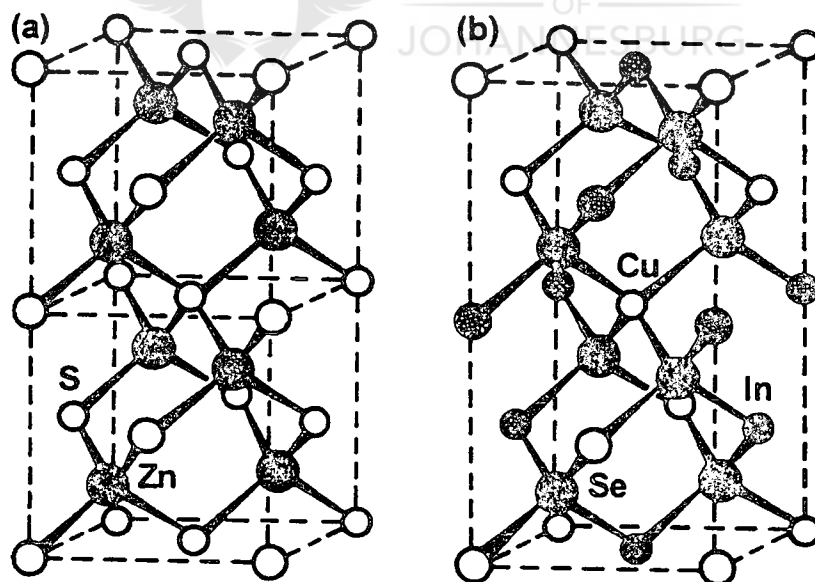


Figure 2.4: Crystal structures of (a) zinc-blende and (b) chalcopyrite lattices.

Firstly, rather than having a single cation, the ternary chalcopyrites have two cations; starting from the A atom and translating in a vertical direction in Fig.2.4(b) through intervals of  $c/2$  we find the sequence  $ABAB\dots$ , whereas translating horizontally with a interval of  $a$ , we find the

sequence AAA... . Secondly, these crystals often show a tetragonal distortion where the ratio between the lattice parameters  $\eta = c/2a$  (tetragonal deformation) differ from 1 by as much as 12%. Thirdly, the anions are displaced from their zinc-blende sites. This is clearly reflected by the fact that in the binary AC zinc-blende compounds each cation A has four anions C as nearest neighbours (and vice versa), whereas in a ternary chalcopyrite ABC<sub>2</sub> each cation A and B has four anions C as nearest neighbours, and each anion has two A and B cations as nearest neighbours. As a result, the anion C usually adopts an equilibrium position closer to one pair of cations than to the other, that is, unequal bond lengths  $R_{AC} \neq R_{BC}$  (i.e. the Cu-Se bond length is 2.43Å whereas the In-Se bond length is 2.57Å). The nearest-neighbour anion-cation bond length is given by (Jaffe and Zunger, 1984):

$$R_{AC} = [u^2 + (1+\eta^2)/16]^{1/2}a \quad (2.1)$$

and

$$R_{BC} = [(u-1/2)^2 + (1+\eta^2)/16]^{1/2}a \quad (2.2)$$

Where  $a$  is the cubic lattice constant and  $u$  the anion displacement. The bond length mismatch is hence  $\alpha = R_{BC}^2 - R_{AC}^2 = (u-1/4)a^2$  and vanishes for a zinc-blende like undistorted anion sublattice, where  $u = 1/4$ . Because of the added structural ( $\eta, u$ ) and chemical ( $A \neq B$ ) degrees of freedom relative to their binary analogs, the ternary ABC<sub>2</sub> semiconductors exhibit a far richer range of physical and chemical properties. A summary of the most important structural properties of CuInSe<sub>2</sub> is given in Table 2.3.

<i>I-III-VI<sub>2</sub> Properties</i>	<i>Value</i>	<i>Unit</i>
<b>Formula</b>	CuInSe <sub>2</sub>	
<b>Molecular weight</b>	336.28	
<b>Density</b>	5.77	g cm <sup>-3</sup>
<b>Colour</b>	Grey	
<b>Melting temperature</b>	986	°C
<b>Symmetry</b>	Chalcopyrite	
<b>Space group</b>	$D_{2d}^{12}$	
<b>Lattice parameters</b>		
<i>a</i>	5.773	Å
<i>c</i>	11.55	Å
<i>u</i>	0.22	Å

Thermal expansion coefficient a-axis (at 273K)	$8.32 \times 10^{-6}$	$K^{-1}$
c-axis (at 273K)	$7.89 \times 10^{-6}$	$K^{-1}$
Thermal Conductivity	0.086	$W cm^{-1} K^{-1}$
Microhardness (112 face)	$3.2 \times 10^9$	$N m^{-2}$
Compressibility	$1.4 \times 10^{-11}$	$m^2 N^{-1}$

Table 2.3: Summary of the important mechanical properties of  $CuInSe_2$ .

### Phase Diagram of I-III-VI<sub>2</sub> systems

The structural, optical and electrical properties of chalcopyrite thin films are critically influenced by the presence of secondary phases in the bulk of the material. In most cases the presence of these Cu-rich and In-rich secondary phases is detrimental to device performance and its presence should therefore be limited or eliminated if possible. In this regard, phase diagrams are very useful in predicting and identifying these secondary phases in final products.

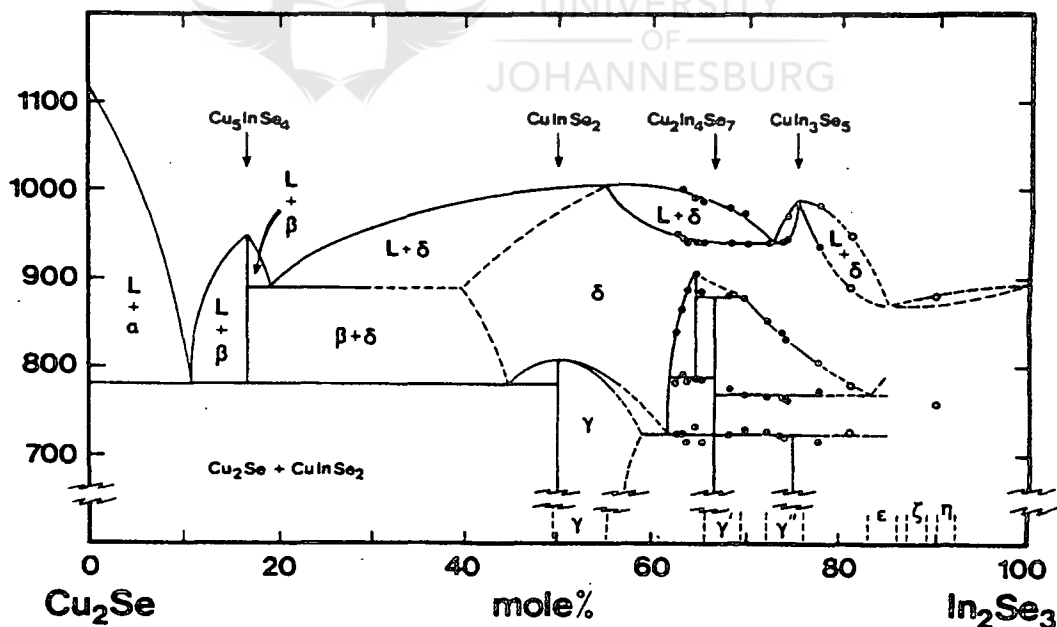


Figure 2.5:  $Cu_2Se-In_2Se_3$  pseudobinary phase diagram (Fearheiley, 1986)

The available phase information is largely limited to the  $Cu_2Se-In_2Se_3$  pseudo-binary phase diagram. According to this phase diagram (Fig. 2.5) various compounds (e.g.  $Cu_2In_4Se_7$ ,  $Cu_3In_5Se_9$ ,  $CuIn_3Se_5$ ,  $Cu_5InSe_4$  and  $CuIn_5Se_8$ ) are likely to occur in this ternary system (Fearheiley, 1986). The homogeneity ranges deduced from X-ray diffraction studies at room

temperature are indicated below the break in the temperature axis. The  $\gamma'$ ,  $\gamma''$  and  $\gamma'''$  regions represent distinct phases associated with the compounds  $\text{CuInSe}_2$ ,  $\text{Cu}_2\text{In}_4\text{Se}_7$  and  $\text{CuIn}_3\text{Se}_5$ , respectively. The  $\eta$ ,  $\epsilon$  and  $\zeta$  phases represent distinct cubic and hexagonal mixed stacking regions (Fearheiley, 1986). The sphalerite phase is stable only at temperatures higher than  $570^\circ\text{C}$ , whereas the chalcopyrite structure is stable from room temperature up to  $810^\circ\text{C}$ . The chalcopyrite single phase  $\text{CuInSe}_2$  extends from the stoichiometric composition of 50 mol.%  $\text{In}_2\text{Se}_3$  to the In-rich composition of about 55 mol.%  $\text{In}_2\text{Se}_3$ . The corresponding Cu/In atomic ratio for single material lies between 1.0 and 0.82. For cases where Cu/In atomic ratios are greater than 1.0, the materials are expected to contain secondary phases of  $\text{Cu}_2\text{Se}$  and for contrary cases (Cu/In atomic ratios less than 0.82) the materials are expected to contain secondary phases of the type  $\text{Cu}_2\text{In}_4\text{Se}_7$  and  $\text{CuIn}_3\text{Se}_5$ .

### 2.4.3 Optical Properties of Ternary Chalcopyrite Semiconductors

In recent years the optical properties of  $\text{CuInSe}_2$  near and above the fundamental edge have been studied by electroreflectance (Shay and Kasper, 1972), reflection (Gan et al., 1974), absorption (Hörig et al., 1977) and photovoltage measurements (Parkes et al., 1973). At present it seems to be well established that  $\text{CuInSe}_2$  is a direct gap semiconductor with a gap of about 1eV at 300K.

Despite the overall structural similarity between the ternary I-III-VI<sub>2</sub> compounds and their binary analogs (Fig. 2.4), the band gap of the former compounds are substantially smaller than those of the latter. This phenomenon is clearly demonstrated in Table 2.4 where the band gap anomaly  $\Delta E_G$  (the difference between binary and ternary gap values) for various semiconductors are depicted. This shift in the band gap to smaller values for ternary compound semiconductors has been explained in terms of a chemical factor  $\Delta E_G^{\text{Chem}}$  and a structural factor  $\Delta E_G^S$  (Jaffe and Zunger, 1984). In the former case, the 3d or 4d electrons of the noble metal hybridize with the p-like valance band (p-d hybridization) due to the proximity of their levels, resulting in a reduction in the value of the band gap by up to 1eV. In the latter case, the uppermost valence band of these compounds is lifted due to simultaneous influence of spin-orbital and crystal-field interactions caused by the uniaxial tetragonal distortion of the crystal lattice (c/a) and the displacement of group VI anions from the ideal position [(1/4, 1/4, 1/8)], as discussed in Section 2.4.2

<i>Ternary</i>	<i>Ternary</i> $E_G$ (eV)	<i>Binary analog</i>	$\Delta E_G$ (eV)
$\text{CuInSe}_2$	1.04	$\text{Zn}_{0.5}\text{Cd}_{0.5}\text{Se}$	1.29
$\text{CuGaSe}_2$	1.68	$\text{ZnSe}$	1.00
$\text{CuInS}_2$	1.53	$\text{Zn}_{0.5}\text{Cd}_{0.5}\text{Se}$	1.64
$\text{CuGaS}_2$	2.43	$\text{ZnS}$	1.37
$\text{CuAlSe}_2$	2.67	$\text{Mg}_{0.5}\text{Zn}_{0.5}\text{Se}$	1.47
$\text{CuInTe}_2$	0.96	$\text{Zn}_{0.5}\text{Cd}_{0.5}\text{Te}$	0.98

Table 2.4: Band gaps of ternary semiconductors and the difference  $\Delta E_G$  (band gap anomaly) with respect to the binary analogs (Jaffe and Zunger, 1984).

Both these effects and lower crystal symmetry make the effective masses of chalcopyrite compounds larger than those of II-VI compounds having comparable band gap energies. Hence the high absorption coefficient of chalcopyrite compounds (Fig. 2.3).

The variation of the band gap of I-III-VI<sub>2</sub> chalcopyrites compounds with temperature is also anomalous compared to their binary analogues. In the case of  $\text{CuInSe}_2$ , the energy gap decreases with increasing temperatures, as does that of its binary analogue. However, the rate of change of  $E_G$  with temperature ( $\Delta E_G/\Delta T$ ) is smaller (Shay et al., 1973). It has been suggested that the  $p$ - $d$  hybridization of the uppermost valance band of I-III-VI<sub>2</sub> compounds is also responsible for this phenomenon. Studies on  $\text{CuInSe}_2$  thin films and single crystals show that the temperature dependence of the band gap can be described approximately by the relation proposed by Varshni for the temperature variation of the energy gap in binary compounds and elemental semiconductors (Varshni, 1967):

$$\Delta E = E_0 - E_G(T) = \delta T^2/(T + \beta) \quad (2.3)$$

where  $E_G$  is the band gap,  $E_0$  is its value at 0K, and  $\beta$  is a parameter of the same order as the Debye temperature  $\theta_d$ .

#### 2.4.4 Electrical Properties of Ternary Chalcopyrite Semiconductors

The electronic properties of CuInSe<sub>2</sub> (CIS) and its alloys are controlled largely by the intrinsic defect chemistry of the material. The possible origin of defect levels in chalcopyrite thin films is atomic vacancies, atoms on wrong lattice sites (antisites) and interstitial atoms. The electronic properties of these thin films are therefore critically influenced by small deviations from perfect stoichiometry (i.e. when Cu/In atomic ratio deviates from 1). In these polycrystalline materials, a Cu/In atomic ratio greater than 1 produces Cu-rich precipitates (see Fig. 2.5). These are conductive and short-circuit devices. In the case of compositions between Cu-rich and slightly In-rich, materials exhibit p-type conductivity and have resistivities  $\leq 0.1 \Omega \text{ cm}$ . Very In-rich materials (Cu/In atomic ratio around 0.3) is n-type and has resistivities that increase sharply from  $0.1 \Omega \text{ cm}$  to approximately  $10^6 \Omega \text{ cm}$  with an increasing In content (Rockett and Birkmire, 1991). It is generally believed that in Cu-rich films  $Cu_{In}^-$  and  $V_{In}^-$  acceptor-type defects form to account for the deviation from stoichiometry. Since both these defects are negatively charged it is expected that  $V_{Se}^{++}$  donor-type defects will form to maintain charge neutrality. In slightly In-rich material (Cu/In atomic ratio = 0.85–0.95), which are generally used to produce high efficiency devices, the most probable intrinsic defect levels are  $V_{Cu}^-$  and  $V_{Se}^{++}$  (Schön et al., 1997). In the case of very In-rich material (Cu/In atomic ratio below 0.5) it is generally expected that  $In_{Cu}^{++}$  donor-type and  $V_{Cu}^-$  acceptor type defects will form to account from deviation from stoichiometry. It is also believed that because these are oppositely charged, these materials tend to be heavily electrically compensated (Rockett and Birkmire, 1991). Changes in the resistivity between Cu- and In-rich single crystals of CuInSe<sub>2</sub> have also been observed. However, these changes are less dramatic than in polycrystalline CuInSe<sub>2</sub>, most likely due to grain boundary effects in polycrystalline CIS rather than differences in bulk resistivity between epitaxial and polycrystalline CIS. Temperature-dependent transport measurements on single crystals (Neumann and Tomlinson, 1990) revealed carrier mobility values that varies between 15 and  $150 \text{ cm}^2\text{V}^{-1}\text{s}^{-1}$  for p-type materials with carrier concentrations ranging between  $0.15$  and  $2 \times 10^{17} \text{ cm}^{-3}$  at 300K. For n-type materials, sample mobilities were 90 to  $900 \text{ cm}^2\text{V}^{-1}\text{s}^{-1}$ , while carrier densities varied from  $1.8 \times 10^{15}$  to  $5 \times 10^{17} \text{ cm}^{-3}$  at 300K. A clear correlation between carrier densities, mobilities and film composition was not obvious from these studies. A summary of the electrical properties of chalcopyrite thin films is presented in Table 2.5.

Film Stoichiometry	Cu-rich	Slightly In-rich	Very In-rich
I/III Ratio	> 1	0.85 – 0.95	< 0.5
Conductivity	p-type	p-type	n-type
Intrinsic Defect Level	$Cu_{In}^-, V_{In}^-, V_{Se}^{++}$	$V_{Cu}^-, V_{Se}^{++}$	$In_{Cu}^{++}, V_{Cu}^-$
Resistivity ( $\Omega \text{ cm}$ )	$\leq 0.1$	10 – 20	$> 10^4$
Carrier Concentration ( $\text{cm}^{-3}$ )	$> 10^{17}$	$2 - 4 \times 10^{16}$	$10^{14} - 10^{15}$
Mobility ( $\text{cm}^2 \text{V}^{-1} \text{s}^{-1}$ )	15 – 150	15 – 150	90 – 900

Table 2.5: Summary of the electrical properties of I-III-VI<sub>2</sub> compound semiconductors as function of material composition.

## 2.5 Preparation Methods for CuInSe<sub>2</sub>

### 2.5.1 Introduction

The heart of CuInSe<sub>2</sub>/CdS/ZnO thin film solar cell devices is the polycrystalline absorber film. As pointed out the preceding Sections, the structural, optical and electrical properties of I-III-VI<sub>2</sub> compound films are highly dependent on their composition and defect chemistry, which in turn are strongly related to the film growth conditions. The choice of the processing method is, therefore, important for obtaining compound films that can yield high efficiency solar cells. In this Section some of the most relevant processing technologies of chalcopyrite thin films are reviewed. Attention is also given to the reaction kinetics for CuInSe<sub>2</sub> film growth.

### 2.5.2 Deposition Technologies

Copper indium diselenide was first selenized in 1953 (Hahn et al., 1953). Since then a variety of methods have been developed for deposition of CuInSe<sub>2</sub> absorber materials. Control of film stoichiometry and uniformity are the most crucial factors for obtaining high quality CuInSe<sub>2</sub> thin films required to produce high efficiency solar cells. Other factors which influence process selection are material utilization, capital equipment costs and scalability prospects. Irrespective of the growth technique used, a good quality CuInSe<sub>2</sub> film should satisfy the following important conditions:

- The Cu/In stoichiometric ratio of the CuInSe<sub>2</sub> layer should be in the 0.9-1.0 range. This stoichiometric ratio should be maintained on a micro- as well as macro-scale.

- The CuInSe<sub>2</sub> films should be adhering well to the Mo-coated substrate. As important, these films should have superior mechanical properties.
- The microstructure of the film should consist of columnar grains. Grain size should be above 1 μm for high performance devices with efficiencies greater than 15%.
- The film should be free of detrimental secondary phases (e.g. Cu<sub>2-x</sub>Se, CuSe and Cu<sub>2</sub>Se).

The CIS film processing techniques currently in use can be grouped under two main categories; single-stage processing and two-stage processing methods (Tables 2.6).

<i>Processing Technology</i>	<i>SS/TS</i>	<i>η (%)</i>	<i>Reference</i>
<b>Co-evaporation</b>	SS	14.8	Stolt et al., 1993
<b>Sputtering</b>	SS	5	Piekoszewski et al., 1980
<b>Laser ablation</b>	SS	2.4	Dittrich et al., 1993
<b>Electrodeposition</b>	SS	6.5	Guillemoles et al., 1994
<b>Chemical Spray Pyrolysis</b>	SS	2	Bougnot et al., 1986
<b>Selenization of Cu/In in H<sub>2</sub>Se</b>	TS	>10	Basol et al., 1993
<b>Selenization of Cu/In/Se in Se vapour</b>	TS	>10	Nakada et al., 1994
<b>Thermal Reaction of Cu/In/Se stacks</b>	TS	>10	Probst et al, 1996

Table 2.6: Examples of single-stage (SS) and two-stage (TS) processing methods for the growth of CuInSe<sub>2</sub> thin films and the corresponding efficiencies (η) of solar cells fabricated on them.

### Single-Stage Processing Methods

Single-stage processing approaches for CuInSe<sub>2</sub> thin film growth involve the delivery of all the components of this material (Cu, In and Se) in one single step onto a heated substrate in order to form the compound film. Some of the most important examples of such methods include co-evaporation, sputtering and laser ablation. Potentially low-cost, non-vacuum deposition techniques such as electrodeposition and chemical spray pyrolysis have also been used to prepare CuInSe<sub>2</sub>. However, high efficiency solar cell devices cannot be fabricated in this way due to the poor crystalline properties of the final compound CuInSe<sub>2</sub> absorber films. By far the most successful single-stage approach, consistently producing solar cell devices with conversion efficiencies above 10%, is the co-evaporation of all elements from open



crucibles or effusion cells. This technique was introduced by a group at Boeing in 1982 when they demonstrated an 11% efficient  $\text{CuInSe}_2/\text{CdS}$  solar cell (Mickelson and Chen, 1982). In this process, the composition of the evaporating flux is continuously adjusted from highly Cu-rich to highly In-rich during the growth period. Diffusion during growth mixes the two films in order to form a near-stoichiometric compound film.  $\text{CuInSe}_2$  films prepared by this method display the large grain size of Cu-rich material, but with the desirable electronic properties of slightly In-rich material. Alloys of  $\text{CuInSe}_2$  with  $\text{CuGaSe}_2$  and  $\text{CuInS}_2$  and compositional profiles can be obtained by the co-evaporation method. However, an accurate control of the evaporation rates is crucial for the success of this approach. It is usually accomplished by accurate temperature control of the crucibles, by mass spectrometry or by electron impact emission spectroscopy (EIES). Although simultaneous evaporation from four elemental sources produced the highest efficiency laboratory-scale  $\text{CuInSe}_2$  (> 14%),  $\text{CuGaSe}_2$  (> 9%) and  $\text{CuInGaSe}_2$  (> 17%) devices, poor material utilization and the difficulty of obtaining uniform metal fluxes over large areas are some of the important limitations of scaling-up this method to high volume production.

### **Two-Stage Processing Methods**

In general, two-stage processing is versatile since the processing steps required for the formation of the compound films are divided into two or more steps. During the first stage of the process, a precursor film containing all or some of the constituent elements of the compound, is deposited on a substrate which may or may not be heated. During the second stage of the process the constituents are reacted with each other and/or with other species introduced from a reactive atmosphere to form a continuous and compact compound film of  $\text{CuInSe}_2$ . Two-stage processing methods that produce the best quality  $\text{CuInSe}_2$  thin films generally involve vacuum processing. Selenization (in elemental Se vapour in vacuum or in  $\text{H}_2\text{Se}/\text{Ar}$ ) of metallic alloys for  $\text{CuInSe}_2$  formation is one of the most promising two-stage approaches in use today. In this approach, the evaporation of the precursor metals (Cu and In) is done sequentially. Therefore, simple thickness measuring devices like quartz balances can be used to adjust the final composition of the films. Attempts to form alloys of  $\text{CuInSe}_2$  with  $\text{CuGaSe}_2$  by selenization resulted in the separation of two phases rather than in the formation of mixed alloys, thus leading to devices with a graded band gap. Additionally, adhesion plays a more critical role in this process owing to the large expansion of the material during the selenization process. Another fairly successful processing technique is the rapid thermal

treatment of stacked layers of Cu, In and Se (Cu/In/Se). These stacks are thermally evaporated and then rapidly heated to temperatures above 500°C in order to produce single-phase material. Material losses (especially Se) during high temperature annealing are considered as the most serious drawback of this specific two-stage processing approach.

Commercialization of CuInSe<sub>2</sub>-based solar cell technologies has already been realized. Companies like Siemens Solar Industries (SSI), Energy Photovoltaics (EPV) and International Solar Energy Technology (ISET) who are front runners in these efforts are employing two-stage processing techniques. It is believed that their technologies are based on the H<sub>2</sub>Se/Ar treatment of sputtered metallic alloys. Other companies who are still in the developmental stages are Solarex Inc and Zentrum für Sonnenenergie- und Wasserstoff- Forschung (ZSW). In the case of ZSW, single-stage processes are employed to produce modules.

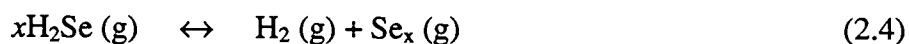
### 2.5.3 Diffusion and Reaction Kinetics of CuInSe<sub>2</sub> Film Growth

A complete understanding of the growth kinetics of these chalcopyrite thin films is of paramount importance. This information is important because:

- a complete understanding of the reaction pathways can be used to modify the absorber layer properties for maximum cell efficiency.
- the information can be used in design and operation of large scale solar panel manufacturing equipment.

Interdiffusion and diffusion in thin films are similar to processes occurring in bulk films. However, the geometry and presence of a higher density of material defects compared to bulk crystals, makes diffusion in thin films a more complicated field of study (Philibert, 1991). Diffusion in thin films can be observed at temperatures well below those at which vacancy diffusion is negligible (Hall and Morabito, 1976). Structural defects which influence self and impurity diffusion through thin films include grain boundaries, dislocations and vacancies. Grain boundaries are surface or area defects that constitute the interface between grains of different crystallographic orientation. The atoms at the grain boundaries are as energetic as the atoms on the film surface and various atomic phenomenon are accelerated. In CuInSe<sub>2</sub> thin films, characterized by typical grain sizes around 1 μm and a high density of grain boundaries, this effect is expected to play a significant role. Dislocations may be viewed as line defects

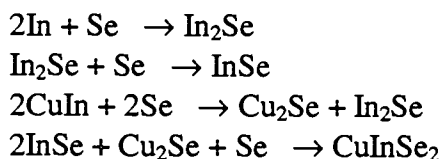
which bear a definite crystallographic relationship with the lattice. These dislocations can be sites for charge recombination or generation as a result of uncompensated dangling bonds. Diffusion, film stress and thermally induced mechanical relaxation processes are also strongly influenced by dislocations. Vacancies are point defects that arises when lattice sites are unoccupied by atoms. Vacancies are formed as the energy required to displace an atom from the lattice to the surface, is not particularly high. Additionally, the increase in system disorder or entropy due to mixing of vacancies among lattice sites gives rise to a thermodynamic probability that a fraction  $f$  of the total number of sites will be unoccupied at any temperature  $T$ . In the present study, CuInSe<sub>2</sub> thin films were prepared by the selenization (in H<sub>2</sub>Se/Ar and elemental Se) of metallic alloys. When H<sub>2</sub>Se gas enters the heated diffusion furnace, the H<sub>2</sub>Se dissociates according to the following chemical reaction (Verma et al., 1991):



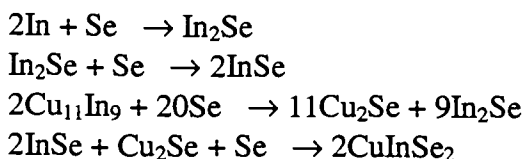
where  $x$  is 1, 2, 3, 5, 6 and 7.

Gas-phase analysis has established that the reacting selenium gas-phase species could be either H<sub>2</sub>Se or one of the Se <sub>$x$</sub>  species (Verma et al., 1992). Both the H<sub>2</sub>Se and Se <sub>$x$</sub>  absorbed from the gas phase dissociate on the film surface to form selenium species. The reaction pathway leading to the formation of CuInSe<sub>2</sub> can be described by two models, depending on the presence of different metallic phases in the initial film structure when Se delivery is initiated (Orbey et al., 1997 and Verma et al., 1996):

In the case of liquid phase In with dissolved Cu where the process kinetics is determined by the presence of the CuIn metallic phase, the following reaction pathway is valid:



In the case of the solid phase (i.e. Cu<sub>11</sub>In<sub>9</sub> are dominating starting species) the following pathway is valid:



## 2.6 Semiconducting Transparent Thin Films

### 2.6.1 Introduction

As pointed out in Section 2.2, the CdS buffer layer and ZnO window layer forms an integral part of the CuInSe<sub>2</sub>-based solar cell device. In this study, attention was also given to the growth and characterization of these materials. Experimental conditions were optimized in order to produce completed solar cell devices. In this Section, the relevant material properties of CdS and ZnO are reviewed.

### 2.6.2 Basic Material Properties of CdS and ZnO

Almost all compounds of the A<sup>II</sup>B<sup>VI</sup> type crystallizes in the hexagonal wurtzite lattice (Fig. 2.6).

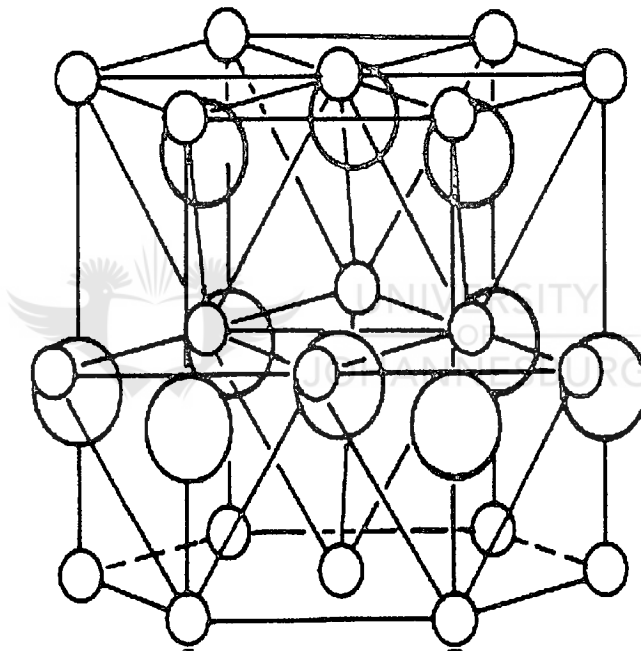


Figure 2.6: The wurtzite lattice of zinc oxide: small circles represent zinc atoms, whereas large circles depict oxygen atoms.

In the case of ZnO, for example, the zinc atoms are nearly in the position of hexagonal close packing. Every oxygen atom lies within a tetrahedral group of four zinc atoms, and all these tetrahedra point in the same direction along the hexagonal axis giving the crystal its polar symmetry. A similar situation holds for CdS. The lattice parameters of these materials are given in Table 2.7.

Compound	Crystal Structure Type	Lattice Parameters, Å		References
		a	c	
CdS	Wurtzite	4.13	6.75	Konstantinov and Smirnov et al., 1915
ZnO	Wurtzite	3.24	5.19	Hartnagel et al., 1995

Table 2.7: Crystal structure of  $A^{II}B^{VI}$  compounds.

Chemical bonding of  $A^{II}B^{VI}$  compound is rather complex. Atoms of group II elements have two  $s^2$  electrons in the outer  $s$  shell, whereas atoms of group six have  $s^2p^4$  electrons. When metal atoms have sufficiently strong electropositive properties and can give up two outer  $s$  electrons to nonmetal atoms, doubly charged ions with filled  $p$  shells are formed and a structure with the octahedral coordination (of the NaCl type) is produced, in the same way as in chalcogenides of alkaline-earth metals. Compounds with the tetrahedral coordination with the sphalerite or wurtzite structure are formed between elements of the zinc and oxygen subgroups when metals have sufficiently high ionization potentials and do not give up their electrons, but share them with neighboring nonmetal atoms. In this case, four elongated electron clouds are formed around each atom and these clouds are in the  $sp^3$  configuration, which is due to the hybridization of the  $s$  and  $p$  orbitals. Thus, four bonds are formed which are directed toward the apices of a regular tetrahedron. Since elements of group VI have a stronger electronegativity than elements of group II, a two-electron cloud shifts from atoms of group II elements to atoms of group VI. Therefore, in the  $A^{II}B^{VI}$  compounds, the binding is partly ionic and partly covalent, and these compounds exhibit properties typical of both types of binding. The tetrahedral distribution of atoms in the  $A^{II}B^{VI}$  compounds is similar to their distribution in crystals of group IV elements, which are typically covalent. However, the magnitude and sign of the effective charge, the crystal structure, and the nature of the cleavage of the  $A^{II}B^{VI}$  compounds all indicate a considerable ionic component of the binding.

## References

- V. Alberts (1998) South African Journal of Science **94**, p. 341-347.
- V. Alberts, R. Swanepoel and M. J. Witcomb (1998) Journal of Material Science **33**, p. 2919-2925.
- B. M. Basol, V. K. Kapur, A. Halani and C. Leidholm (1993) Solar Energy Materials and Solar Cells **29**, p 163.
- B. M. Basol, V. K. Kapur, C. R. Leidholm, A. Minnick and A. Helani, (1994), Studies on substrates and contacts for CIS films and devices, Proc. IEEE First World Conference Photovoltaic Energy Conversion, Hawaii, **1**, p 148.
- J. Bougnot, S. Duchemin and M. Savelli (1986) Solar Cells **16**, p 221-236.
- B. Dimmler, E. Gross, R. Menner, M. Powalla, D. Hariskos, M. Ruckh, U. Rühle and H. W. Schock (1990) Proc. 25<sup>th</sup> IEEE Photovoltaic Specialist Conference, Washington, p 757.
- H. Dittrich, M. Klose, M. Brieger, R. Schäffler and H. W. Schock (1993) Proc. 23<sup>rd</sup> IEEE Photovoltaic Specialist Conference, Louisville, p 102.
- M. L. Fearheiley, (1986) Solar Cells **16**, p 91.
- J. N. Gan, J. Tauc, V. G. Lambrecht and M. Robbins (1974) Solid State Commun **15**, p 605.
- R. Gay, M. Dietrich, C. Fredric, C. Jensen, K. Knapp, D. Tarrant and D. Willett, (1994) 12<sup>th</sup> EC Photovoltaic Solar Energy Conference, Amsterdam, p 935.
- R. Gay (1994) Solar Energy Materials and Solar Cells **47**, p 19.
- J. Guillemoles, S. Massaccesi, P. Cowrache, L. Thouin, S. Sanchez, D. Lincot and J. Vedel (1994) Proc. 12<sup>th</sup> EC Photovoltaic Solar Energy Conference, Amsterdam, p 406.
- H. Hahn, G. Frank, W. Klinger, A. D. Meyer and G. Z. Storger (1953) Anorgg. Allgem. Chem. **271**, p 153.
- P. M. Hall and J. M. Morabito (1976) Thin Solid Films **33**, p 107.
- H. L. Hartnagel, A. L. Dawar, A. K. Jain and C. Jagadish (1995) Semiconducting Transparent Thin Films, Institute of Physics Publishing Bristol and Philadelphia.
- J. Hedström, H. Ohlsen, M. Bodegård, A. Kylner, L. Stolt, D. Hariskos, M. Ruckh and H. W. Schock (1993) Proc. 23<sup>rd</sup> IEEE Photovoltaic Specialists Conference, Louisville, p 364.
- W. Hörig, H. Neumann, H. J. Höbler and G. Kühn (1977) Phys. Status Solidi B **80**, p k21.
- J. E. Jaffe and A. Zunger (1984) Phys. Review **29**(4), p 1882-1905.
- N. S. Konstantinov and V. N. Smirnov (1915) Izv. Leningrad. Politekhn. In-ta **23**, p 713.

- K. Kushiya, I. Sugiyama, M. Tachiyuki, T. Kase, Y. Nagoya, D. Okumura, M. Sato, O. Yamase and H. Takeshita (1996) Proc. PVSEC-9, p 143.
- R. A. Mickelsen and W. S. Chen (1982) Us Patent No 433 5266.
- R. A. Mickelsen, W. S. Chen, B. I. Starbery, H. Bursh, J. M. Stewart, Y. R. Hsiao and W. Devaney (1985) Proc. 18<sup>th</sup> IEEE Photovoltaic Specialist Conference, Kissimmee, p 1069.
- V. Nadenau, D. Hariskos and H. W. Schock (1997) Proc. 14<sup>th</sup> EC Photovoltaic Solar Energy Conference, Vienna, p 1250.
- T. Nakada, R. Onishi and A. Kunioka (1994) Solar Energy Materials and Solar Cells **35**, p 209-214.
- H. Neumann and R. D. Tomlinson (1990) Solar Cells **28**, p 301.
- N. Orbey, H. Hichri, R. W. Birkmire and T. W. F. Russell (1997) Progress in Photovoltaics: Research and Application **5**, p 237.
- J. Parkes, R. D. Tomlinson and M. J. Hampshire (1973) Solid-State Electron **16**, p 773.
- J. Philibert (1991) Applied Surface Sciences **53**, p 74.
- J. Piekoszewski, J. Loferski, R. Beaulien, J. Beall, B. Roessler and J. Shewchun (1980) Solar Energy Mater. **2**, p 363.
- V. Probst, F. Karg, J. Rimmasch, W. Riedl, W. Stetter, H. Harms and O. Eibl (1996) Proc. Mat. Res. Soc. Symp. **426**, p 165.
- A. Rockett and R. W. Birkmire (1991) J. Appl. Phys. **70**, p R81.
- J. H. Schön, V. Alberts and E. Bucher (1997) Thin Solid Films **301**, p 115-121.
- J. L. Shay and H. M. Kasper (1972) Phys. Rev. Lett. **29**, p 1162.
- J. L. Shay, B. Tell, H. M. Kasper and L. M. Shiavone (1973) Phys. Rev. **B(7)**, p 4485.
- L. Stolt, J. Hedström, J. Kessler, M. Ruckh, K-O Velthaus and H. W. Schock (1993) Appl. Phys. Lett. **62(6)**, p 597-599.
- J. R. Tuttle, T. A. Berens, S. E. Asher, M. A. Contreras, K. R. Ramanathan, H. L. Tennant, R. Bhattacharya, J. Keane and R. Noufi (1995) Proc. 13<sup>th</sup> EC Photovoltaic Solar Energy Conference, Barcelona, p 2131.
- Y. P. Varshni (1967) Physica **34**, p 149.
- S. Verma, J. Varrin, R. W. Birkmire and T. W. F. Russell (1991) Proc. 22<sup>nd</sup> IEEE Photovoltaics Specialist Conference, Las Vegas, p 914.

S. Verma, S. Yamanaka, B. E. McCandless, R. W. Birkmire and T. W. F. Russel (1992) Proc. 11<sup>th</sup> EC Photovoltaic Solar Energy Conference, Montreaux, p 807.

S. Verma, N. Orbey, R. W. Birkmire and T. W. F. Russel (1996) Progress in Photovoltaic: Research and Applications 4, p 341.

T. Walter, R. Menner, C. Köble and H. W. Schock (1994) Proc. 12<sup>th</sup> EC Photovoltaics Solar Energy Conference, Amsterdam, p 1755.





## CHAPTER 3

# FUNDAMENTAL PRINCIPLES OF SOLAR CELL DEVICES

### 3.1 Introduction

Solar cells operate by converting sunlight directly into electricity using the electric properties of a class of materials known as semiconductors. In this Chapter, this important phenomenon will be discussed, starting from the basic physical principle of sunlight radiation. Attention is mainly given to a mathematical description of a  $p-n$  junction diode and solar cell parameters influencing the operation of solar cells.

### 3.2 Outline of Solar Cell Development

Solar cells depend upon the photovoltaic effect for their operation. This effect was reported initially in 1839 by Becquerel, who observed a light-dependent voltage between electrodes immersed in an electrolyte. It was also observed in an all-solid-state system in 1876 for the case of selenium. This was followed by the development of photocells based on both this material and cuprous oxide. Although a silicon cell was reported in 1941, it was not until 1954 that the forerunner of present silicon cells was announced. This device represented a major development because it was the first photovoltaic structure that converted light to electricity with reasonable efficiency. These cells found application as power sources in spacecrafts as early as 1958. By the early 1960's, the design of cells for space use had stabilized, and over the next decade, this was their major application.

The early 1970's saw an innovative period in silicon cell development, with marked increases in realizable energy-conversion efficiencies. At about the same time, there was a reawakening of interest in terrestrial use of these devices. By the end of the 1970's, the volume of cells produced for terrestrial use had completely outstripped that for space use. This increase in production volume was accompanied by a significant reduction in solar cell costs. The early 1980's saw newer device technologies being evaluated at the pilot production stage, poised to enable further reduction in costs over the coming decade. With such cost reductions, a continual expansion of the range of commercial applications is ensured for this approach to utilize the sun's energy.

### 3.3 Physical Principle of Sunlight Radiation

#### 3.3.1 Physical Source of Sunlight

Radiant energy from the sun is vital for life on our planet. It determines the surface temperature of the earth as well as supplying virtually all the energy for natural processes both on its surface and in the atmosphere.

The sun is essentially a sphere of gas heated by a nuclear fusion reaction at its center. Hot bodies emit electromagnetic radiation with a wavelength or spectral distribution determined by the body's temperature. For a perfectly absorbing or "black" body, the spectral distribution of the emitted radiation is given by Planck's radiation law (Siegel and Howell, 1972).

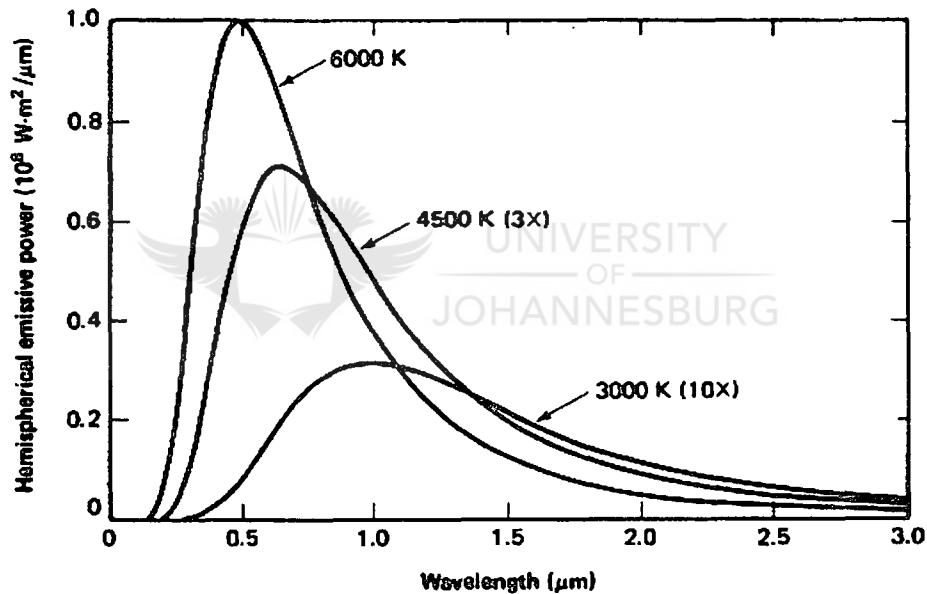


Figure 3.1: Planckian black-body radiation distributions for different black-body temperatures (Green, 1992).

As indicated in Fig 3.1, this law indicates that as a body is heated, not only does the total energy of the electromagnetic radiation emitted increase, but the wavelength of peak emission decreases. An example of this within most of our ranges of experience is that metal, when heated, glows red and then yellow as it gets hotter.

Temperatures near the sun's center are estimated to reach values around  $2 \times 10^7$  K. However, this is not the temperature that determines the characteristic electromagnetic radiation emission from the sun. Most of the intense radiation from the sun's deep interior is absorbed by a layer of negative hydrogen ions near the sun's surface. These ions act as continuous absorbers over a great range of wavelengths. The accumulation of heat in this layer sets up convective currents that transport the excess energy through the optical barrier (Fig 3.2). Once through most of this layer, the energy is re-radiated into the relatively transparent gases above. The sharply defined level where convective transport gives way to radiation is known as the photosphere. Temperatures within the photosphere are much cooler than at the sun's interior but are still a very high 6000 K. The photosphere radiates an essentially continuous spectrum of electromagnetic radiation closely approximating that expected from a black body at this temperature.

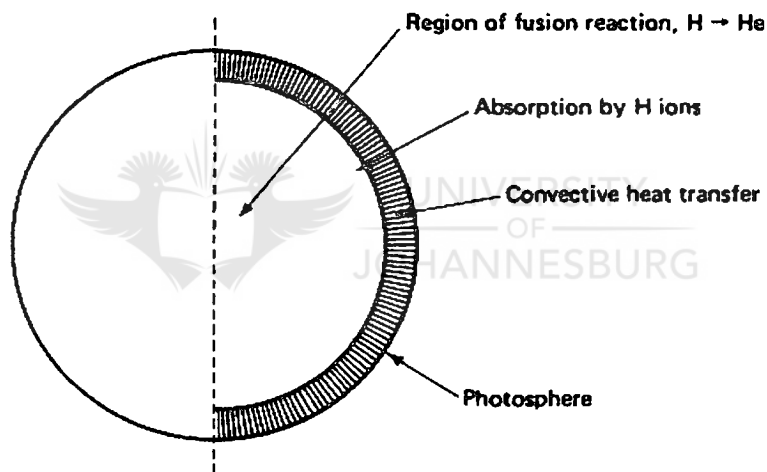


Figure 3.2: Principal features of the sun (Green, 1992).

### 3.3.2 The Solar Constant

The radiant power per unit area perpendicular to the direction of the sun outside the earth's atmosphere but at the mean earth-sun distance is essentially constant. This radiation intensity is referred to as the solar constant or, alternatively, air mass zero (AM0) radiation, for reasons that will soon become apparent.

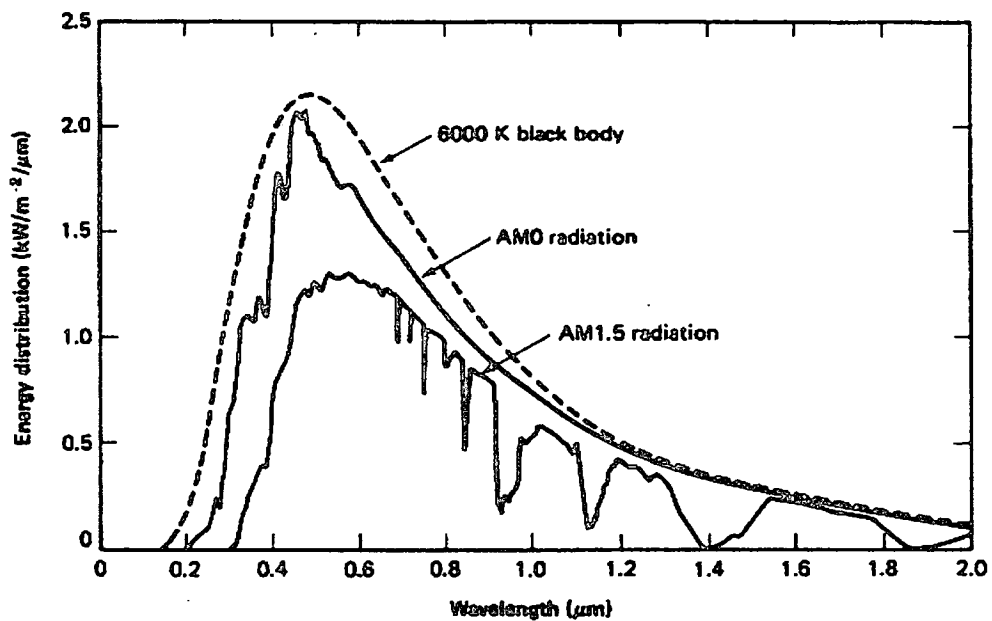


Figure 3.3: Spectral distribution of sunlight. Shown are the cases of AM0 and AM1.5 radiation together with the radiation distribution expected from the sun if it were a black body at 6000 K (Green, 1992).

The presently accepted value of the solar constant in photovoltaic work is  $1.353 \text{ kW/m}^2$ . This value has been determined by taking a weighted average of measurements made by equipment mounted on balloons, high-altitude aircraft, and spacecraft (Thekackara, 1970). As indicated by the two uppermost curves in Fig. 3.3, the spectral distribution of AM0 radiation differs from that of an ideal black body. This is due to such effects as differing transmissivity of the sun's atmosphere at different wavelengths. A knowledge of the exact distribution of the energy content in sunlight is important in solar cell work because these cells respond differently to different wavelengths of light.

### 3.3.3 Solar Intensity at the Earth's Surface

Sunlight is attenuated by at least 30% during its passage through the earth's atmosphere. Causes of such attenuation are (Gast, 1960):

- Rayleigh scattering or scattering by molecules in the atmosphere. This mechanism attenuates sunlight at all wavelengths but is most effective at short wavelengths.
- Scattering by aerosols and dust particles.

- Absorption by the atmosphere and its constituent gases-oxygen, ozone, water vapor, and carbon dioxide, in particular.

A typical spectral distribution of sunlight reaching the earth's surface is shown by the lower curve of Fig.3.3, which also indicates the absorption bands associated with molecular absorption. The degree of attenuation is highly variable. The most important parameter determining the total incident power under clear conditions is the length of the light path through the atmosphere. This is shortest when the sun is directly overhead. The ratio of any actual path length to this minimum value is known as the optical air mass. When the sun is directly overhead, the optical air mass is unity and the radiation is described as air mass one (AM1) radiation. When the sun is an angle  $\theta$  to overhead, the air mass is given by:

$$\text{Air mass} = 1/\cos \theta \quad (3.1)$$

Hence, when the sun is  $60^\circ$  off overhead, the radiation is AM2. The easiest way to estimate the air mass is to measure the length of the shadow  $s$  cast by a vertical structure of height  $h$ . Then

$$\text{Air mass} = \sqrt{1 + \left(\frac{s}{h}\right)^2} \quad (3.2)$$

With increasing air mass but with other atmospheric variables constant, the energy reaching the earth is attenuated at all wavelengths, with attenuation in the vicinity of the absorption bands of Fig.3.3 becoming even more severe. Hence, as opposed to the situation outside the earth's atmosphere, terrestrial sunlight varies greatly both in intensity and spectral composition. To allow meaningful comparison between the performances of different solar cells tested at different locations, a terrestrial standard has to be defined and measurements referred to this standard. Although the situation is in a state of flux, the most widely used terrestrial standard at the time of writing is the AM1.5 distribution, which is plotted as the terrestrial curve in Fig.3.3 In the photovoltaic program of the U.S. government, this distribution, essentially scaled up so that the total power density content is  $1 \text{ kW/m}^2$ , was incorporated as a standard in 1977 (Report ERDA/NASA, 1977). The latter power density is close to the maximum received at the earth's surface.

### 3.4 *p-n* Junction Diodes and Solar Cell Parameters

#### 3.4.1 Introduction

The most common solar cells are essentially just very large area *p-n* junction diodes, where such a diode is formed by making a junction between *n*-type and *p*-type regions. In this Section, the basic properties of such a junction will be analyzed when in the dark and when illuminated.

#### 3.4.2 Electrostatics of *p-n* Junctions

Consider isolated pieces of *n*-type and *p*-type semiconducting material as shown in Fig. 3.4. If these are brought together in a conceptual experiment, it would be expected that electrons would flow from regions of high concentration (*n*-type side) to regions of low concentration (*p*-type side) and similarly for holes. However, electrons leaving the *n*-type side will create a charge imbalance in this side by exposing ionized donors (positive charge). Similarly, holes leaving the *p*-type side will expose negative charge.

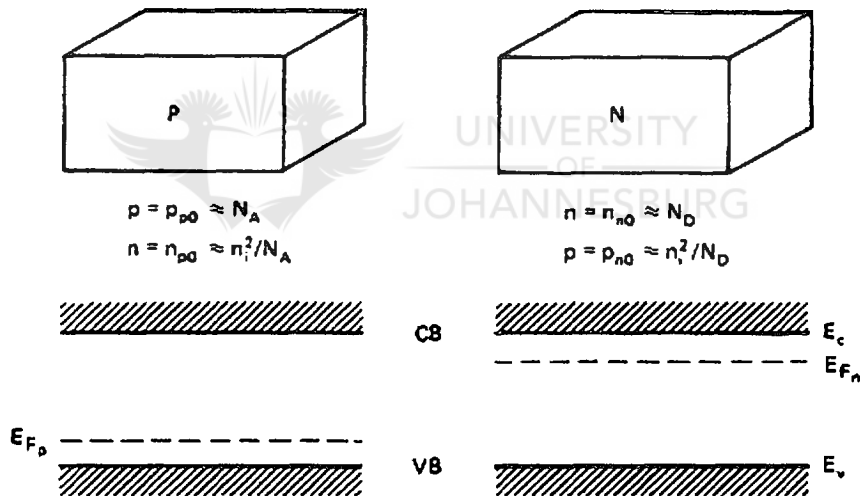


Figure 3.4: Isolated pieces of *p*-type and *n*-type semiconductor material with corresponding energy-band diagrams (Green, 1992).

These exposed charges will set up an electric field that will oppose the natural diffusion tendency of the electrons and holes and an equilibrium situation will be obtained. The characteristics of the equilibrium situation can be found by considering Fermi levels. A system in thermal equilibrium can have only one Fermi level. Far enough away from the metallurgical junction, conditions could be expected to remain unperturbed from those in isolated material. Referring to Fig. 3.5,

this means there must be a transition region near the junction in which a potential change,  $\psi_0$  occurs. The value of  $\psi_0$  can be found from this figure:

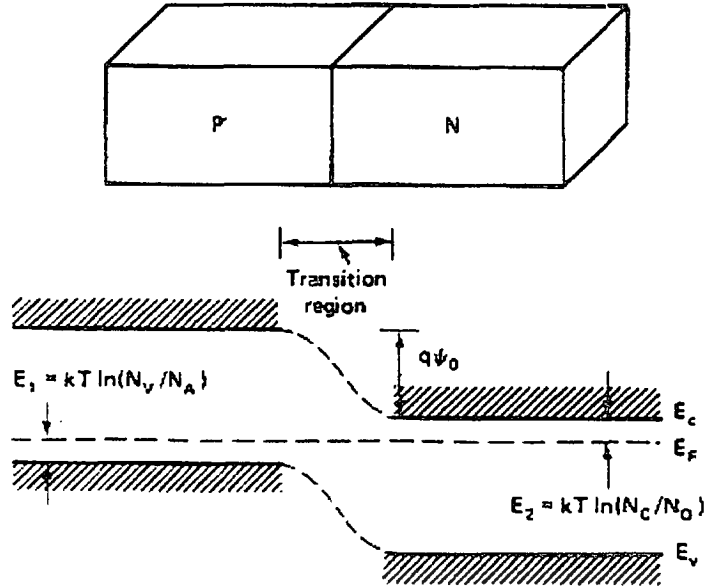


Figure 3.5: A  $p$ - $n$  junction formed by bringing the isolated  $p$ -type and  $n$ -type regions together. Also shown is the corresponding energy-band diagram at thermal equilibrium (Green, 1992).

$$q\psi_0 = E_g - E_1 - E_2 \quad (3.3)$$

The expressions for  $E_1$  and  $E_2$  are indicated in Fig.3.5. Hence,

$$\begin{aligned} q\psi_0 &= E_g - kT \ln\left(\frac{N_v}{N_A}\right) - kT \ln\left(\frac{N_C}{N_D}\right) \\ &= E_g - kT \ln\left(\frac{N_C N_v}{N_A N_D}\right) \end{aligned} \quad (3.4)$$

The intrinsic carrier concentration of a semiconductor is given by:

$$n_i^2 = N_C N_v \exp\left(-\frac{E_g}{kT}\right)$$

Therefore,

$$\psi_0 = \frac{kT}{q} \ln \left( \frac{N_A N_D}{n_i^2} \right) \quad (3.5)$$

An applied voltage,  $V_a$ , will change the potential difference between the two sides of the diodes by  $V_a$ . Hence, the potential across the transition region will become  $(\psi_0 - V_a)$ . It is instructive to plot the carrier concentrations corresponding to Fig. 3.5. These concentrations depend on the exponential of the energy difference between the Fermi level and the respective band. The resulting plot is shown in Fig.3.6 on a logarithmic scale.

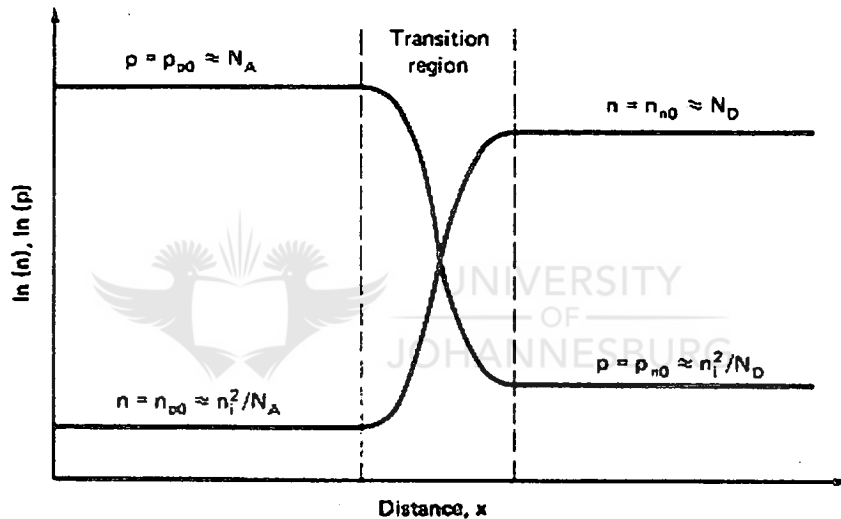


Figure 3.6: Plot of the natural logarithms of the electron and hole concentrations corresponding to Fig. 3.5. (Green, 1992).

The corresponding plot of the space-charged density,  $\rho$ , is shown as the dashed line in Fig. 3.7(a).



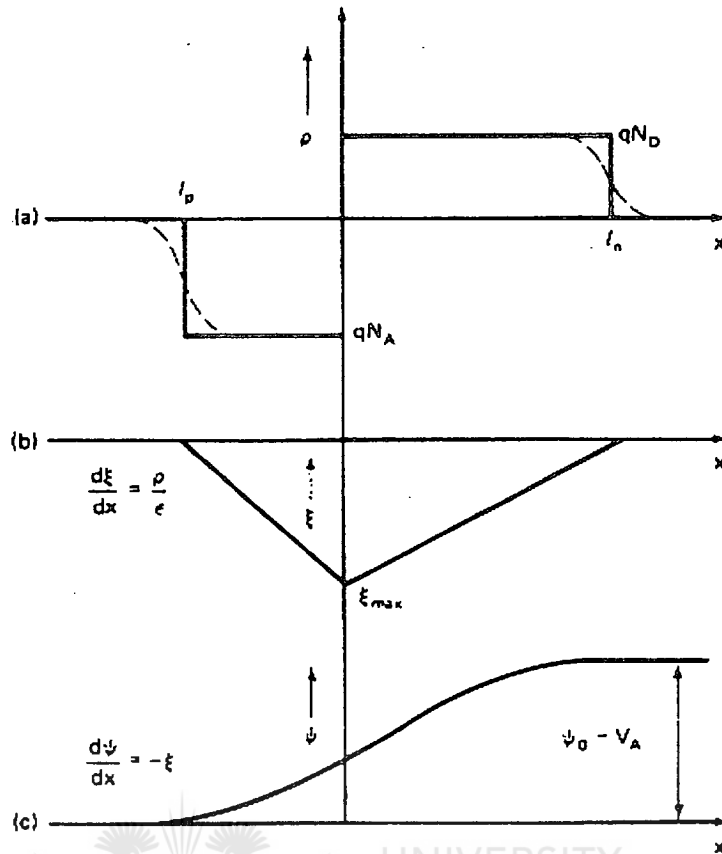


Figure 3.7: (a) Space-charge density corresponding to Fig. 3.6. The dashed line shows the actual distribution while the solid line shows the assumed distribution in the depletion approximation. (b) Corresponding electrical field strength and (c) corresponding potential distribution (Green, 1992).

The rapid change of  $\rho$  near the edge of the depletion region leads to approximation 1, the depletion approximation. In this approximation, the device is divided into two types of regions: *quasi-neutral regions* where the space-charge density is assumed zero throughout and a depletion region where the carrier concentrations are assumed so small that the only contribution to space-charge density comes from the ionized dopants. This approximation essentially just sharpens up the space-charge distribution, as indicated by the solid line in Fig. 3.7(a). With this approximation, it is a simple matter to find the electric field and potential distribution across the depletion region, as shown in Fig. 3.7(b) and (c). The space-charge distribution is just integrated successively, remembering that electric field strength is the negative gradient of potential. The results for the maximum field strength in the depletion region,  $\xi_{max}$ , the width of the depletion

region,  $W$ , and the distance this region extends on either side of the junction,  $l_n$  and  $l_p$  are (Grove, 1967).

$$\begin{aligned}\xi_{\max} &= \left[ \frac{2q}{\epsilon} (\psi_0 - V_a) \left( \frac{1}{N_A} + \frac{1}{N_D} \right) \right]^{1/2} \\ W = l_n + l_p &= \left[ \frac{2\epsilon}{q} (\psi_0 - V_a) \left( \frac{1}{N_A} + \frac{1}{N_D} \right) \right]^{1/2} \\ l_p &= W \frac{N_D}{N_A + N_D} \\ l_n &= W \frac{N_A}{N_A + N_D}\end{aligned}\tag{3.6}$$

### 3.4.3 Carrier Injection

The next calculation involves finding the concentration of carriers at the edge of the depletion region as a function of bias. Referring to Fig. 3.8, values are sought for the concentrations  $n_{pa}$  and  $p_{nb}$ . At zero bias, their values are already known (Fig.3.6):

$$\begin{aligned}p_{nb} = p_{n0} = p_{p0} \exp\left(-\frac{q\psi_0}{kT}\right) &\approx \frac{n_i^2}{N_D} \\ n_{pa} = n_{p0} = n_{n0} \exp\left(-\frac{q\psi_0}{kT}\right) &\approx \frac{n_i^2}{N_A}\end{aligned}\tag{3.7}$$

Within the depletion region, both the highest electric field strengths and concentration gradients are present. The net current flow through such regions is actually the small difference between two large terms. For holes:

$$J_h = q\mu_h p \xi - qD_h \frac{dp}{dx}\tag{3.8}$$

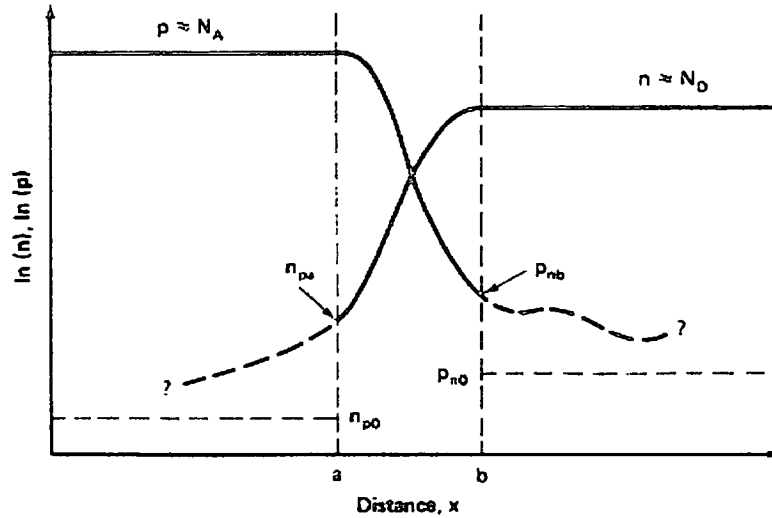


Figure 3.8: Plot of carrier concentrations when a voltage is applied to the  $p$ - $n$  junction. In the text, expressions are found for the minority carrier concentrations  $n_{pa}$  and  $p_{nb}$  at the edge of the junction depletion region. Subsequently, the precise form of the distributions shown dashed are also calculated (Green, 1992).

Both the drift and diffusion terms are large but opposing. At zero bias they balance. At moderate bias points, the net current flow is a small difference between these two much larger terms. This leads to approximation 2-that, within depletion regions,

$$q\mu_h p \xi \approx qD_h \frac{dp}{dx} \quad (3.9)$$

In other words,

$$\xi = \frac{kT}{q} \frac{1}{p} \frac{dp}{dx} \quad (3.10)$$

Making use of Einstein's relationship between  $\mu_h$  and  $D_h$  and integrating the negative of both sides of Eq. (3.10) across the depletion region gives:

$$\begin{aligned}\psi_0 - V_a &= -\frac{kT}{q} \ln p \Big|_a^b \\ &= \frac{kT}{q} \ln \frac{p_{pa}}{p_{nb}}\end{aligned}\quad (3.11)$$

or, rearranging,

$$p_{nb} = p_{pa} e^{-q\psi_0/kT} e^{qV_a/kT} \quad (3.12)$$

But from space-charge neutrality at point  $a$  and introducing approximation 3, that only cases where the carriers in the minority have a much lower concentration than those in the majority will be considered ( $p_{pa} \gg n_{pa}$ ,  $n_{na} \gg p_{na}$ ), gives

$$p_{pa} = N_A + n_{pa} \quad (\text{where } n_{pa} \text{ is small})$$

$$\approx p_{p0} \approx p_{n0} e^{q\psi_0/kT} \quad (3.13)$$


Hence,

$$\begin{aligned}p_{nb} &= p_{n0} e^{qV_a/kT} = \frac{n_i^2}{N_D} e^{qV_a/kT} \\ n_{pa} &= n_{p0} e^{qV_a/kT} = \frac{n_i^2}{N_A} e^{qV_a/kT}\end{aligned}\quad (3.14)$$

Therefore, the concentration of carriers in the minority (minority carriers) at the edge of the depletion region increases exponentially with applied voltage. The process by which this concentration is controlled by the bias across the junction is known as *minority-carrier injection*.

### 3.4.4 Dark Characteristics

#### Minority Carriers in Quasi-Neutral Regions

To summarize progress to date, it has been shown that a reasonable approximation for analysis is to divide the diode up into depletion and quasi-space-charge neutral regions. It has been found that the minority-carrier concentration at the edge of the depletion region depends exponentially on the voltage applied to the diode. This information is summarized in Fig.3.8. Moreover, it has been shown that, when quasi-neutral regions are uniformly doped and majority carrier currents small, minority carriers flow primarily by diffusion. This will allow the distributions shown dashed in Fig.3.8 to be calculated.

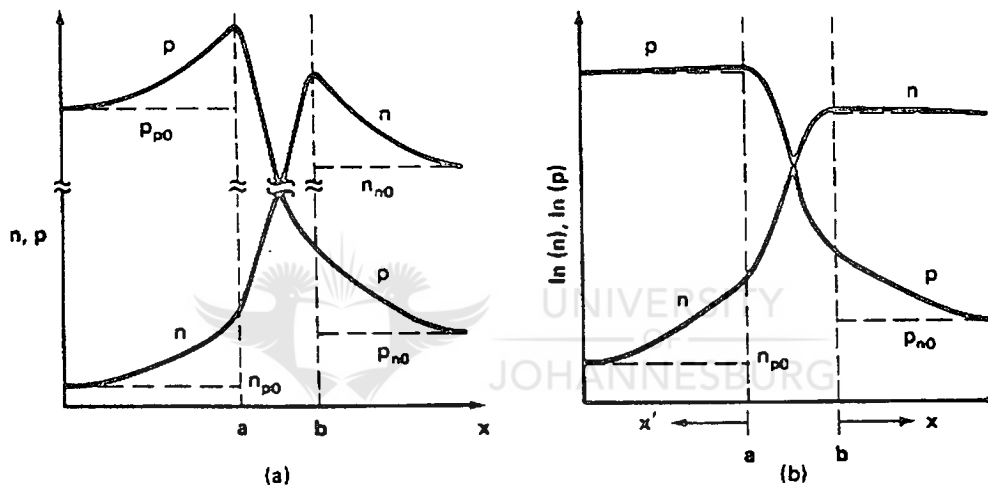


Figure 3.9: (a) Linear plot of the distributions of carriers throughout the  $p$ - $n$  junction diode under forward bias. (b) Corresponding semi-logarithmic plot. Note the differences with respect to majority carriers (Green, 1992).

On the  $n$ -type side of the diode,

$$J_h = -qD_h \frac{dp}{dx} \quad (3.15)$$

while the continuity equation gives:

$$\frac{1}{q} \frac{dJ_h}{dx} = -(U - G) \quad (3.16)$$

From the definition of carrier lifetimes:

$$\tau_e = \frac{\Delta n}{U}$$

$$\tau_h = \frac{\Delta p}{U}$$

Where  $\tau_e$  and  $\tau_h$  are lifetimes for electrons and holes,  $U$  is the net recombination rate and  $\Delta n$  and  $\Delta p$  are the disturbances of the respective carriers from their equilibrium values,  $n_0$  and  $p_0$ , the recombination rate in the  $n$ -type region can be put in the form:

$$U = \frac{\Delta p}{\tau_h} \quad (3.17)$$

where  $\Delta p$  is the excess concentration of minority-carrier holes equal to the total concentration,  $p_n$  minus the equilibrium concentration,  $p_{n0}$ .  $\tau_h$  is the minority-carrier lifetime which can be regarded as a constant, at least for small disturbances from equilibrium. Combining the three equations above gives:

$$D_h \frac{d^2 p_n}{dx^2} = \frac{p_n - p_{n0}}{\tau_h} - G \quad (3.18)$$

In the dark,  $G=0$ . Also,  $d^2 p_{n0}/dx^2=0$ . Hence Eq. (3.18) simplifies to:

$$\frac{d^2 \Delta p}{dx^2} = \frac{\Delta p}{L_h^2} \quad (3.19)$$

where

$$L_h = \sqrt{D_h \tau_h} \quad (3.20)$$

$L_h$  has the dimensions of length and is known as the diffusion length. It will become apparent that this is a very important parameter in solar cell work. The general solution to Eq. (3.19) is:

$$\Delta p = Ae^{x/L_h} + Be^{-x/L_h} \quad (3.21)$$

The constants  $A$  and  $B$  can be found by applying two boundary conditions as follows:

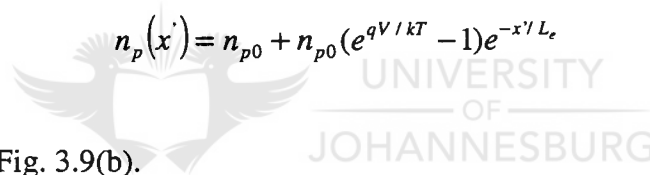
1. At  $x=0$ ,  $p_{nb}=p_{n0}e^{qV/kT}$

2.  $p_n$  finite as  $x \rightarrow \infty$ . Therefore,  $A=0$

These boundary conditions give the particular solution:

$$p_n(x) = p_{n0} + p_{n0}(e^{qV/kT} - 1)e^{-x/L_h} \quad (3.22)$$

Similarly,

$$n_p(x') = n_{p0} + n_{p0}(e^{qV/kT} - 1)e^{-x'/L_e} \quad (3.23)$$


where  $x'$  is defined in Fig. 3.9(b).

These solutions for minority-carrier concentrations throughout the device are plotted in Fig. 3.9(a). In the quasi-neutral regions, the majority-carrier concentrations must have a corresponding change in their distributions to maintain space-charge neutrality, also as shown in Fig. 3.9(a). Even though the absolute changes are the same, the relative changes in the majority changes are very much smaller, as indicated in the logarithmic plot of Fig. 3.9(b).

### Minority-Carrier Currents

It is a very simple matter to calculate minority-carrier current flows once the carrier distributions are known. Since currents are diffusive in quasi-neutral regions, on the  $n$ -type side:

$$J_h = -qD_h \frac{dp}{dx} \quad (3.24)$$

substituting Eq. (3.22) gives:

$$J_h(x) = \frac{qD_h p_{n0}}{L_h} (e^{qV/kT} - 1) e^{-x/L_h} \quad (3.25)$$

similarly, in the  $p$ -type region,

$$J_e(x') = \frac{qD_e n_{p0}}{L_e} (e^{qV/kT} - 1) e^{-x'/L_e} \quad (3.26)$$

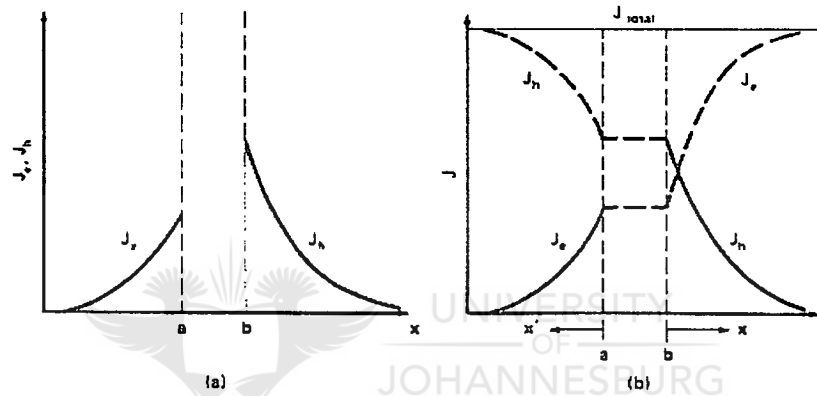


Figure 3.10: (a) Minority-carrier current densities in a  $p$ - $n$  junction diode corresponding to Fig. 3.9. (b) Distribution of minority, majority, and total current densities in the diode, neglecting recombination in the depletion region (Green, 1992).

The current distributions resulting from these expressions are plotted in Fig. 3.10(a). In order to calculate the total current flow in the diode, it is necessary to know both the electron and hole components at the same point. Considering current flows in the depletion region, the continuity equations gives:

$$\frac{1}{q} \frac{dJ_e}{dx} = U - G = -\frac{1}{q} \frac{dJ_h}{dx} \quad (3.27)$$

Hence, the magnitude of the change in current across the depletion region is:



$$\delta J_e = |\delta J_h| = q \int_{-W}^0 (U - G) dx \quad (3.28)$$

$W$  is generally much less than  $L_e$  and  $L_h$ , the characteristic decay lengths of  $J_e$  and  $J_h$ . This indicates that Fig. 3.10(a) is grossly out of proportion. Since  $W$  is small, a reasonable approximation is to assume that the integral involved in Eq. (3.28) is negligible, so that

$$\delta J_e = |\delta J_h| \approx 0$$

It follows that  $J_e$  and  $J_h$  are essentially constant across the depletion region as shown in Fig. 3.10(b). This approximation, approximation 5, would appear more reasonable if  $W$  were drawn to scale. The total current can now be found since both  $J_e$  and  $J_h$  are known at all points in the depletion region. Hence,

$$\begin{aligned} J_{total} &= J_e|_{x=0} + J_h|_{x=0} \\ &= \left( \frac{qD_e n_{p0}}{L_e} + \frac{qD_h p_{n0}}{L_h} \right) (e^{qV/kT} - 1) \end{aligned} \quad (3.29)$$

Since  $J_{total}$  is constant with position, it is now possible to complete the distributions of  $J_e$  and  $J_h$  throughout the diode as shown by the dashed lines of Fig. 3.10(b). The result of the analysis has been the derivation of the ideal diode law:

$$I = I_0 (e^{qV/kT} - 1) \quad (3.30)$$

The expression derived for the saturation current density is:

$$I_0 = A \left( \frac{qD_e n_i^2}{L_e N_A} + \frac{qD_h n_i^2}{L_h N_D} \right) \quad (3.31)$$

where  $A$  is the cross-sectional area of the diode.

### 3.4.5 Solar Cell Output Parameters

Three parameters are usually used to characterize solar cell outputs (Fig.3.11). One of these is the short-circuit current,  $I_{sc}$ . Ideally, this is equal to the light-generated current  $I_L$ . A second parameter is the open-circuit voltage,  $V_{oc}$ . Setting  $I$  to zero in  $I = I_0(e^{qV/kT} - 1) - I_L$  gives the ideal value:

$$V_{oc} = \frac{kT}{q} \ln\left(\frac{I_L}{I_0} + 1\right) \quad (3.32)$$

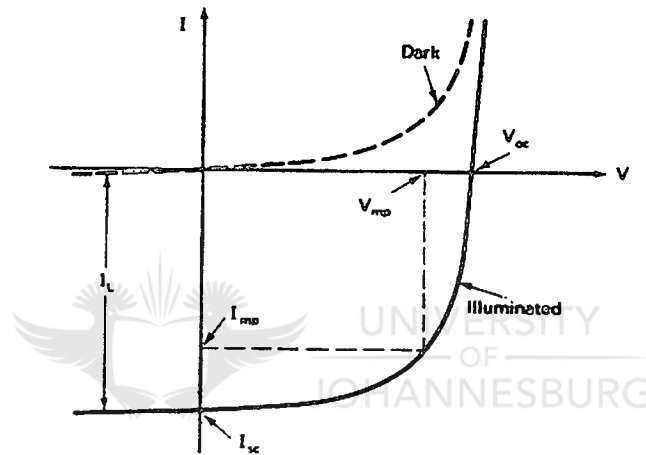


Figure 3.11: Terminal properties of a  $p$ - $n$  junction diode in the dark and when illuminated (Green, 1992).

$V_{oc}$  is determined by the properties of the semiconductor by virtue of its dependence on  $I_0$ . The power output for any operating point in the fourth quadrant is equal to the area of the rectangle indicated in Fig. 3.11. One particular operating point ( $V_{mp}$ ,  $I_{mp}$ ) will maximize this power output. The third parameter, the fill factor,  $FF$ , is defined as:

$$FF = \frac{V_{mp} I_{mp}}{V_{oc} I_{sc}} \quad (3.33)$$

It is a measure of how “square” the output characteristics are. For cells of reasonably efficiency, it has a value in the range 0.7 to 0.85. Ideally, it is a function only of the open-circuit voltage,

$V_{oc}$ . Defining a normalized voltage,  $v_{oc}$ , as  $V_{oc}/(kT/q)$ , the ideal (maximum) value of  $FF$  is shown in Fig. 3.12. An empirical expression describing this relationship to about four significant digits for  $v_{oc} > 10$  is (Green, 1992):

$$FF = \frac{v_{oc} - \ln(v_{oc} + 0.72)}{v_{oc} + 1} \quad (3.34)$$

The energy-conversion efficiency,  $\eta$ , is then given by:

$$\eta = \frac{V_{mp} I_{mp}}{P_{in}} = \frac{V_{oc} I_{sc} FF}{P_{in}} \quad (3.35)$$

where  $P_{in}$  is the total power in the light incident on the cell. Energy-conversion efficiencies of commercial solar cells generally lie in the 12 to 14% range.

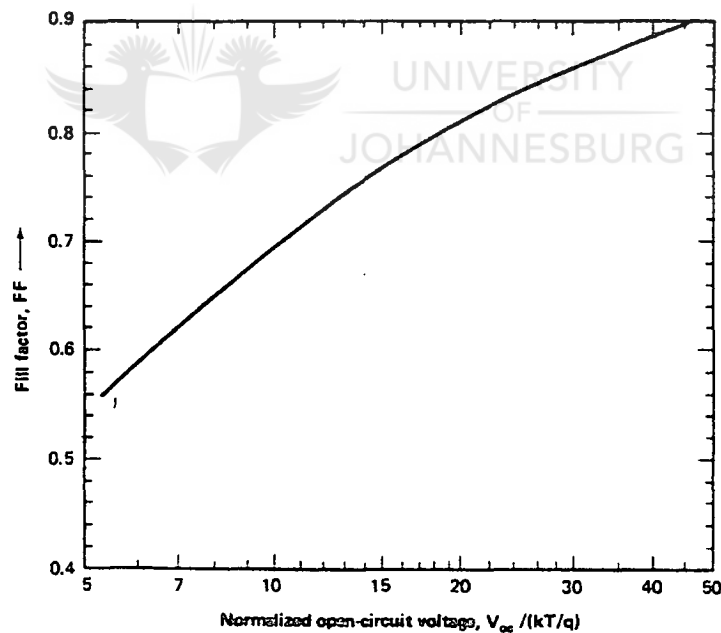


Figure 3.12: Ideal value of the fill factor as a function of the open-circuit voltage normalized to the thermal voltage,  $kT/q$  (Green, 1992).

## 3.5 Efficiency Limits

### 3.5.1 Introduction

In the previous section it was seen that three parameters could be used to characterize the performance of a  $p$ - $n$  junction solar cell. These are the open-circuit voltage ( $V_{oc}$ ), the short-circuit current ( $I_{sc}$ ), and the fill factor ( $FF$ ). It was indicated that the maximum value of the fill factor is a function of  $V_{oc}$ . In this Section, the ideal limits of  $I_{sc}$  and  $V_{oc}$  will be discussed.

### 3.5.2 Short-Circuit Current

It is relatively easy to calculate the upper limit to the short-circuit current obtainable from any selected solar cell material. Under ideal conditions, each photon incident on the cell of energy greater than the band gap gives rise to one electron flowing in the external circuit. Hence, to calculate the maximum  $I_{sc}$ , the photon flux in sunlight must be known. This can be calculated from the energy distribution of sunlight by dividing the energy content at a given wavelength by the energy of an individual photon ( $hf$  or  $hc/\lambda$ ) of this wavelength. The results of such a calculation are shown in Fig. 3.13(a) for AM0 radiation and the standard terrestrial AM1.5 radiation mentioned in Sections 3.3.2 and 3.3.3.

The maximum  $I_{sc}$  is then found by integrating these distributions from low wavelengths up to the maximum wavelength for which electron-hole pairs can be generated for a given semiconductor. It is not surprising that as the band gap decreases, the short-circuit current density increases. More photons have the energy required to create an electron-hole pair as the band gap becomes smaller.

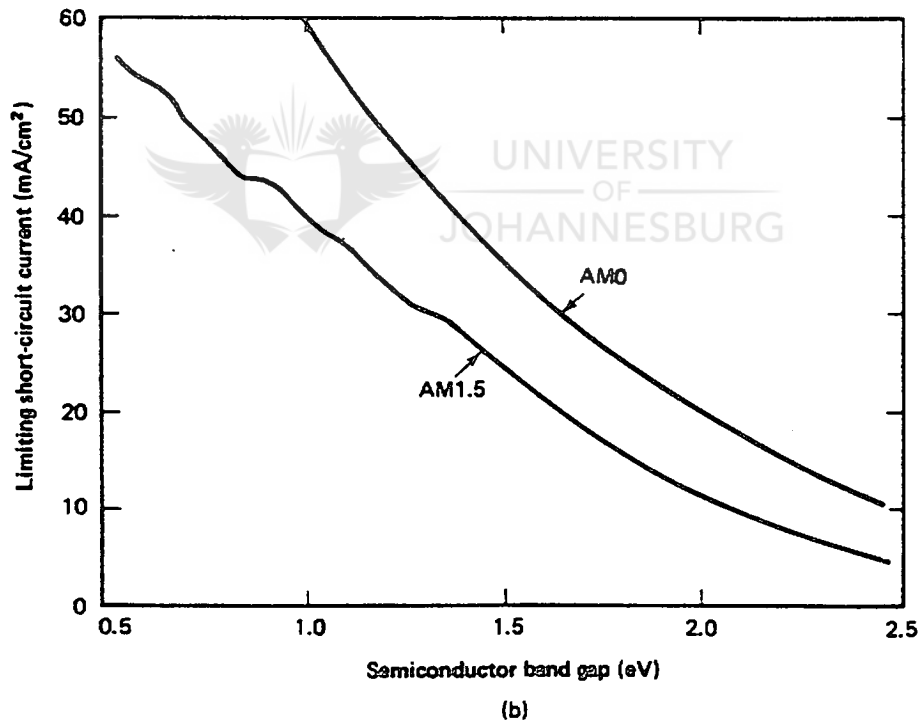
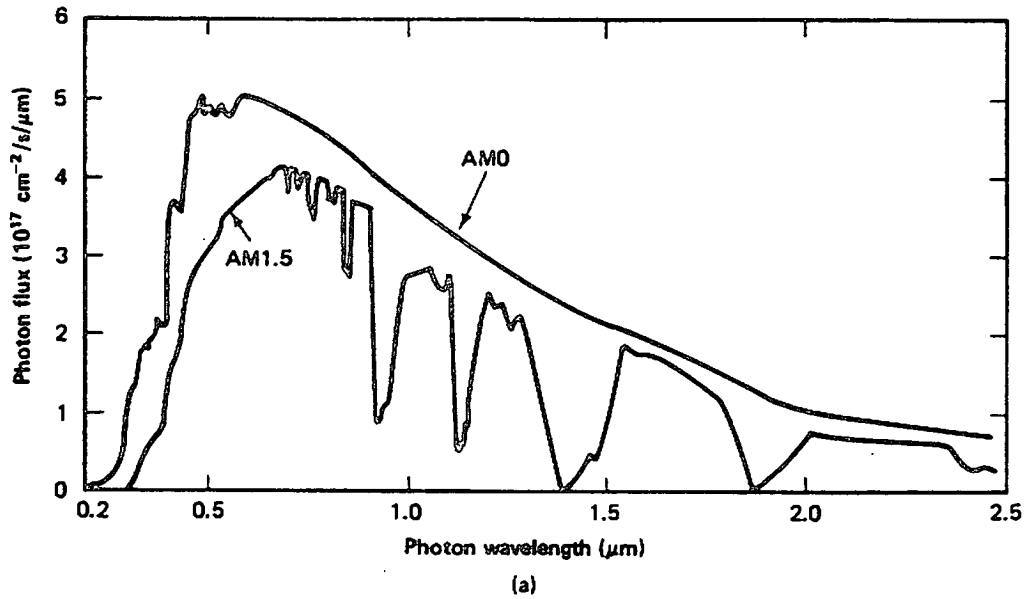


Figure 3.13: (a) Photon flux in sunlight corresponding to the AM0 and AM1.5 energy distributions given in Fig. 3.3. (b) Corresponding upper limits on the short-circuit current density as a function of the energy band gap of the solar cell material (Green, 1992).

### 3.5.3 Open-Circuit Voltage and Efficiency

The fundamental limitations on the open-circuit voltages of solar cells are not as clearly defined. In Section 3.4.5, it was shown that, for an ideal  $p$ - $n$  junction cell,  $V_{oc}$  was given by:

$$V_{oc} = \frac{kT}{q} \left( \frac{I_L}{I_0} + 1 \right) \quad (3.36)$$

where  $I_L$  is the light-generated current and  $I_0$  is the diode saturation current calculated as:

$$I_0 = A \left( \frac{qD_e n_i^2}{L_e N_A} + \frac{qD_h n_i^2}{L_h N_D} \right) \quad (3.37)$$

$I_0$  needs to be as small as possible for maximum  $V_{oc}$ . One approach to calculating upper limits on  $V_{oc}$  (and hence efficiency) is to assign favorable values to the semiconductor parameters in Eq. (3.37) while still keeping them within the range expected to be required to produce good solar cells (Hovel, 1975). For silicon, this gives a maximum  $V_{oc}$  of about 700 mV. The corresponding maximum fill factor is 0.84. Combining with the results of the preceding section for  $I_{sc}$  allows the maximum energy-conversion efficiency to be found.

The parameter in Eq. (3.37) which depends most strongly on the choice of semiconductor material is the square of the intrinsic concentration,  $n_i^2$ . Is known from the theory that:

$$n_i^2 = N_C N_V \exp\left(-\frac{E_g}{kT}\right) \quad (3.38)$$

A reasonable estimate of the minimum value of the saturation current density, as a function of band gap, from Eq. (3.37) is:

$$I_0 = 1.5 \times 10^5 \exp\left(-\frac{E_g}{kT}\right) \quad \text{A/cm}^2 \quad (3.39)$$

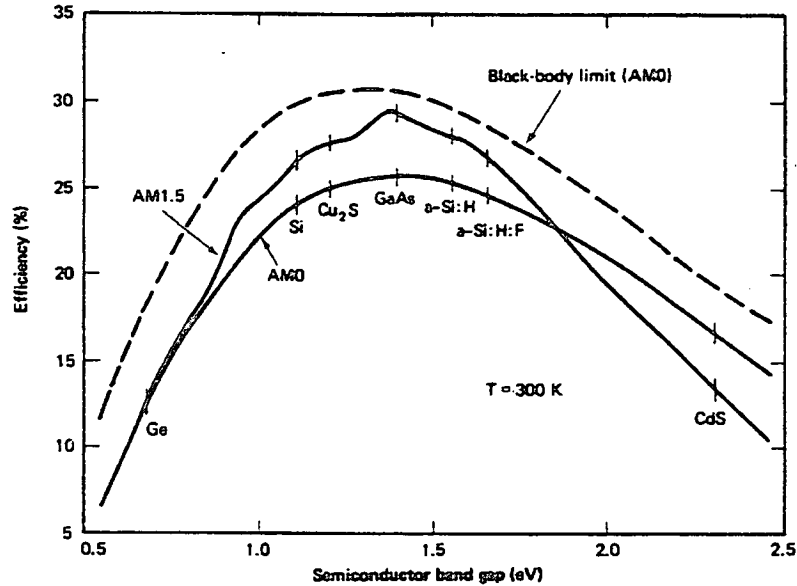


Figure 3.14: Solar cell efficiency limits as a function of the band gap of the cell material. The solid lines are semi-empirical limits for AM0 and AM1.5 illumination; the dashed line is based on thermodynamic considerations for black-body solar cells under AM0 radiation (Green, 1992).

This relationship ensures that the maximum value of  $V_{oc}$  decreases with decreasing band gap. This trend is opposite from that observed for  $I_{sc}$ . It follows that there will be an optimum-band-gap semiconductor for highest efficiency. This is demonstrated in Fig. 3.14, which shows maximum energy-conversion efficiency calculated as outlined above as a function of band gap. The peak efficiency occurs for a band gap in the range 1.4 to 1.6eV and increases from 26 to 29% as the air mass increases from 0 to 1.5. A major contributor to these relatively low maximum efficiencies is the fact that each photon absorbed creates one electron-hole pair regardless of its energy. The electron and hole quickly relax back to the band edges, emitting phonons (Fig.3.15). Even though the photon's energy may be much larger than the band gap, the resulting electron and hole effectively are separated by only the latter energy. This effect alone limits the maximum achievable efficiency to about 44% (Shockley and Queisser, 1961). The other major contributor is that even though the generated carriers are separated by a potential corresponding to the band-gap energy,  $p-n$  junction cells are inherently capable of giving a voltage output only a fraction of this potential.

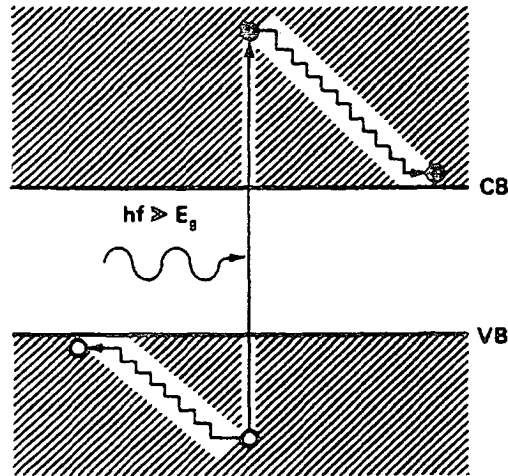


Figure 3.15: One of the major loss mechanisms in solar cells. An electron-hole pair created by a high-energy photon quickly “thermalizes” or relaxes back to the edges of the respective carrier bands. The energy wasted is dissipated as heat (Green, 1992).

The foregoing discussion is limited to the case of an individual cell exposed directly to sunlight. Experimentally, devices of this type based on GaAs have exceeded 20% efficiency. An efficiency of 28.5% was reported in 1978 (Moon, 1978) for a system involving multiple cells. Despite the low maximum-efficiency values, solar cells remain the most efficient way yet demonstrated of converting sunlight to electricity.

### 3.6 Efficiency Losses

#### 3.6.1 Introduction

It is important to realize that actual solar cell devices are significantly less efficient than the ideal limits discussed in the previous section. This is due to various additional loss mechanisms present in the cell during operation. A knowledge of these loss mechanisms is critically in order to design solar cell devices with optimum performance.

#### 3.6.2 Short-Circuit Current Losses

There are three types of losses in solar cells, which could be described as being of an “optical” nature:

- Semiconductors are in general quite reflective. These reflection losses can be reduced to about 10% by the use of an antireflection coating (Fig.3.16).



- The necessity of making electrical contact to both  $p$ - and  $n$ -type regions of solar cells generally results in a metal grid contact on the side of the cell exposed to sunlight. This blocks 5 to 15% of the incoming light.
- Finally, if the cell is not thick enough, some of the light of appropriate energy that does get coupled into the cell will pass straight out the back. This determines the minimum thickness of semiconductor material required. Indirect-band-gap semiconductors require more material than direct-gap materials.

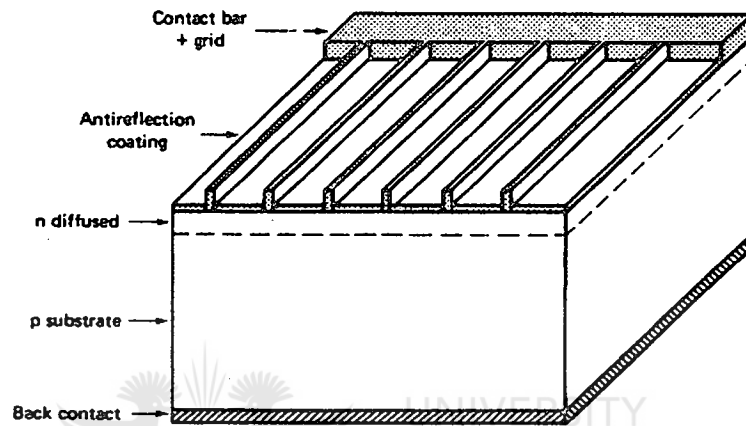


Figure 3.16: Major features of a solar cell. Dimensions in the vertical direction are exaggerated compared to lateral dimensions for the purposes of illustration (Green, 1992).

Another source of  $I_{sc}$  loss is recombination in the bulk semiconductor and at surfaces. It was indicated in previous sections that only electron-hole pairs generated near the  $p$ - $n$  junction itself contribute to  $I_{sc}$ . Carriers generated well away from the junction have a high probability of recombining before they complete the trip from the point of generation to the device terminals.

### 3.6.3 Open-Circuit Voltage Losses

The fundamental process determining  $V_{oc}$  is recombination in the semiconductor. This is brought out by the approach to calculating limits on  $V_{oc}$ . The lower the recombination rate in the semiconductor, the higher is  $V_{oc}$ . Both bulk and surface recombination are important. One important effect that can limit  $V_{oc}$  is recombination through trapping levels in depletion regions. This recombination mechanism is particularly effective in such regions. The expression for this mechanism is given by:

$$U = \frac{np - n_i^2}{\tau_{h0}(n + n_1) + \tau_{e0}(p + p_1)} \quad (3.40)$$

This rate will have its peak value when both  $n_1$  and  $p_1$  are small and both  $n$  and  $p$  are small. Both these conditions occur for traps located near the mid-gap within the depletion region. In the analysis of the dark characteristics of  $p$ - $n$  diodes in previous Sections, recombination in depletion regions was neglected on the basis of the depletion-layer width,  $W$ , being very small (approximation 5). However, the enhanced value of recombination in this region can make it quite important in some situations. Including such depletion-region recombination adds an additional term to the dark current-voltage characteristics, which then become:

$$I = I_0(e^{qV/kT} - 1) + I_w(e^{qV/2kT} - 1) \quad (3.41)$$

where  $I_0$  has the same value as before and  $I_w$  has the value (Sah, 1957):

$$I_w = \frac{qAn_i\pi}{2\sqrt{\tau_{e0}\tau_{h0}}} \frac{kT}{q\xi_{\max}} \quad (3.42)$$

where  $\xi_{\max}$  is the maximum electric field strength in the junction. Its value is given by Eq. (3.6) for junctions uniformly doped on each side.

These characteristics are plotted on a semi-logarithmic plot in Fig.3.17. The second term of Eq. (3.41) dominates at low currents, the first at high currents. It is possible to write Eq. (3.41) in the form:

$$I = I_0'(e^{qV/nkT} - 1) \quad (3.43)$$

where  $n$  is known as the *ideality factor*. It varies with the current level as does  $I_0'$ . From Eq. (3.41),  $n$  decreases from 2 at low currents to 1 at higher currents. Since the illuminated solar cell characteristics are those of Fig.3.17 shifted down into the fourth quadrant, it can be seen that the presence of this additional depletion-region recombination current can act to decrease  $V_{oc}$ .

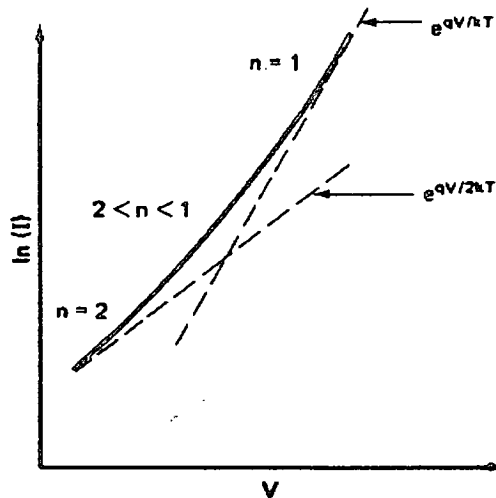


Figure 3.17: Semi-logarithmic plots of the dark current-voltage characteristics of a  $p$ - $n$  junction diode in the dark, including the effect of recombination in the depletion region (Green, 1992).

### 3.6.4 Fill Factor Losses

Recombination in the depletion region can also reduce the fill factor. If the ideality factor,  $n$ , of the preceding Section is greater than unity, the fill factor is that calculated for the ideal case (Fig.3.12) at a voltage  $V_{oc}/n$ . This will give a lower value than when  $n$  equals unity.

Defining the normalized voltage,  $v_{oc}$ , as  $V_{oc}/(nkT/q)$  in this more general case, the empirical expression for the fill factor given in Section 3.4.5 remains valid with an accuracy of about four significant digits for  $v_{oc} > 10$  (Green, 1992):

$$FF_0 = \frac{v_{oc} - \ln(v_{oc} + 0.72)}{v_{oc} + 1} \quad (3.44)$$

Solar cells generally have a parasitic series and shunt resistance associated with them, as indicated in the solar cell equivalent circuit of Fig. 3.18. There are several physical mechanisms responsible for these resistances. The major contributors to the series resistance,  $R_s$ , are the bulk resistance of the semiconductor material making up the cell, the bulk resistance of the metallic contacts and interconnections, and the contact resistance between the metallic contacts and the semiconductor. The shunt resistance,  $R_{SH}$ , is caused by leakage across the  $p$ - $n$  junction around the

edge of the cell and in nonperipheral regions in the presence of crystal defects and precipitates of foreign impurities in the junction region. Both types of parasitic resistances act to reduce the fill factor, as indicated in Fig. 3.19. Very high values of  $R_S$  and very low values of  $R_{SH}$  can also reduce  $I_{sc}$  and  $V_{oc}$ , respectively, as indicated.

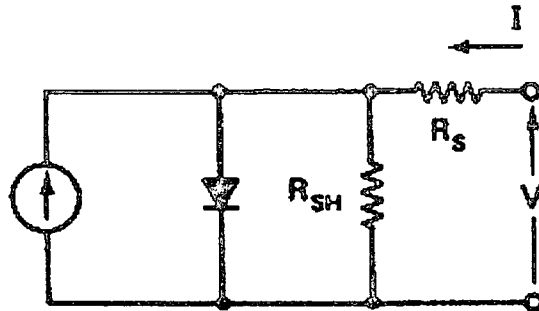


Figure 3.18: Equivalent circuit of a solar cell (Green, 1992).

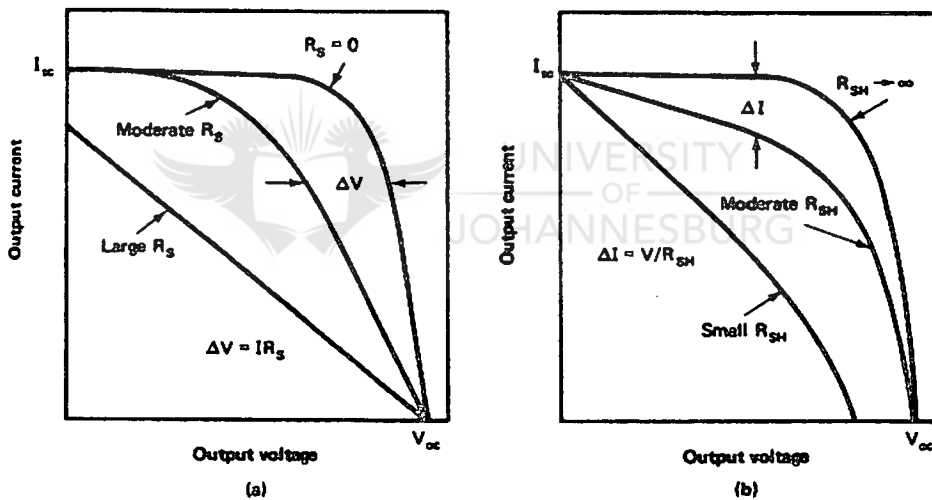


Figure 3.19: Effect of parasitic resistances on the output characteristics of solar cells: (a) Effect of series resistance,  $R_S$  and (b) effect of a shunt resistance,  $R_{SH}$ . (Green, 1992).

The magnitude of the effect of  $R_S$  and  $R_{SH}$  on the fill factor can be found by comparing their values to the characteristic resistance of a solar cell defined as (Green, 1977):

$$R_{CH} = \frac{V_{oc}}{I_{sc}} \quad (3.45)$$

If  $R_S$  is a lot less than this quantity or  $R_{SH}$  a lot larger, there will be little effect upon the fill factor. Defining a normalized resistance,  $r_s$ , as  $R_S / R_{CH}$ , an approximate expression for the fill factor in the presence of series resistance is (precise values are given in Fig. 3.20):

$$FF = FF_0(1 - r_s) \tag{3.46}$$

Where  $FF_0$  represents the ideal fill factors in the absence of parasitic resistance as approximated quite closely by Eq. (3.44). This expression is accurate to close to two significant digits for  $v_{oc} > 10$  and  $r_s < 0.4$ . Defining a normalized shunt resistance,  $r_{sh}$ , as  $R_{SH} / R_{CH}$ , a corresponding expression for the effect of shunt resistance, also involving the normalized voltage  $v_{oc} = V_{oc} / (nkT/q)$ , is (exact values are again given in Fig. 3.20):

$$FF = FF_0 \left\{ 1 - \frac{(v_{oc} + 0.7) FF_0}{v_{oc} r_{sh}} \right\} \tag{3.47}$$

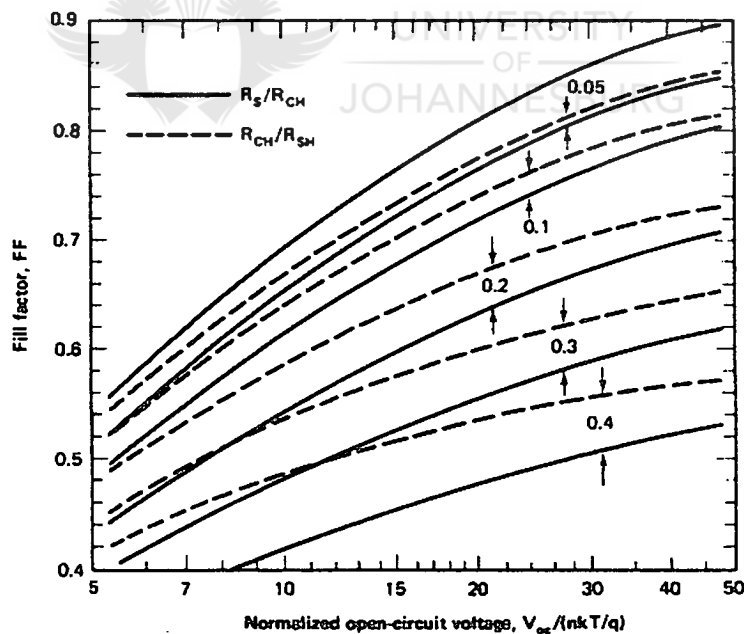


Figure 3.20: General curves for solar cell fill factors as a function of normalized open-circuit voltage. The solid curves show the fill factor as a function of normalized series resistance,  $R_S/R_{CH}$ , where  $R_{CH} = V_{oc}/I_{sc}$ . The dashed curves show the effect of shunt resistance. The normalized parameter in this case is  $R_{CH}/R_{SH}$  (Green, 1992).

## References

P. R. Gast (1960) Handbook of Geophysics, New York, p14-16 and 16-30.

M. A. Green (1977) Solid-State Electronics **20**, p 265-266.

M. A. Green (1992) Solar Cells, Prentice-Hall, New York.

A. S. Grove (1967) Physics and Technology of Semiconductor Devices, New York, p 158.

H. J. Hovel (1975) Solar Cells, vol.11, Semiconductors and Semimetals Series.

R. L. Moon (1978) Conference Record, 13<sup>th</sup> IEEE Photovoltaic Specialists Conference, Washington, D.C., p 859-867.

C. T. Sah (1957) Proceedings of the IRE **45**, p 1228-1243.

W. Shockley and H. J. Queisser (1961) Journal of Applied Physics **32**, p 510-519.

R. Siegel and J. R. Howell (1972) Thermal Radiation Heat Transfer, New York: Mc Graw-Hill.

M. P. Thekackara (1970) NASA Technical report No. R-351.



## CHAPTER 4

### EXPERIMENTAL PROCEDURES

#### 4.1 Introduction

The production of thin film solar cell devices is rather complex and involves a large number of processing steps (see Fig. 2.1). In this Chapter, the various processing steps as well as the specific experimental details followed during the deposition of the respective thin films (i.e. Mo, CuInSe<sub>2</sub>, CdS, and ZnO), are described in detail. Other important aspects such as substrate preparation and metallic/semiconductor contact formation are also dealt with. Another important aspect of this study was the accurate characterization of these semiconductor thin films. A large number of structural, optical and electrical characterization techniques were used in this study and are discussed in this Chapter.

#### 4.2 Substrate Preparation

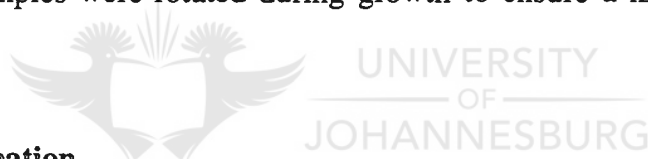
All films considered in this study were deposited on soda-lime glass substrates. The substrates had dimensions of approximately  $76 \times 15 \times 1 \text{ mm}^3$ . As in any thin film deposition process, the quality of the substrate, prior to growth is a crucial factor which influence the material properties of the deposited films. Surface defects such as scratches on the glass have an adverse effect on the structural properties of the thin films. The use of dirty substrates normally result in active layers with poor adhesion properties. The former problem can be solved by mechanical polishing of samples. In order to obtain glass substrates with a high degree of chemical cleanliness, the following procedure is routinely followed in our laboratories:

- Glass samples are ultrasonically cleaned in a soap solution for 10 minutes.
- Substrates are washed under running deionized water for 5 minutes.
- Samples are ultrasonically cleaned in deionized water for 10 minutes.
- Substrates are ultrasonically cleaned in acetone, methanol and deionized water for 10 minutes, 15 minutes and 10 minutes, respectively.
- Glass substrates are spin dried in an argon atmosphere at 80°C.

If necessary, the last two steps can be repeated several times. At least 10 samples are cleaned simultaneously and are kept under clean conditions until being loaded into the vacuum systems.

### **4.3 Molybdenum Deposition**

The first step in the fabrication process is the deposition of a Mo layer on the glass substrates. In this study, high quality Mo thin films (approximately 1  $\mu\text{m}$ ) were obtained by electron-beam evaporation. Vacuum melted Mo pellets of 99.99% purity were used during the deposition process. Depositions were carried out at a pressure of about  $10^{-6}$  mbar and the thicknesses of the Mo layers were measured by a quartz crystal monitor. The most crucial factor controlling the final quality of the Mo films was the substrate temperature during growth. Films with superior structural properties (i.e. smooth, uniform films with good adhesion properties) could only be obtained at substrate temperatures above 200°C. In addition, it was found necessary to preheat the samples at elevated temperatures for at least 3 hours in order to obtain high quality material. Up to 20 glass substrates were loaded during each run and the samples were rotated during growth to ensure a high degree of thickness uniformity.



### **4.4 Absorber Formation**

As pointed out in Section 2.5.2, a large number of deposition technologies can be used for the production of device quality  $\text{CuInSe}_2$  absorber films. In this study, a relatively simple and easily scalable two-stage processing approach was used to produce the absorber films. In this approach, various metallic precursors were prepared by thermal evaporation from specially designed graphite heaters. The second step involved the reaction of these metallic alloys to a reactive  $\text{H}_2\text{Se}/\text{Ar}$  atmosphere or elemental Se vapour. In this Section, the experimental details followed during the different stages of absorber formation are outlined.

#### **4.4.1 Precursor Formation**

During this stage of the process, Cu and  $\text{In}_2\text{Se}_3$  layers were deposited sequentially by means of thermal evaporation onto the Mo-coated glass substrates. The homogeneous evaporation of these materials onto large area substrates is quite complicated and therefore requires innovative system designs. In order to accomplish this task, a vacuum system was designed and constructed in this study.



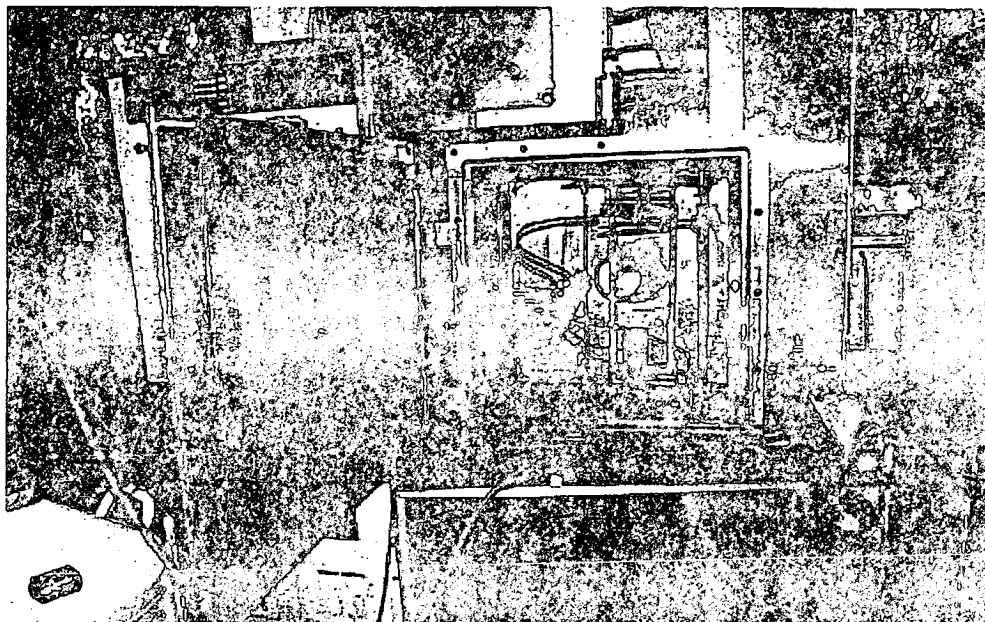


Figure 4.1: Evaporation system used in this study for the deposition of precursor alloys.

The most important features of this system are illustrated in Fig. 4.1. The system was pumped down to pressures below  $10^{-6}$  mbar with standard mechanical and diffusion pumps. During depositions stable pressures around  $5 \times 10^{-5}$  mbar were maintained. In order to ensure uniform heating of the glass substrates during evaporation, a specially designed plate-like graphite substrate heater was employed (Fig. 4.2(a)). The substrate heater (H) was positioned directly above (about 5 cm away) the substrate holder (S), and a J-type thermocouple (T) through the centre of the substrate heater made direct contact with the glass substrates. A molybdenum heat shield (M) was placed above the graphite heater to ensure maximum heat transfer towards the glass substrates. The evaporation rate and thicknesses of the respective layers were measured by a quartz crystal monitor. The quartz crystal (Q) was mounted in close vicinity of the substrate holder (Fig. 4.2(a)) to ensure maximum accuracy. Cu and  $\text{In}_2\text{Se}_3$  of high purity (99.999%) were sequentially evaporated from graphite crucibles, positioned symmetrically within cylindrical-shaped graphite heaters.

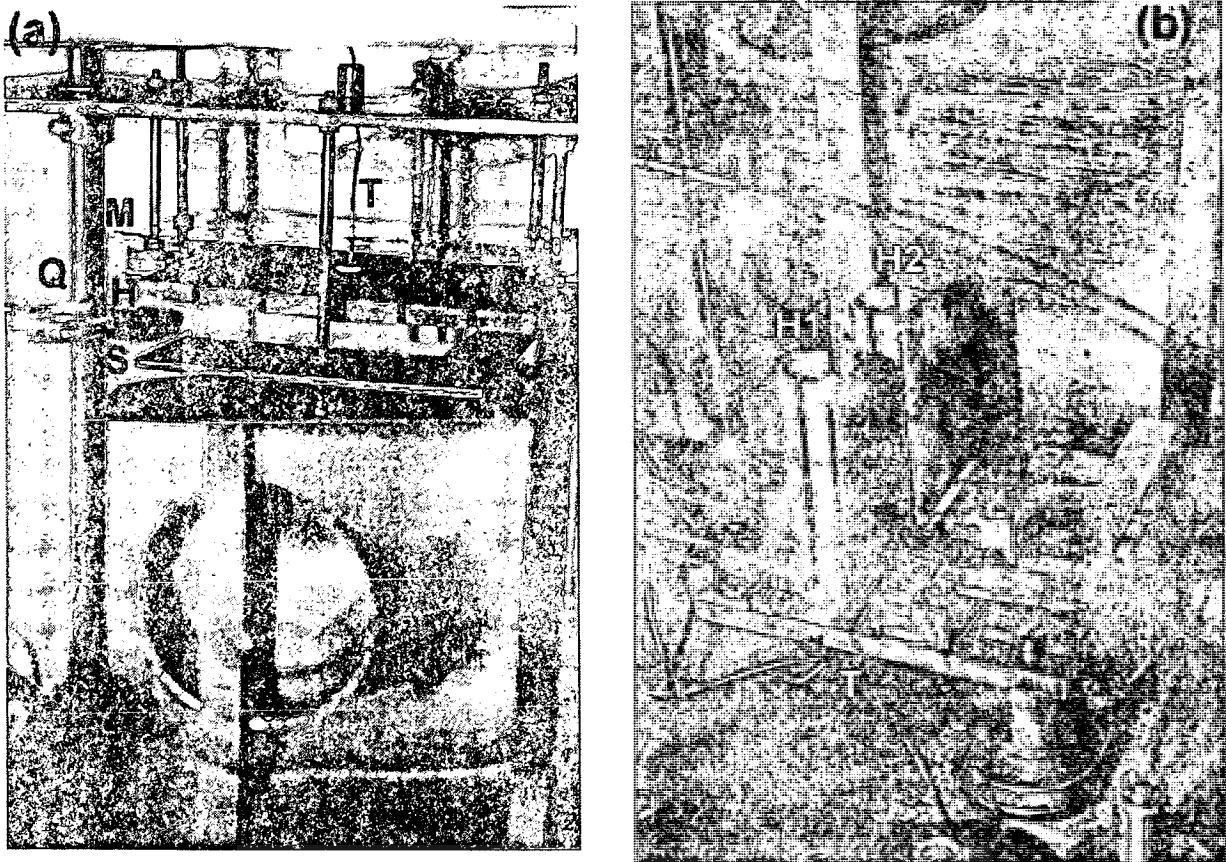


Fig. 4.2: Representation of the (a) substrate heater and (b) cylindrical-shaped evaporation sources, which are essential components of the vacuum system depicted in Fig. 4.1

The heaters (H1 and H2 in Fig. 4.2 (b)) are separated by about 3 cm and are positioned directly below (about 40 cm) the substrate holder. The graphite heaters were also shielded by molybdenum heat shields in order to reach temperatures above 1500°C. In order to obtain uniform evaporation conditions, it was essential to optimize the heating profile for each material. Programmable temperature controllers were used for this purpose and several heating steps were incorporated to ensure precise temperature control of the graphite crucibles. The temperatures of the crucibles were accurately monitored by S-type thermocouples (T), positioned in small holes at the bottom of the crucibles. The crucibles were slowly heated in 5 minutes to 200°C for 10 minutes during the first step. Thereafter, the temperature was increased in 2 minutes to 500°C and kept at that temperature for at least 10 minutes. This step was necessary to remove contaminants (especially Se) from the crucible surfaces and especially the evaporation materials, prior to film deposition. In the case of  $\text{In}_2\text{Se}_3$ , the crucible temperature was increased in 10 minutes to 780°C, which resulted in a

constant evaporation rate around  $1\text{nm sec}^{-1}$ . In the case of Cu, the crucible temperatures was kept constant at  $1350^{\circ}\text{C}$  to ensure uniform evaporation rates around  $1\text{nm sec}^{-1}$ . It is important to mention that the shutter was opened only once the final temperature set points were reached and stable growth rates were established. The shutter was manually open and closed during the growth of the respective layers. Figure 4.3 is a schematic representation of the various precursor structures produced in this study.

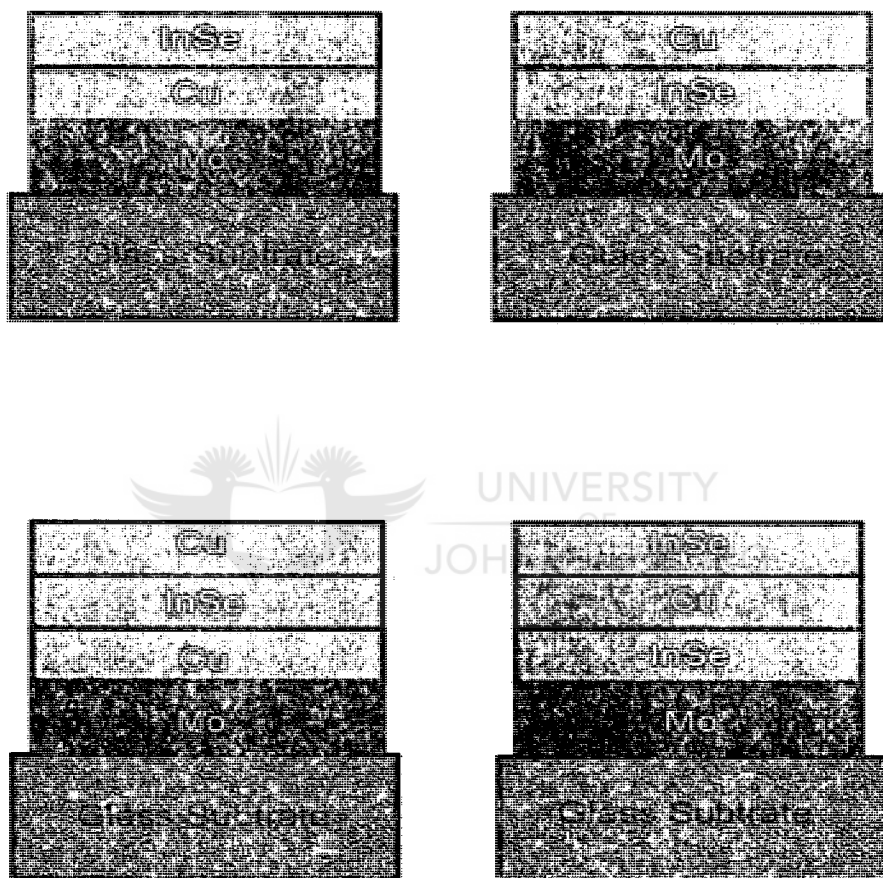


Fig. 4.3: Schematic representation of the precursor films deposited in this study. Irrespective of the stacking order, the thicknesses of the Cu and InSe layers were kept constant at 200nm and  $2\mu\text{m}$ , respectively in order to obtain near-stoichiometric films. The substrate temperature was maintained at  $200^{\circ}\text{C}$ .

Bilayer (i.e. Cu/InSe and InSe/Cu) as well as triple layer (InSe/Cu/InSe and Cu/InSe/Cu) structures were grown and the total thicknesses of the Cu and InSe layers were kept constant at 200nm and  $2\mu\text{m}$ , respectively. The precursors were deposited onto the glass substrates at a

temperature of 200°C. This temperature was chosen to avoid the condensation of selenium on the substrates.

#### **4.4.2 Selenization Processes**

During the second stage of the process the precursor elements are reacted with each other and with Se species. CuInSe<sub>2</sub> semiconductor thin films are then formed, according to the diffusion process discussed in Section 2.5.3. In this study, three approaches were followed during the final processing of the precursors to form the CuInSe<sub>2</sub> films.

##### **4.4.2.1 Selenization in elemental Se vapour**

In the first approach, the precursors, depicted in Fig. 4.3, were exposed to elemental selenium in vacuum. During the selenization process the substrate temperature was increased from 200°C to 600°C to ensure efficient diffusion of Se into the metal alloys. In order to create and maintain a constant elemental selenium vapour flux, an effusion cell (see Fig. 4.4) was designed. The effusion cell was mounted at an angle of about 45° with respect to the substrates and the distance from the substrate holder to effusion cell was 20 cm. In essence, the effusion cell consists of a stainless steel tube (length = 12 cm and diameter = 2.5 cm) with an evenly spaced heating coil. Selenium of high purity (99.999%) was used and the temperature was accurately monitored by a J-type thermocouple mounted in the bottom part of the effusion cell. The temperature of the effusion cell was controlled with a programmable temperature controller. The top part of the effusion cell was shielded by molybdenum plate in order to create a temperature gradient across the cell. The higher temperature region at the top was required to prevent the condensation of Se at the cell walls during evaporation. The effusion cell was heated up to 330°C in 5 minutes, which resulted in a stable elemental Se flux.

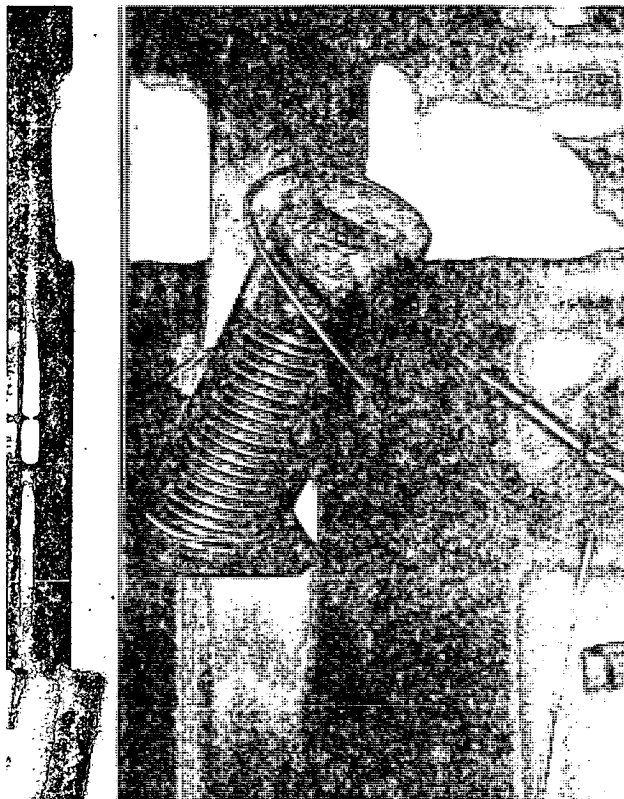


Figure 4.4: Representation of the stainless steel effusion cell which was used to create an uniform elemental selenium flux in vacuum.

A small bolt with a 1mm hole near the top of the effusion cell controlled the elemental Se flux during the selenization processes. This bolt could also be removed in order to full up the effusion cell with Se when required. The amount of Se evaporated was calculated by weighing the effusion cell before and after each selenization processes. For complete reaction of the precursor films, a reaction period of 60 minutes was required, corresponding to about 2 g of Se being evaporated.

#### 4.4.2.2 Selenization in H<sub>2</sub>Se/Ar gas

In a second approach, the metallic precursors were removed from the vacuum and placed in a diffusion furnace. The reaction furnace (Fig. 4.5) was designed and constructed in our laboratories for the controlled selenization of metallic alloys in a mixture of H<sub>2</sub>Se and Ar gases at atmospheric pressure. The operating procedures, developed and optimized over a period of two years, took into account the use of extremely toxic H<sub>2</sub>Se under controlled experimental conditions. The volume concentration of H<sub>2</sub>Se in Ar was carefully controlled by

two separate mass flow controllers. The outlet of the furnace is connected to a cracking furnace and extraction fan and the gaseous atmosphere in the laboratory was constantly monitored with a toxic gas detector. The precursors were placed flat on a graphite substrate holder in a rectangular quartz tube with dimensions of 20cm × 10cm × 50cm. The temperature of the substrates was monitored by a J-type thermocouple and accurate temperature control was guaranteed with a temperature controller. The samples were heated from the bottom by a combination of ten tungsten halogen lamps and this design made it possible to heat samples rapidly to elevated temperatures. Prior to heating, the tube was perched for at least 30 minutes with argon.



Figure 4.5:  $\text{H}_2\text{Se}/\text{Ar}$  reaction furnace used in this study for selenization of metallic precursors.

In this study, the samples were heated to  $450^\circ\text{C}$  in 5 minutes and the volume concentration of  $\text{H}_2\text{Se}$  in Ar was kept constant at 5%. The reaction periods were varied between 45 and 60 minutes. After growth, the samples were cooled down to temperatures below  $200^\circ\text{C}$  within 2 minutes, while maintaining a Se overpressure. The samples were removed from the reaction furnace after at least one hour of flushing with Ar.

#### **4.4.2.3 Rapid thermal processing (RTP)**

As an alternative to  $H_2Se$  and Se reaction, precursors were also processed by rapid thermal annealing. In this case the precursors (Fig.4.3) were covered with an additional  $1\mu m$  thick Se layer. This additional Se was required to compensate for Se losses during rapid thermal annealing. The Se capping layer was deposited by thermal annealing without any intentional substrate heating.

Rapid thermal annealing experiments were carried out in a commercial RTP furnace (AST 100) at the University of Konstanz in Germany. The precursors were encapsulated in a graphite box and heated by tungsten halogen lamps from the top and bottom side. This system enables heating of samples to temperature above  $1000^\circ C$  in only 30 seconds. Prior to heating the reaction chamber was evacuated and flushed several times with nitrogen gas and then filled to a pressure of 0.6 bar with argon.

### **4.5 Device Fabrication**

After  $CuInSe_2$  deposition, the absorber film was covered with a thin CdS buffer layer. The solar cell structure is completed with the deposition of a ZnO window layer and Ni/Al front contacts. A schematic representation of the complete cell structure is given in Fig. 2.1. In this Section, the experimental procedures followed during these final stages of device fabrication, are briefly outlined.

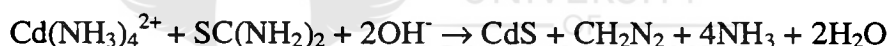
#### **4.5.1 CdS Buffer Layer Deposition**

In this study, 50nm thick CdS buffer layers were deposited on  $CuInSe_2$  by means of a chemical bath deposition (CBD) process. Depositions were carried out in a tube-like reactor ( $100\text{ cm}^3$ ) at temperatures around  $60^\circ C$ . The bath was made up of four separate solutions including cadmium sulfate ( $CdSO_4$ ), thiourea ( $NH_2CSNH_2$ ), ammonia ( $NH_3$ ) and ammonium chloride ( $NH_4Cl$ ). High purity chemicals and deionized water were used and the typical concentrations of the solutions are summarized in Table 4.1. The four solutions were prepared at least 12 hours before being used. The glass reactor was kept in a vertical position in a temperature controlled water bath.

Chemical	Mass/Volume	Volume of H <sub>2</sub> O	Concentration
NH <sub>4</sub> Cl	1.37500g	500ml	0.043M
NH <sub>3</sub>	60ml	342ml	2.0M
CdCl <sub>2</sub>	1.37500g	500ml	15 × 10 <sup>-3</sup> M
NH <sub>2</sub> CSNH <sub>2</sub>	6.08995g	200ml	0.4M

Table 4.1: Experimental details regarding the chemicals and concentration of solutions used in the CBD process.

The process was initiated by adding 20ml of each solution to the reactor. The solutions were always added to the reactor in the same sequence: first CdCl<sub>4</sub>, followed by the thiourea, NH<sub>4</sub>Cl and finally the NH<sub>3</sub>. The samples were subsequently dipped into the heated chemical bath and rotated to ensure homogeneous bath conditions. The samples were removed from the bath after about five minutes and immediately rinsed in deionized water. Deposition of CdS thin films is formed from the reaction between dissolved cadmium ions and thiourea molecules in ammonia solution according to the global reaction:



The growth process is mainly heterogeneous and controlled kinetically by successive surface reactions:

- (1)  $\text{Cd}(\text{NH}_3)_4^{2+} + 2(\text{OH}^-)_{2,\text{ads}} + \text{site} \rightarrow \text{Cd}(\text{OH})_{2,\text{ads}} + 4\text{NH}_3$
- (2)  $\text{SC}(\text{NH}_2)_2 + \text{Cd}(\text{OH})_{2,\text{ads}} \rightarrow \text{C}_{\text{ads}}$
- (3)  $\text{C}_{\text{ads}} \rightarrow \text{CdS} + \text{CN}_2\text{H}_2 + 2\text{H}_2\text{O} + \text{site}$

Where C<sub>ads</sub> represents an adsorbed reaction intermediate. When the precursor concentrations increase, the growth rate increases and a growth by colloid aggregation becomes possible. In the case of cadmium it is related to the formation of cadmium hydroxide clusters in the solution, which catalyse the formation of CdS particles in the bath.



#### 4.5.2 ZnO Window Layer Deposition

In this study, the ZnO films were deposited by DC magnetron sputtering. A schematic representation of the specific system used in this study is given in Fig.4.6. The system was equipped with a circular planar magnetron, which has a 55mm diameter erosion zone and is cooled by forced air circulation.

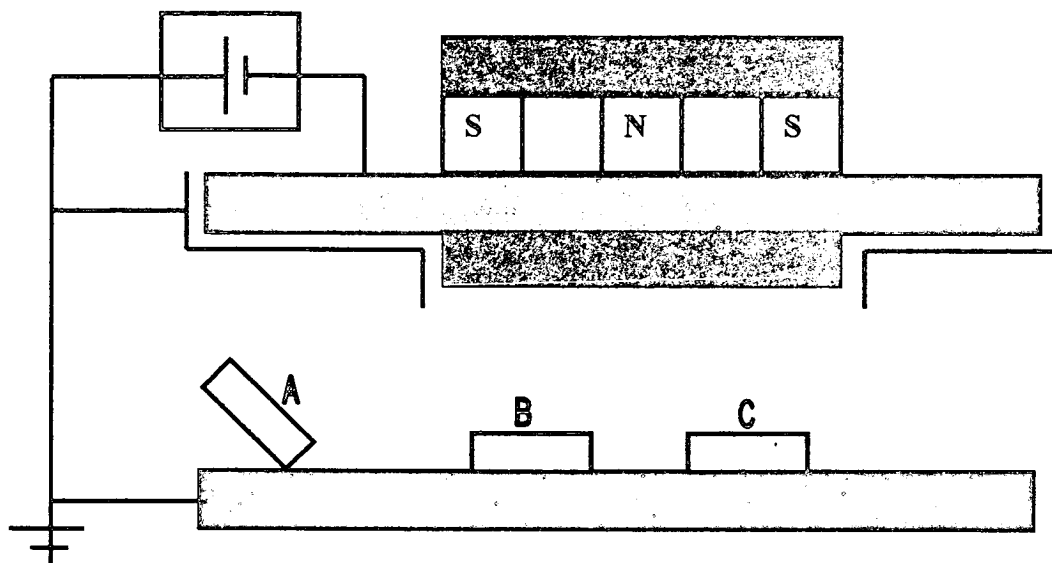


Figure 4.6: Basic configuration of the DC magnetron sputtering unit used in this study for ZnO sputtering.

The target for intrinsic depositions was a 100mm diameter 99.999% ZnO ceramic disc. For the doped depositions, a 2.5% Al<sub>2</sub>O<sub>3</sub>-doped ZnO target was used. The pure ZnO and Al-doped ZnO targets were prepared by pressing 200g of ZnO and 200g of ZnO plus 5g of Al<sub>2</sub>O<sub>3</sub> powder respectively, followed by sintering at 920°C for an hour, then cooled down overnight. After that the targets were machined to a smooth disc and sintered again for two hours at 1200°C. In the sputtering system, the target discs were bonded to a cooled backing plate. After pumping the system down (about 10<sup>-5</sup> mbar) the substrates were heated with halogen lamps to the desired temperature around 100°C. The sputtering gas (99.999% Ar) was admitted to the chamber through a calibrated leak valve. The working gas pressure was maintained around 7x10<sup>-3</sup> mbar. The DC power was kept constant around 40.8W. The substrates (A, B and C in Fig. 4.6) were placed at different positions and orientations in the sputter unit. A summary of the sputtering conditions is given in the Table 4.2.

<i>Control Parameters</i>	<i>ZnO (Undoped)</i>	<i>ZnO (Doped)</i>
Base pressure (mbar)	$8 \times 10^{-5}$	$8 \times 10^{-5}$
Sputtering pressure (mbar)	$7 \times 10^{-3}$	$7 \times 10^{-3}$
Sputtering current (mA)	120	120
Sputtering voltage (V)	340-350	340-350
DC power (W)	40.8	40.8-42.0
Deposition ratio ( $\text{\AA}/\text{s}$ )	1.3-3.5	1.3-3.5

Table 4.2: Summary of experimental parameters used during sputtering of ZnO.

### 4.5.3 Ni/Al front contact deposition

Electron-beam evaporation was used to deposit 50nm of Ni and 1 $\mu\text{m}$  Al through a metal mask onto the ZnO window layers. The mask was design to cover only 5% of the total active cell area. Evaporations were carried out at about  $10^{-6}$  mbar at a rate of  $2\text{nm sec}^{-1}$ . The Ni/Al grids were deposited without any intentional heating and the layer thicknesses were monitored by an oscillating quartz crystal monitor. A rotatable four-pocket crucible permitted the sequential deposition of Ni and Al without breaking vacuum. Cell areas were delineated by mechanical scribing to produce individual cells with  $0.5\text{ cm}^2$  areas.

## 4.6 Characterization Techniques

### 4.6.1 Introduction

In this study, a wide variety of characterization techniques were used to evaluate the material quality of the semiconductor thin films. The structural properties of the polycrystalline films were studied by scanning electron microscopy (SEM) and the presence of crystalline phases by X-ray diffraction (XRD). The stoichiometric ratio and  $\text{CuInSe}_2$  layer thicknesses were determined by energy dispersive X-ray spectroscopy (EDS) and X-ray fluorescence (XRF). The optical properties of the films were evaluated by infrared spectroscopy and low temperature photoluminescence (PL) studies. The electrical properties of the materials were investigated by standard four-point probe and Hall measurements. Completed devices were evaluated in the dark and under illumination by standard I-V characterization equipment. The

most important features of these characterisation techniques are outlined in the following Sections.

## **4.6.2 Structural Analysis**

### **4.6.2.1 Introduction**

Several levels of structural information were of interest in this particular study. The first level broadly deals with the issues of film surface topography and morphology including grain size and shape, evidence of film voids and the lack of adhesion between the glass substrates and the thin films. Somewhat more difficult to obtain, but crucial to successful device fabrication, is information about the compositional uniformity of the films as function of depth. Lastly, are the X-ray diffraction patterns and the information they convey regarding the presence of secondary phases in the compound the films.

### **4.6.2.2 Scanning Electron Microscopy (SEM)**

In this study the morphological features of the various thin films were investigated with a JEOL JSM-840 SEM, equipped with a LINK AN10000 EDS detector. The SEM is perhaps the most widely employed thin-film and coating characterization instrument. A schematic representation of a typical SEM is shown in Fig. 4.7. Electrons thermionically emitted from a tungsten or LaB<sub>6</sub> cathode filament are drawn to an anode, focused by two successive condenser lenses into a beam with a very fine spot size (~50 Å).

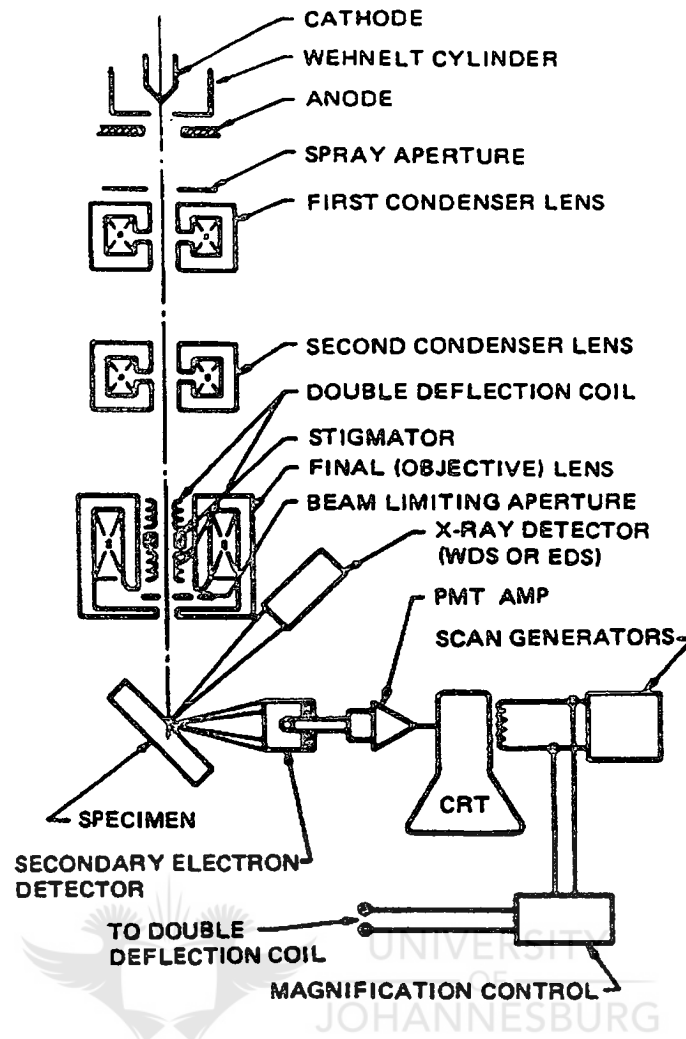


Figure 4.7: Schematic of the scanning electron microscope (Goldstein et al., 1981).

Pairs of scanning coils located at the objective lens deflect the beam either linearly or in raster fashion over a rectangular area of the specimen surface. Electron beams having energies ranging from a few thousand to 50keV, with 30keV a common value, are utilized. Upon impinging on the specimen, the primary electrons decelerate and in losing energy transfer it inelastically to other atomic electrons and to the lattice. Through continuous random scattering events, the primary beam effectively spreads and fills a teardrop-shaped interaction volume (Fig. 4.8 (a)) with a multitude of electronic excitations. The result is a distribution of electrons that manage to leave the specimen with an energy spectrum shown schematically in Fig. 4.8 (b). In addition, target X-rays are emitted, and other signals such as light, heat, and specimen current are produced, and the sources of their origin can be imaged with appropriate detectors. The various SEM techniques are differentiated on the basis of what is subsequently detected and imaged.

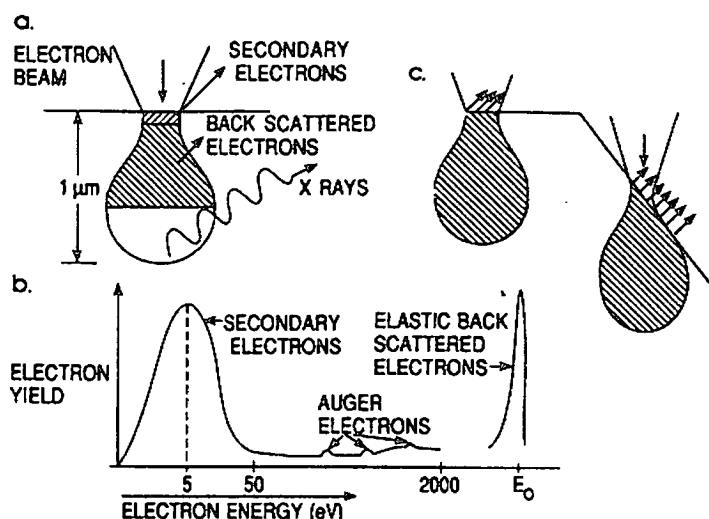


Figure 4.8: (a) Electron and photon signals emanating from a tear-shaped interaction volume during electron-beam impingement on a specimen surface. (b) Energy spectrum of electrons emitted from specimen surface. (c) Effect of surface topography on electron emission (Ohring, 1992).

### Secondary Electrons

The most common imaging mode relies on detection of this very lowest portion of the emitted energy distribution. Their very low energy means they originate from a subsurface depth of no larger than several angstroms. The signal is captured by a detector consisting of a scintillator-photomultiplier combination, and the output serves to modulate the intensity of a CRT, which is rastered in synchronism with the raster-scanned primary beam. The image magnification is then simply the ratio of scan lengths on the CRT to that on the specimen. Resolution specifications quoted on research quality SEM's are  $\sim 50\text{\AA}$ . Great depth of focus enables images of beautiful three-dimensional quality to be obtained from non-planar surfaces. The contrast variation observed can be understood with reference to Fig. 4.8 (c). Sloping surfaces produce a greater secondary electron yield because the portion of the interaction volume projected on the emission region is larger than on a flat surface. Similarly, edges will appear even brighter.

### Backscattered Electrons

Backscattered electrons are the high-energy electrons that are elastically scattered and essentially possess the same energy as the incident electrons. The probability of backscattering increases with the atomic number  $Z$  of the sample material. Since the

backscattered fraction is not a very strong function of  $Z$  (varying very roughly as  $\sim 0.05 Z^{1/2}$  for primary electron beams employed in the SEM), elemental identification is not feasible from such information. Nevertheless, useful contrast can develop between regions of the specimen that differ widely in  $Z$ . Since the escape depth for high-energy backscattered electrons is much greater than for low-energy secondaries, there is much less topological contrast in the images.

#### 4.6.2.3 Energy Dispersive X-Ray Spectroscopy (EDS) and X-Ray Fluorescence (XRF)

The stoichiometry of multinary compound semiconductor has a strong influence on their material properties. The exact control of the stoichiometry and accurate analysis of the composition of these thin films are therefore a prerequisite for preparation of high quality thin film chalcopyrite absorbers. By far the most common used technique for the chemical analysis of thin films is electron probe micro-analysis (EPMA), sometimes also called energy dispersive X-ray spectroscopy (EDX or EDS). This method is fast, non-destructive and a very high lateral resolution can be obtained. Most EDS systems are interfaced to SEM's, where the electron beam serves to excite characteristic X-rays from the area of the specimen being probe. There are two common methods to record the spectra of the emitted characteristic radiation. The first is to measure the whole energy spectrum simultaneously with an energy sensitive detector. The second option is to use a goniometer and an analyzing crystal with  $\theta$ - $2\theta$  coupling and to assign a measured intensity to a  $2\theta$  position. By means of the Bragg equation  $n\lambda = 2d \sin \theta$ , the energy of a measured peak can then be determined from the  $2\theta$ -position of the detector. The first technique, the energy dispersive spectrometry, is known as EDS or EDX, while the second approach is called wavelength dispersive spectrometry (WDS or WDX). These techniques, however, lack reproducibility and accuracy in the case of samples with identical stoichiometry, but with different structural properties (i.e. film thickness, grain size and surface roughness). In order to understand the effects responsible for shortcomings in thin film analysis with EPMA, it is important to consider the excitation process. In the case of EPMA, the characteristic radiation is excited by an incident electron beam. The electrons are decelerated in the sample material and, besides other effects, inner electron shells of target atoms become ionized. That in turn causes the emission of the characteristic radiation. One electron can cause several ionization events and it will be strongly deflected or even backscattered while being slowed down in the sample. The distribution of the primary X-ray generation depends mainly on the electron-beam

acceleration voltage, the material density, the scattering of primary electrons and the variation of the ionization cross-section with the electron energy. For thin film chalcopyrite solar cells and typical acceleration voltages, the excited volume is of the same order of magnitude as the thickness of the absorber layer. The higher the electron density, the higher the excited radiation density. Therefore the radiation generation is not homogeneous and will be less effective in the outer region of the excited volume. The EPMA measurement result is also influenced by fluctuations of the detected intensities. The chalcopyrite thin films have a relatively rough surface, and the average film thickness varies over the whole sample area to a certain extent. If one projects an imaginary excitement volume to different spots there will be differences in the penetration depth relative to the film thickness and the amount of the analyzed material. At a short range of the analyzed sample area because of the roughness, at a larger range also because of the average thickness variation. Even if the material composition would be absolutely homogeneous, this would already cause slight fluctuations in the output. The relative intensities compared to each other are dependent on the excitation depth distribution, because of the different influence of the matrix effects for every characteristic line. This will be especially important if not only copper, gallium and selenium with their similar weight and X-ray absorption properties are measured but, for example, also indium and sulfur. An appreciably larger error is caused if there is a depth gradient in the elemental distribution, because the output is in that case more dependent on the penetration depth to film thickness ratio, especially because the EPMA can mostly use only the  $L\alpha$ -lines for the chalcopyrite elements. The error will increase once again if for some of the elements the  $L\alpha$ -lines and for others the  $K\alpha$ -lines are used. Besides these effects the EPMA is sensitive to the angle of incidence of the electron beam which on a rough surface can be different on this scale when measured at various spots. It is difficult to give a quantitative estimation of the error caused by these effects, because the error is strongly dependent on the sample properties and measurement conditions, but it can be of the magnitude of several atomic percent. Besides these effects, which cause fluctuations in the output, there is a problem with the calibration standards, which can lead to systematic errors. Normally the used standards are pure elements, either in the form of a "bulk" or as a thin film. Another possibility is to use similar thin films with a known composition. The use of pure element standards is doubtful, because the surface properties of the standards will be different from those of the unknown samples, for example, because of oxidation or the preparation conditions. The use of similar

film standards will be a better choice, but will only lead to correct results as long as the unknown samples have a similar thickness, grain size and homogeneity as the used standards.

A remarkable improvement in reproducibility can be achieved by the use of X-ray fluorescence (XRF), a technique which is quite similar to EPMA. In the case of XRF, however, the characteristic X-rays are generated by an incident X-ray beam. Usually the polychromatic radiation from a X-ray tube is the excitation source of the XRF. The primary beam of the X-ray source penetrates the sample atoms. When electrons from outer shells fill the resulting gaps, the characteristic radiation is emitted. In most cases  $K\alpha_{1,2}$  or  $L\alpha_1$ -lines are used for chemical analysis, because they are generally the most intense lines on the spectra. The  $K\alpha_{1,2}$ -lines provide information about the total amount of each of the elements and thicknesses of films, while the  $L\alpha_1$ -lines are more surface sensitive. It has recently been indicated (Klenk et al., 1999) that the large penetration depth of X-rays leads to proportional relations between the  $K\alpha_{1,2}$ -lines intensities and the mass per analysed area of the sample. As the information depth (approximately  $100\mu\text{m}$ ) is much larger than a typical thin film layer thickness ( $1\text{-}2\mu\text{m}$ ), not only the absorber material but also other layers of a thin film cell can be analyzed. In the case of a typical chalcopyrite solar cell this means, for example, that the thickness of the very thin CdS layer can be determined as well as that of the molybdenum and ZnO layers. Due to the high  $2\theta$  resolution of XRF, there is also no line overlap of the different elements present in the chalcopyrite absorber material, which could disturb the measurement. There is also no line overlap caused by other commonly used solar cell materials such as Mo, ZnO or CdS. The large penetration depth of X-rays also minimizes the matrix effects and allows for a relatively easy calibration process. Besides the concentration in atomic percent, the total amount of each of the elements in the layer as well as the film thickness can be measured accurately.

#### 4.6.2.4 X-Ray Diffraction (XRD)

X-ray diffraction is a very important experimental technique that has long been used to address all issues related to the crystal structure of bulk solids, including lattice constants and geometry, identification of unknown materials, orientation of single crystals, and preferred orientation of polycrystals, defects, stresses, etc. In this study a SIEMENS D5000 X-ray system was used to analyse the various thin films produced in this study. X-ray scans were performed between  $2\theta$  values of  $10^\circ$  and  $90^\circ$  with a typical step size of  $0.02^\circ$ , using Cu  $K\alpha$



radiation. CuInSe<sub>2</sub>, for example, crystallizes in the well-known tetragonal lattice with plane spacings given by:

$$\frac{1}{d^2} = \frac{h^2 + k^2}{a^2} + \frac{l^2}{c^2} \quad (4.1)$$

By combining equation (4.1) with the Bragg law:

$$n\lambda = 2d \sin \theta \quad (4.2)$$

We have:

$$\sin^2 \theta = \frac{\lambda^2}{4} \left( \frac{h^2 + k^2}{a^2} + \frac{l^2}{c^2} \right) \quad (4.3)$$

where  $\lambda=1.540562\text{\AA}$  for Cu K $\alpha$ 1 radiation.

The crystalline phases were identified by matching the XRD peak with those given in the Joint Council for Powder Diffraction Studies (JCPDS) files.

### 4.6.3 Optical Characterization

#### 4.6.3.1 Introduction

An important aspect of this study was the optical characterization of the semiconductor thin films produced in this study. Standard transmission measurements were used to determine the thicknesses of layers, absorption coefficients, index of refraction and optical band gaps of films. In addition, low temperature photoluminescence was employed to investigate the presence of intrinsic defect levels in the CuInSe<sub>2</sub> absorber films. In this Section, we discuss the most important features of these characterization techniques.

#### 4.6.3.2 Infrared Spectroscopy

The optical properties of the films were determined by analysis of transmission spectra, obtained by using a Varian Cary 500 Spectrophotometer. There are two basic instrumentation approaches to measure the transmission spectra. The older, more traditional one is based on the use of a monochromator; the more recent and new more popular one is based on an interferometer. The foundation of modern Fourier transform infrared spectroscopy (FTIR)

were laid in the latter part of the nineteenth century by Michelson (Michelson, 1891). The basic optical component of Fourier transform spectrometers is the Michelson interferometer shown in simplified form in Fig. 4.9.

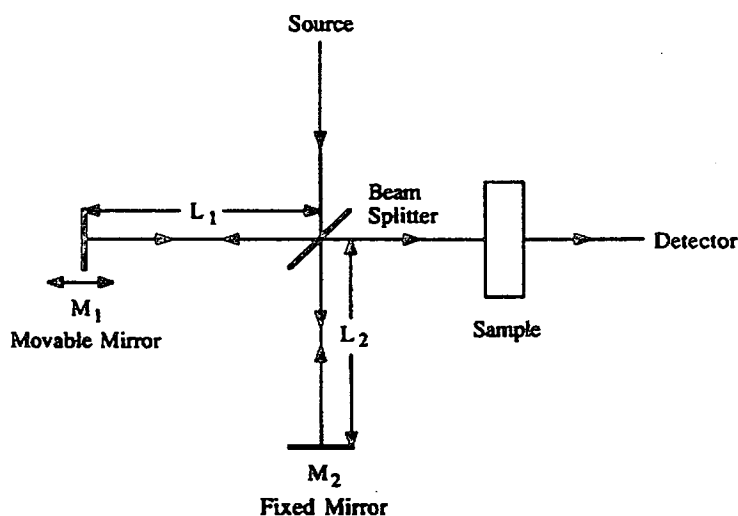


Figure 4.9: Schematic representation of a Fourier transform infrared spectrometer (Schroder, 1990).

Light from an infrared source is collimated and incident on a beam splitter. An ideal beam splitter creates two separate optical paths by reflecting 50% of the incident light and transmitting the remaining 50%. In the near and middle infrared region, germanium deposited on a KBr substrate is commonly used as beam splitter. In one path the beam is reflected by a fixed-position mirror back to the beam splitter where it is partially reflected to the source and partially transmitted to the detector. In the other leg of the interferometer, the beam is reflected by the movable mirror that is translated back and forth and maintained parallel to itself. The beam from the movable mirror is also returned to the beam splitter where it too is partially transmitted back to the source and partially reflected to the detector. Although the light from the source is incoherent, when it is split into two components by the beam splitter, the components are coherent and can produce interference phenomena when the beams are combined. The detector is typically a deuterated triglycine sulfate pyroelectric detector, and the movable mirror rides on an air bearing for good stability. Other detectors such as cooled HgCdTe are also used. The light intensity reaching the detector is the sum of the two beams. The two beams are in phase and reinforce each other when  $L_1=L_2$ . When  $M_1$  is moved, the optical path lengths are unequal, and an optical path difference  $\delta$  is introduced. If  $M_1$  is moved a distance  $x$ , the retardation is  $\delta=2x$  since the light has to travel an additional distance  $x$

to reach the mirror and the same additional distance to reach the beam splitter. Consider the output signal from the detector when the source emits a single frequency or wavelength. For  $L_1=L_2$  the two beams reinforce each other because they are in phase,  $\delta=0$ , and the detector output is a maximum. If  $M_1$  is moved by  $x=\lambda/4$ , the retardation becomes  $\delta=2x=\lambda/2$ . The two wave fronts reach the detector  $180^\circ$  out of phase, resulting in destructive interference or zero output. For an additional  $\lambda/4$  movement by  $M_1$ ,  $\delta=\lambda$  and constructive interference results again. The detector output-the interferogram-consists of a series of maxima and minima that can be described by the equation (Schroder, 1990)

$$I(x) = B(f)[1 + \cos(2\pi x f)] \quad (4.4)$$

where  $B(f)$  is the source intensity.

#### 4.6.3.3 Photoluminescence

In this study, steady state PL measurements were carried out using a 40mW Krypton-Ion-Laser (Spectra Physics Model 165 Ion Laser) at an excitation wavelength of 568.2 nm. The luminescence light was analyzed and detected by a GCA/McPherson Instrument 1 meter Scanning Monochromator and liquid nitrogen cooled germanium detector (North Coast EO-817L). Photoluminescence (PL) provides a non-destructive technique for the determination of certain impurities in semiconductors (Bedd and Williams, 1972). It is particularly suited for detection of shallow-level impurities but can also be applied to certain deep-level impurities, provided that radiative recombination events dominate non-radiative recombination (Dean, 1982). Identification of impurities is easy with PL, but measurement of the concentration of impurities is more difficult. PL can provide simultaneous information on many types of impurities in a sample. However, only those impurities that produce radiative recombination processes can be detected. Fortunately many impurities fall within this category. A typical PL set-up is illustrated in Fig. 4.10. The sample is placed in a cryostat and cooled to temperatures near liquid helium. Low-temperature measurements are necessary to obtain the fullest spectroscopic information by minimising thermally-activated non-radiative recombination processes and thermal line broadening.

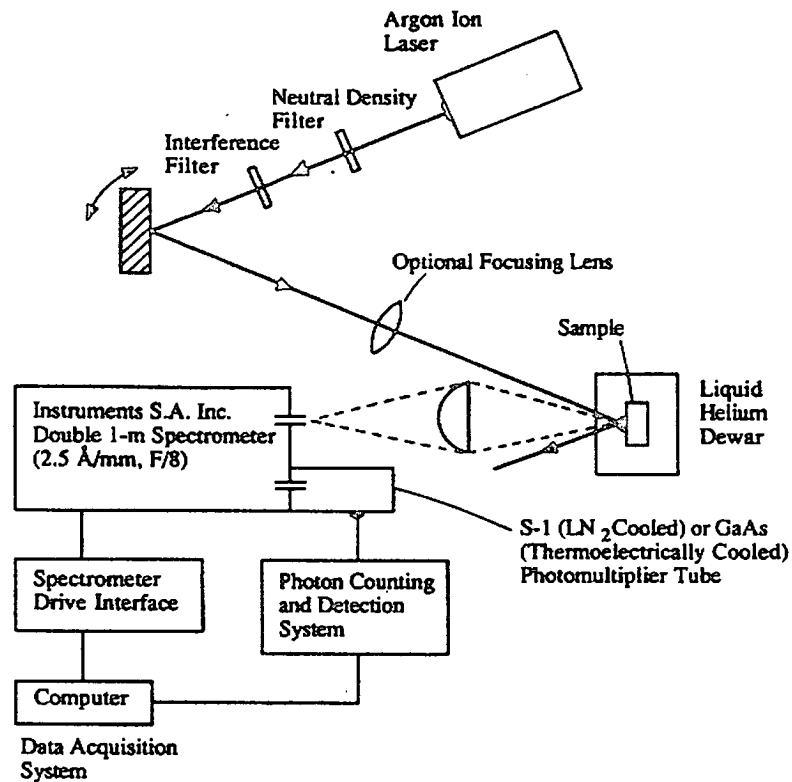


Figure 4.10: Typical apparatus for photoluminescence measurements (Stillman et al., 1988).

The thermal distribution of carriers excited into a band contributes a width of approximately  $kT/2$  to an emission line originating from that band. This makes it necessary to cool the sample to reduce the width. The thermal energy  $kT/2$  is only 1.8meV at  $T= 4.2\text{K}$ . For many measurements this is sufficiently low, but occasionally it is necessary to reduce this broadening further by reducing the sample temperature below 4.2K. The sample is excited with an optical source, typically a laser with  $h\nu > E_g$ , generating electron-hole pairs (ehp's) that recombine by one of several mechanisms. Photons are emitted for radiative recombination. For non-radiative processes photons are not emitted. For good PL output one would like the majority of the recombination processes to be radiative. The photon energy depends on the recombination process illustrated in Fig. 4.11, where five of the most commonly observed PL transitions are shown (Smith, 1981). Band-to-band recombination (Fig. 4.11 (a)) dominates at room temperature but is rarely observed at low temperatures in materials with small effective masses due to the large electron orbital radii. Excitonic recombination is commonly observed, but what are excitons? When a photon generates an ehp, Coulombic attraction can lead to the formation of an excited state in which an electron and a hole remain bound to each other in a hydrogen like state (Wolfe and Mysyrowicz,

1984). This excited state is referred to as a free exciton (FE). Its energy, shown in Fig. 4.11 (b), is slightly less than the band gap energy required to create a separated ehp.

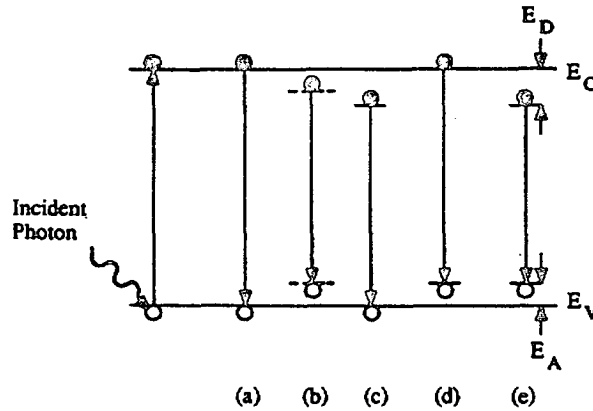


Figure 4.11: Radiative transitions observed with photoluminescence (Schroder, 1990).

An exciton can move through the crystal, but being a bound ehp, both electron and hole move together and no photoconductivity results, for example. A free hole can combine with a neutral donor (Fig. 4.11 (c)) to form a positively charged excitonic ion or bound exciton (BE) (Pankove, 1975). Similarly electrons combining with neutral acceptors also form bound excitons. If the material is sufficiently pure, free excitons form and recombine by emitting photons. The photon energy in direct band gap semiconductors is (Pankove, 1975):

$$h\nu = E_g - E_x \quad (4.5)$$

where  $E_x$  is the excitonic energy. In indirect band gap semiconductors, momentum conservation requires the emission of a phonon, giving (Pankove, 1975)

$$h\nu = E_g - E_x - E_p \quad (4.6)$$

where  $E_p$  is the phonon energy. Bound exciton recombination dominates over free exciton recombination for less pure material. A free electron can recombine with a hole on a neutral acceptor (Fig.4.11 (d)), and similarly a free hole can recombine with an electron on a neutral donor (Fig. 4.11 (c)). Lastly, an electron on a neutral donor can recombine with a hole on a neutral acceptor, the well-known donor-acceptor (D-A) recombination, illustrated in Fig. 4.11 (e). The emission line has an energy modified by the Coulombic interaction between donors and acceptors (Dean, 1982):

$$h\nu = E_g - (E_A + E_D) + \frac{q^2}{K_s \epsilon_0 r} \quad (4.7)$$

where  $r$  is the distance between donor and acceptor. The photon energy in Eq. (4.7) can be larger than the band gap for small  $E_A + E_D$ . Such photons are generally re-absorbed in the sample. The full width at half maximum (FWHM) for bound exciton transitions are typically  $\leq kT/2$  and resemble slightly broadened delta functions. This distinguishes them from donor valence band transitions which are usually a few  $kT$  wide.

#### 4.6.4 Electrical Characterization

##### 4.6.4.1 Introduction

As in the case of structural and optical characterization, it is crucial to investigate the electrical properties of semiconductor materials in order to optimize the growth conditions. In this study, the transport properties in our polycrystalline thin films were evaluated by standard four-point probe and Hall effect measurement. The relevant theoretical aspects of these techniques are summarized in this Section.

##### 4.6.4.2 Four-Point Probe

The four-point probe technique is one of the most common methods for measuring the semiconductor resistivity. If an electric field  $E$  is applied to a semiconductor material, an electric current will flow, whose density  $J$  is given by:

$$J = \sigma E \quad (4.8)$$

where  $\sigma$  is called the electrical conductivity of the material. The reciprocal of electrical conductivity is known as electrical resistivity  $\rho$ . For a rectangular-shaped sample (Fig. 4.12 (a)), the resistance  $R$  is given by

$$R = \rho(l/bt) \quad (4.9)$$

where  $l$  is the length,  $b$  is the width and  $t$  is the thickness of the sample. If  $l=b$ , equation (4.9) becomes:

$$R = \rho/t = R_s$$

The quantity  $R_s$  is known as the sheet resistance and it is the resistance of one square of the film and is independent of the size of the square. The sheet resistance is expressed in Ohms/square. The most commonly used method for measuring the sheet resistance  $R_s$  is a four-point probe technique. A typical schematic set-up is shown in Fig. 4.12(b).

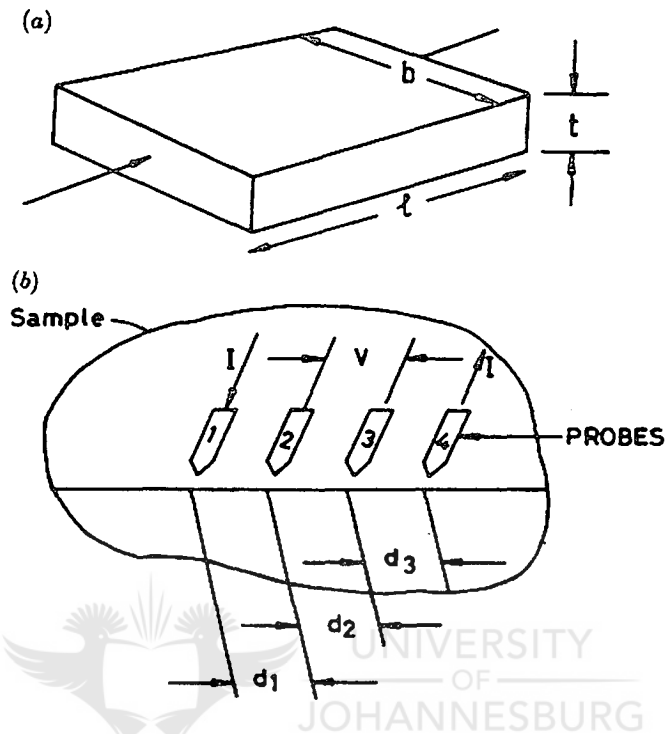


Figure 4.12: (a) Definition of resistivity and sheet resistance and (b) Four-point probe technique (Hartnagel et al., 1995).

When the probes are placed on a material of semi-infinite volume, the resistivity is given by (Valdes, 1954):

$$\rho = \frac{V}{I} \frac{2\pi}{1/d_1 + 1/d_2 - 1/(d_1 + d_2) - 1/(d_2 + d_3)}$$

when  $d_1 = d_2 = d_3 = d$ ,

$$\rho = \frac{V}{I} 2\pi d \quad (4.10)$$

If the material is in the form of an infinitely thin film resting on an insulating support, equation (4.10) leads (Valdes, 1954) to:

$$\rho = \frac{V}{I} \frac{\pi}{\ln 2}$$

or

$$\frac{\rho}{t} = R_s = 4.53 \frac{V}{I}$$

#### 4.6.4.3 Hall Effect Measurements

A Hall effect study is usually required to distinguish between the two types of carriers. It also allows determination of the density of the charge carriers. When a current is passed through a slab of material in the presence of a transverse magnetic field (Fig. 4.13), a small potential difference, known as the Hall voltage, is developed (between face 1 and face 2), in a direction perpendicular to both the current and the magnetic field. Face 1 is positive for  $p$ -type samples, whereas it is negative for  $n$ -type samples. Mathematically, it is given by

$$V_H = R_H I (B/t) \quad (4.11)$$

where  $V_H$  is the Hall voltage,  $B$  is the magnetic field and  $I$  is the current through the sample.  $R_H$  is the Hall coefficient and is related to the carrier density according to the relation

$$R_H = r_H (1/Ne) \quad (4.12)$$

where  $r_H$  is the Hall scattering factor. The value of  $r_H$  depends on the geometry of the scattering surface and the mechanisms by which the carriers are scattered.

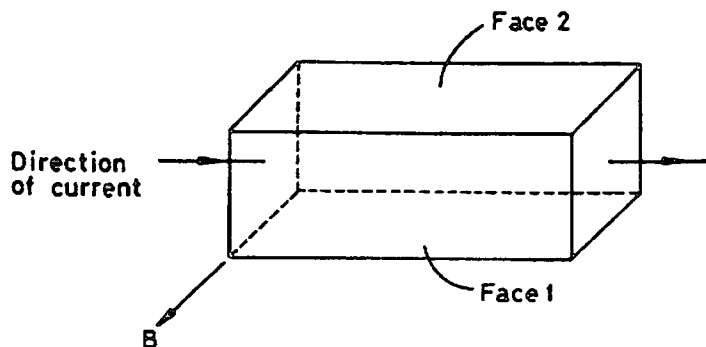


Figure 4.13: The Hall effect phenomenon (Hartnagel et al., 1995).



In general,  $r_H$  does not depart very significantly from unity. For  $n$ -type semiconductors,  $R_H$  is negative, while for  $p$ -type it is positive. Hall effect measurements, in conjunction with the measurement of conductivity, enable calculation of the mobility of charge carriers:

$$\mu = \sigma / Ne \quad (4.13)$$

where  $\mu$  is the mobility of charge carriers.

Combination of equations (4.12) and (4.13) leads to:

$$\mu = R_H \sigma . \quad (4.14)$$

The value of mobility of charge carriers determined by Hall measurements is known as Hall mobility ( $\mu_H$ ).

#### 4.6.5 Device Characterization

In this study, completed devices were evaluated under AM 1.5 ( $100 \text{ mW cm}^{-2}$ ) conditions, using a Oriel Solar Simulator. The radiation distribution of AM 1.5 radiation is depicted in Fig. 3.3. A typical experimental arrangement for measuring solar cell output characteristics is shown in Fig. 4.14.

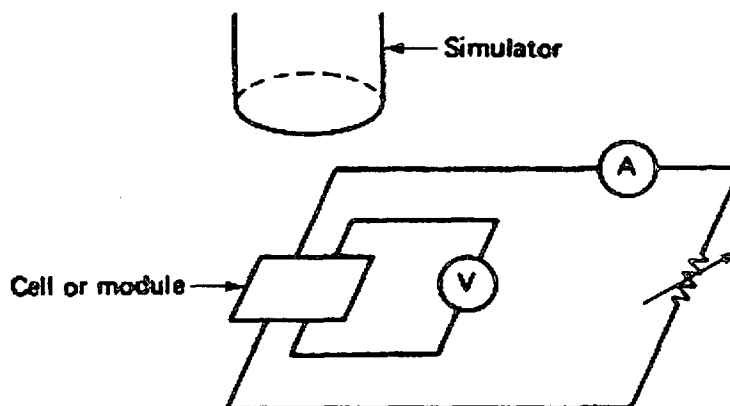


Figure 4.14: Experimental configuration for testing solar cells and modules (Green, 1992).

A four-point contacting scheme is desirable in which voltage and current leads to the cell under test are kept separate. This eliminates effects due to the series resistance of the test leads and associated contact resistances. The cells are mounted on a temperature-controlled block. Both 25°C and 28°C are standard temperatures for solar cell measurements. The lamp intensity is adjusted to give the desired intensity as measured by a reference cell. By varying the load resistance, the characteristics of the test cell can then be measured.



## References

- H. B. Bedd and E. W. Williams (1972) Academic Press, New York **8**, p181-320.
- P. J. Dean (1982) Prog. Crystal Growth Charact. **5**, p 89-174.
- J. I. Goldstein, D. E. Newbury, P. Echlin, D. C. Joy, C. Fiori, and E. Lifshin (1981) Scanning Electron Microscopy and X-Ray Microanalysis, Plenum, New York.
- H. L. Hartnagel, A. L. Dawar, A. K. Jain and C. Jagadish (1995) Semiconducting Transparent Thin Films.
- M. Klenk, O. Schenker, U. Probst and E. Bucher (1999) Solar Energy Materials & Solar Cells **58**, p 299-319.
- A. A. Michelson (1891) Phil Mag. **31**, p 256-259.
- M. Ohring (1992) The Materials Science of Thin Films, Academic Press, New York.
- J. I. Pankove (1975) Optical Processes in Semiconductors, Dover, New York.
- D. K. Schroder (1990) Semiconductor Material and Device Characterization, Wiley Interscience, New York.
- K. K. Smith (1981) Thin Solid Films **84**, p 171-182.
- G. E. Stillman, B. Lee, M. H. Kim and S. S. Bose (1988) Electrochem. Soc., Pennington, NJ, p 56-70.
- L. B. Valdes (1954) Proc. IRE **42**, p 420.
- J. P. Wolfe and A. Mysyrowicz (1984) Sci. Am. **250**, p 98-107.

## CHAPTER 5

### RESULTS AND DISCUSSION

#### 5.1 Introduction

As pointed out in Section 2.3, I-III-VI<sub>2</sub> compound semiconductors are important photovoltaic materials with diverse material properties that can be tuned for optimum device performance. Important progress has been made, especially in terms of small cell efficiencies, with the performance of the best thin film laboratory cells approaching the performance of multi-crystalline silicon cells. Despite this progress on a fundamental level, there is as yet no commercial scale manufacturing facility operating today. The current position is mainly attributed to the absence of a scalable, relatively simple approach for the preparation of high quality CuInSe<sub>2</sub> absorber films. In addition, the development of efficient, low-priced thin film solar cells has been hampered by the lack of basic material research on the crucial absorber material. Against this background, the aim of the present study was two-fold: the investigation of the fundamental material properties of CuInSe<sub>2</sub> thin film absorbers and the development of processing technologies which can easily be scaled-up in order to be useful to industry. In addition to these important aims, a standard CdS/ZnO window layer technology was developed during this study. Preliminary solar cell devices were also fabricated and evaluated. The most important results that followed from these studies will be discussed in this Chapter.

#### 5.2 Material Properties of CuInSe<sub>2</sub>

##### 5.2.1 Introduction

A promising growth technique, developed about five years ago, involved the selenization of copper-indium alloys in elemental Se vapour or a reactive H<sub>2</sub>Se/Ar atmosphere. However, progress (reproducibility and scale-up) has been seriously hampered by adhesion problems between the Mo back contact and chalcopyrite absorber film. In addition, losses of material during the selenization process and the complex interdiffusion of intermediate phases (e.g. In<sub>2</sub>Se<sub>3</sub>, Cu<sub>2-x</sub>Se and CuSe) critically influenced the controllability of the film quality. In this study, device quality CuInSe<sub>2</sub> absorber films were produced by a relatively simple, tolerant and reproducible two-stage growth technique. This process involved the preparation of

various selenium containing precursor layers by thermal evaporation, and the subsequent reaction of these precursors to produce the compound semiconductor absorber films.

In this Section, the material properties (structural, optical and electrical) of the CuInSe<sub>2</sub> absorber films are discussed in detail. Attention is mainly given to the structural properties of the precursor films prior to selenization and the influence of the various processing techniques (i.e. in elemental Se vapour, in H<sub>2</sub>Se/Ar and rapid thermal processing) on the final quality of the absorber films. From these studies growth parameters were determined to produce CuInSe<sub>2</sub> absorber films with optimum material properties (i.e. uniform and dense films with a high degree of compositional uniformity) for solar cell applications.

### 5.2.2 Structural Properties of Precursor Films

The optimization of the structural properties of the CuInSe<sub>2</sub> absorber films is an important prerequisite for the successful fabrication of high efficiency CuInSe<sub>2</sub>/CdS/ZnO solar cell devices. In this study the attention was mainly focussed on the optimization of two distinct processing steps; i.e. precursor formation and the subsequent reaction process. In the former case, it is believed that the precursor structure is determinant to the morphology and adhesion of the final CuInSe<sub>2</sub> film. It is, for example, anticipated that the thickness uniformity, the degree of alloying between the respective layers in the stack and the morphology of the resulting precursor alloy are all factors that determine the final material quality of the absorber films. A series of samples (Fig. 4.3) were prepared in this study in order to optimize the precursor deposition parameters. Figs. 5.1 (a) and (b) show planar view SEM micrographs of the surface morphologies of typical Mo/InSe/Cu/InSe and Mo/Cu/InSe/Cu precursor structures. The precursors shown in these micrographs were deposited on Mo films, prepared under identical and optimized conditions (Section 4.3). It is therefore reasonable to assume that the underlying Mo layer had very little influence on the morphology of the final alloys, shown in Fig. 5.1. In addition, for each of these metal films there were only minor differences in the morphologies when the layer thicknesses of Cu and InSe were varied. A comparison of Figs. 5.1 (a) and (b) clearly reveals a significant difference in morphological features when the order of deposition was varied. In the case of bilayers (Mo/Cu/InSe) and triple layers (Mo/InSe/Cu/InSe) in which the growth sequence was terminated with a InSe layer, films were visually extremely smooth and uniform. SEM studies (Fig. 5.1 (a)) indicated that these specific films were flat and smooth with virtually no evidence of grain formation.

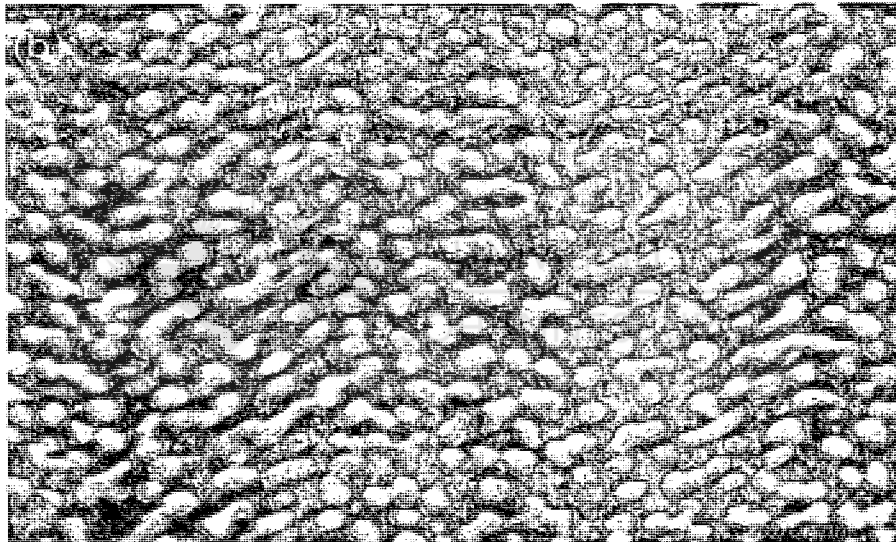
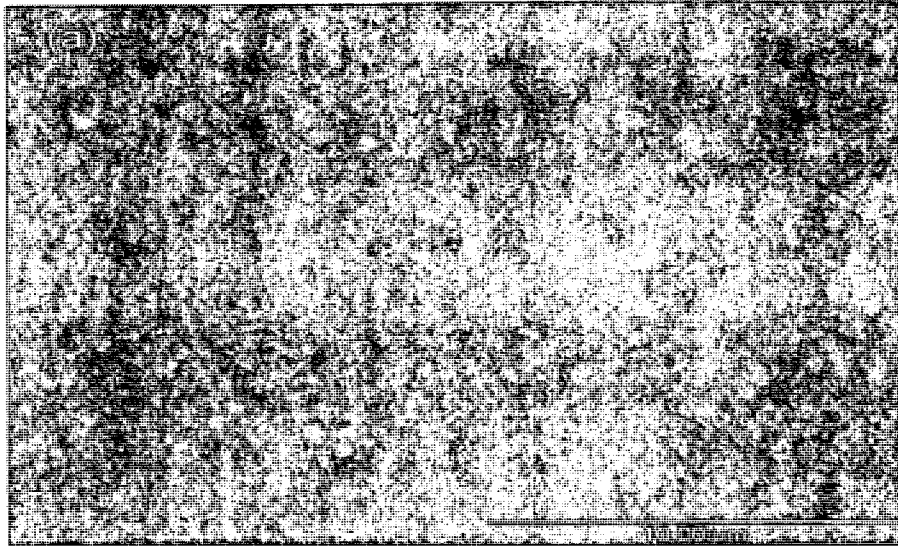
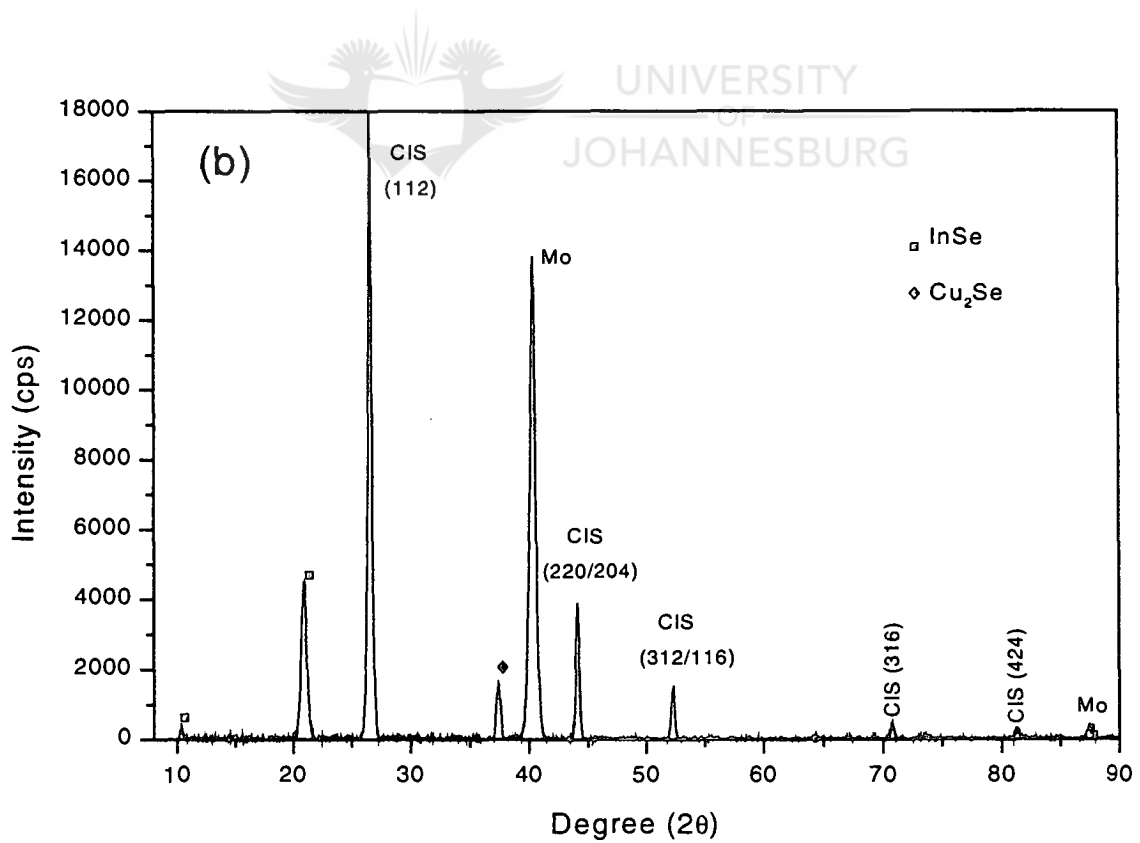
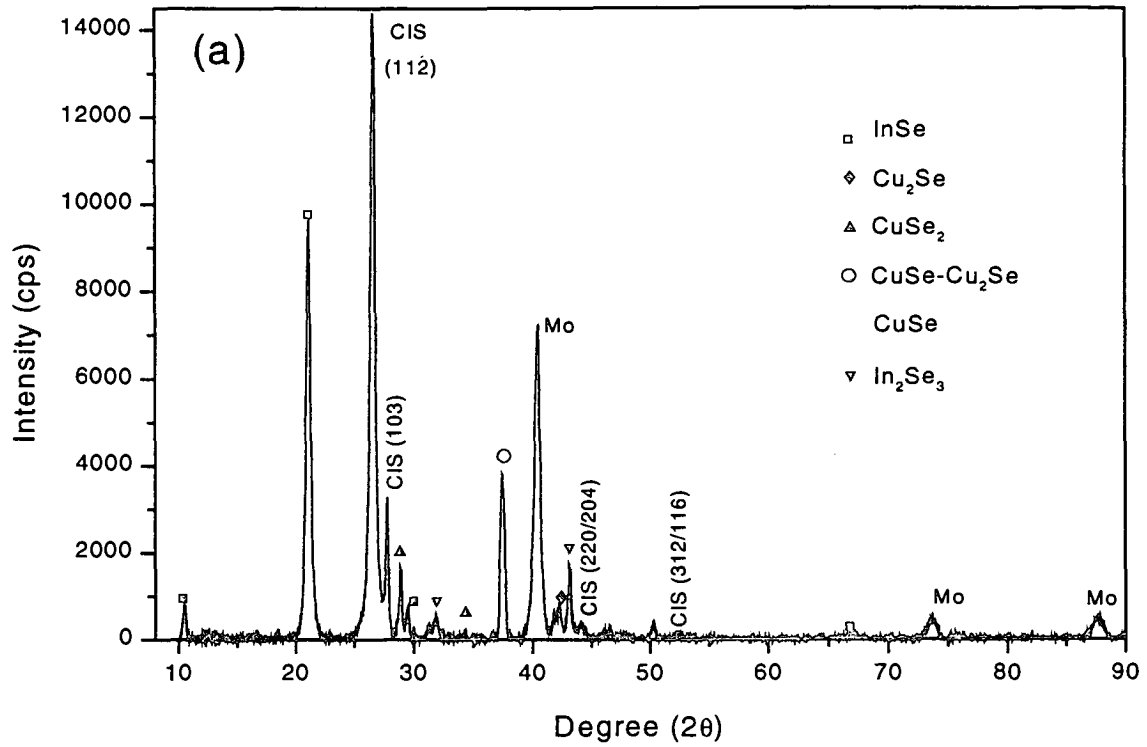


Figure 5.1: SEM micrographs of a typical (a) Mo/InSe/Cu/InSe and (b) Mo/Cu/InSe/Cu precursor alloy.

In contrast, alloys in which the growth sequence was terminated with a Cu layer were characterized by the presence of a large droplet-like structure (Fig. 5.1 (b)). Similar structures were observed for Mo/InSe/Cu structure and the lateral distances between individual droplets increased with increasing In content (or InSe layer thickness). From these studies important conclusions could therefore be drawn. The structural properties of the precursor films were critically influenced by the growth sequence. Irrespective, of bilayers or triple layers, well-interdiffused precursors without the formation of a droplet morphology were obtained when

the growth sequence was terminated with a InSe layer. On the other hand, relatively rough structures with poor surface coverage was obtained in cases when the growth process was terminated with a Cu layer. Other growth parameters such as substrate temperature, growth rate and film composition had marginal influences on the film morphology of the precursor structures.

The variation in the crystalline quality of the precursor films was also clearly reflected by XRD studies. The alloys were prepared at 200°C without any intentional annealing after growth. Fig. 5.2 depicts XRD patterns from various precursor films in which the order of deposition was varied. The bulk composition of these films was kept constant, irrespective of the growth sequence considered. X-ray fluorescence (XRF) studies indicated that the typical thickness of the precursor films was around 2µm with the Se content close to 40 atomic %. From these studies it was evident that a certain degree of interdiffusion occurred between the individual layers. Irrespective of the precursor structure considered, the characteristic (112), (204/220) and (116/312) peaks of the chalcopyrite phase were detected. In addition to these chalcopyrite peaks, a large number of binary phases were also detected. Careful analysis revealed that these additional peaks in the XRD patterns are related to the presence of InSe (JCPDS: 12-0118), In<sub>2</sub>Se<sub>3</sub> (JCPDS: 20-0496), CuSe (JCPDS: 06-0427) and CuSe<sub>2</sub> (JCPDS: 19-0401). These results indicated that selenium diffused from the InSe layers into the Cu layers, resulting in the presence of various Cu-selenide phases. It is also interesting to note that the different stacking orders influenced the relative intensity and number of binary phases present in the precursor alloys. In general, it was observed that structures with InSe as top layer (i.e. Mo/InSe/Cu/InSe and Mo/Cu/InSe) contained a lower density of binary phases. This observation is in line with SEM studies, revealing improved structural properties in the case of precursor alloys in which the growth sequence is terminated with an InSe layer (Fig. 5.1).





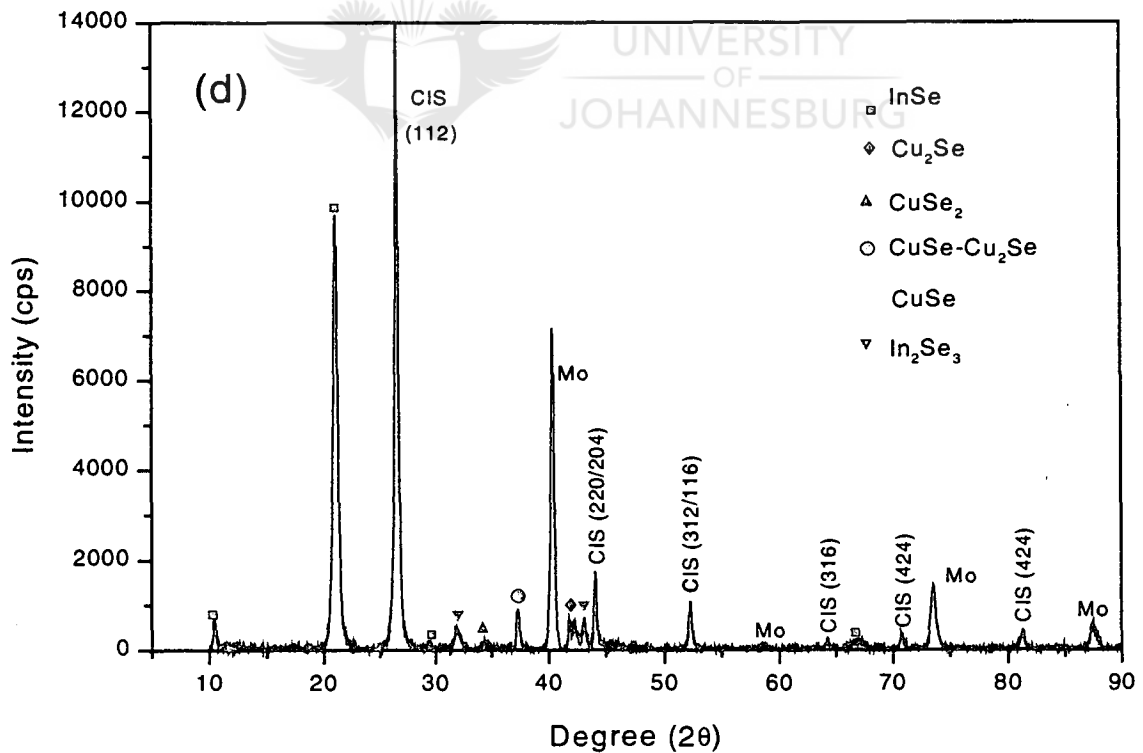
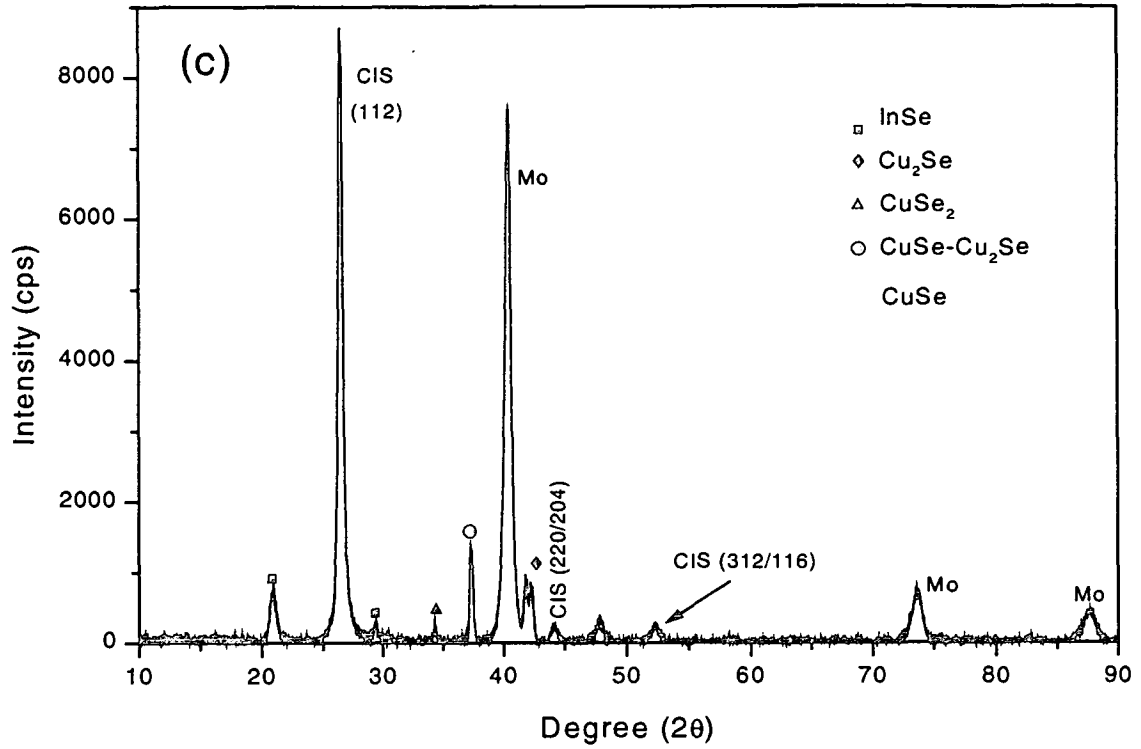


Figure 5.2: XRD patterns from (a) Mo/InSe/Cu, (b) Mo/Cu/InSe, (c) Mo/InSe/Cu/InSe and (d) Mo/Cu/InSe/Cu structures. The precursors were prepared at a substrate temperature of 200°C.

### 5.2.3 Structural Properties of Reacted Precursor Films

The precursor films were finally processed in elemental selenium vapour, in a reactive H<sub>2</sub>Se/Ar atmosphere and by rapid thermal processing. In each case, it was important to determine optimum processing parameters in order to produce device quality material. The degree of success of the various reaction processes was evaluated in terms of the material quality of the final compound films.

#### 5.2.3.1 Reaction of metallic precursors to an elemental Se vapour

In this approach, the metallic precursors (Fig. 4.3) were deposited at 200°C, followed by selenization in vacuum at a substrate temperature of 600°C. The experimental procedure followed during this process is discussed in detail in Section 4.4.2.1. Irrespective the precursor structure considered, fully selenized films (i.e. Se content  $\geq$  50 at. %) could only be obtained after 1h of reaction to Se vapour at substrate temperatures between 550°C and 600°C. Films selenized at lower temperatures or for shorter periods were characterized by poor structural properties (i.e. non-uniform surface morphologies and presence of secondary phases). As expected, the structural properties of precursor films prior to selenization, critically influenced the morphological properties of the final CuInSe<sub>2</sub> absorber films. The most crucial parameter controlling the structural properties of the films was the order of deposition of Cu and InSe in the precursor stacks. Fig. 5.3 shows representative SEM micrographs of the surface morphologies of CuInSe<sub>2</sub> films obtained by the selenization of the precursor films, shown in Fig. 5.1(b). In these cases (Mo/InSe/Cu or Mo/Cu/InSe/Cu) the growth sequence was terminated with a Cu layer. The precursors were selenized at 600°C for 60 minutes. It is important to note that the surface features observed in the precursor layers were translated into the morphology of the CuInSe<sub>2</sub> layer after the selenization step. These films appeared fairly uniform and flat to the naked eye, but SEM studies revealed an inhomogeneous grain growth process. In general, these films were characterized by large (> 5 $\mu$ m) elongated grain structures in which the grain boundaries were not clearly defined. The less defined or diffused edges of the crystallites are indicative of a degree of film recrystallization. This assumption is based on the phase diagram produced by Boehnke and Kühn, which indicates that CuSe melts at approximately 500°C with the consequent formation of a solid solution in CuInSe<sub>2</sub> (Boehnke and Kühn, 1987). Upon cooling, the solution resolidifies with the possible formation of larger crystallites from the coagulation of small ones. This phenomenon was observed for all selenized precursor (bilayers and triple layers) in

which the growth sequence was terminated with a Cu layer. It is believed that the direct exposure of the Cu layer to elemental selenium at temperature above 500°C created significant amounts of CuSe which acted as a flux agent for grain growth. Another important feature of these specific films is the appearance of gaps or holes in the selenized samples.

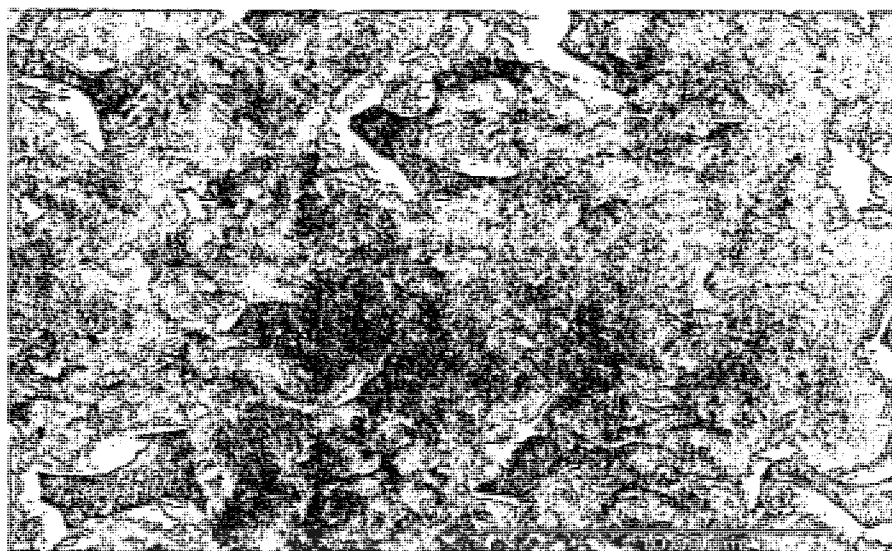


Figure 5.3: SEM micrographs of CuInSe<sub>2</sub> films obtained by selenization of Mo/InSe/Cu or Mo/Cu/InSe/Cu precursors in Se vapour. The composition of this specific film is 22.39 at.% Cu, 26.13 at.% In and 51.48 at.% Se.

This observation is consistent with the morphological properties of the precursor films (Fig. 5.1(b)), revealing clear evidence of incomplete surface coverage (i.e. droplet formation on smooth background). Fig. 5.4 is a typical XRD pattern obtained from the film shown in Fig. 5.3. The typical reflections of the chalcopyrite structure are visible, showing a strong (112) preferred orientation. However, it can be seen that these films contain various Cu-rich secondary phases which is in agreement with the observed morphological features of the film (Fig. 5.3). Some evidence of  $\text{MoSe}_2$  was also detected in these films. It is also important to mention that the bulk composition of this specific layer was slightly In-rich (Cu/In atomic ratio = 0.86). According to the pseudobinary phase diagram (Fig. 2.5) this composition falls within the homogeneity region of single phase  $\text{CuInSe}_2$ . However, these results indicate that binary phases were formed during the selenization process, probably due to the presence of excess  $\text{CuSe}$  at the surface of the layer. It is also important to mention that variations in the selenization parameters (i.e. selenization temperature, reaction period and gas concentration) could not produce single-phase material when using these specific precursors. In addition, the use of triple layers (Mo/Cu/InSe/Cu) instead of bilayers (Mo/InSe/Cu) resulted only in marginal changes in the structural properties of the final absorber films.

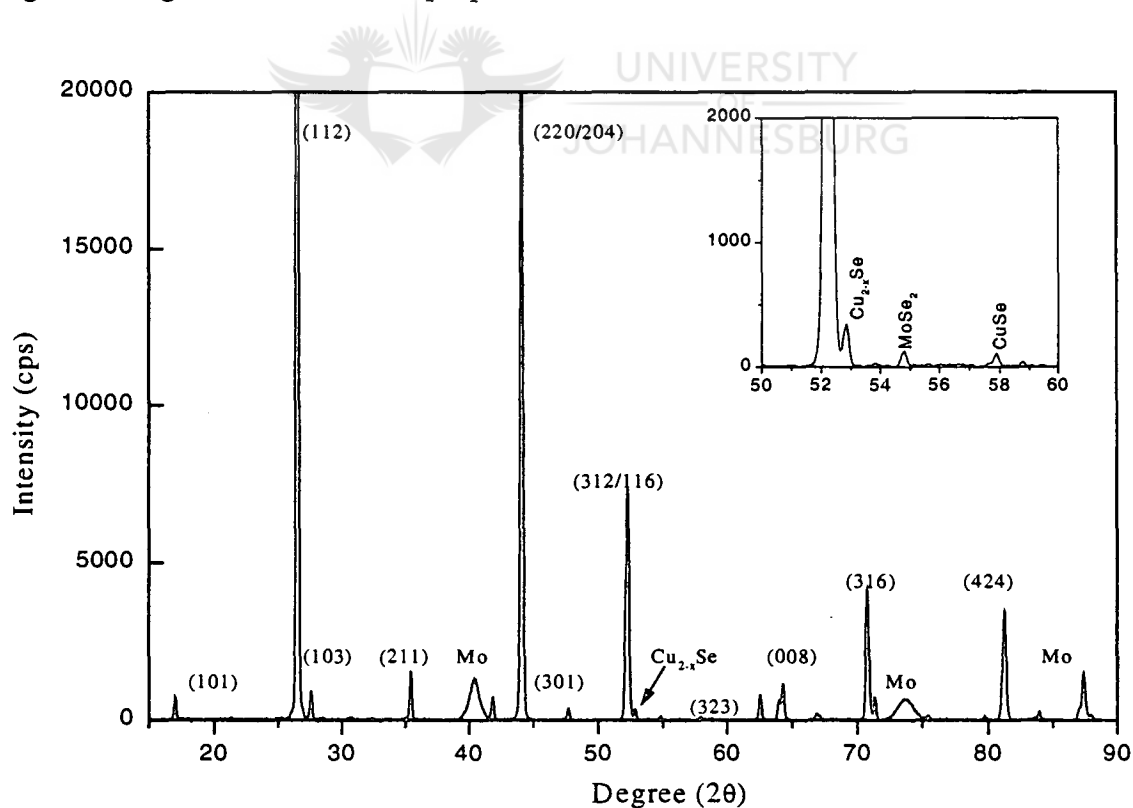


Figure 5.4: XRD pattern from a selenized (in Se vapour at 600°C for 1h) precursor film in which the growth sequence was terminated with a Cu layer.

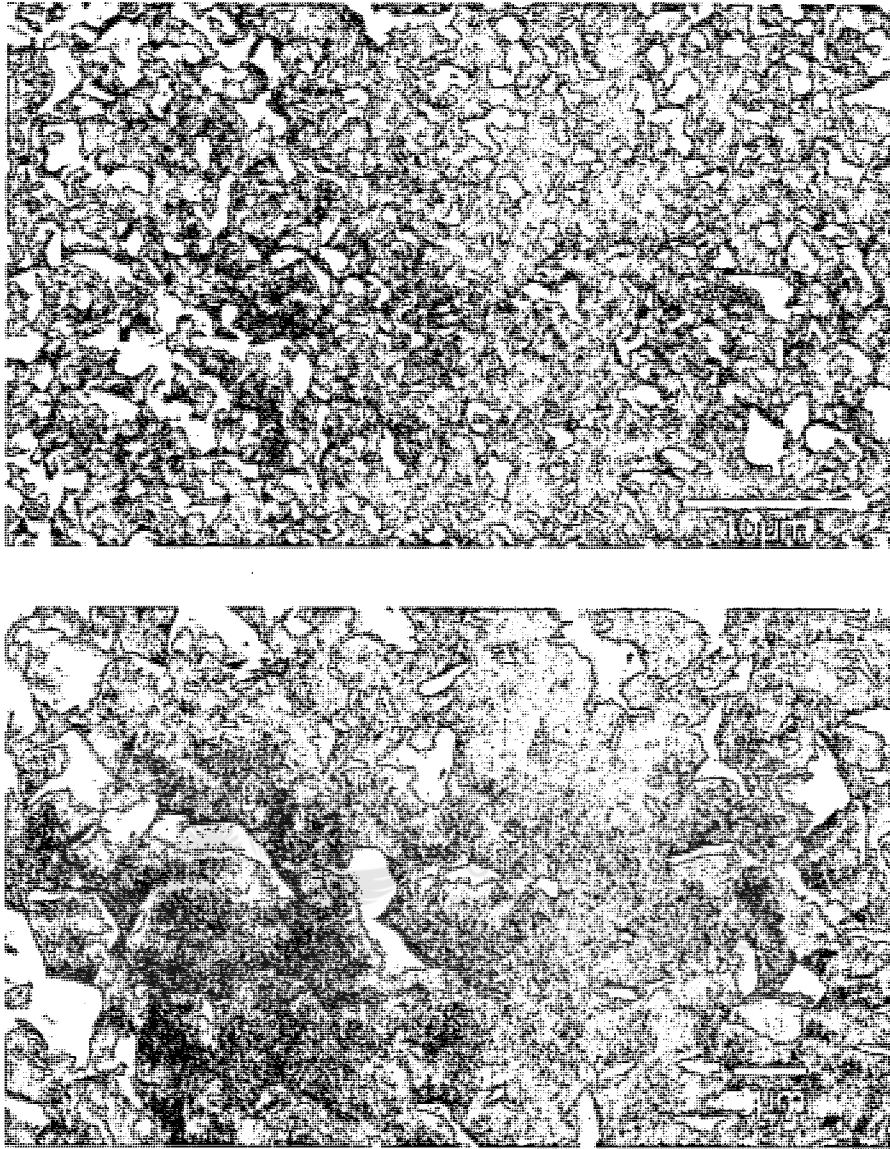


Figure 5.5: SEM micrographs of a typical  $\text{CuInSe}_2$  absorber film produced by treatment of a Mo/Cu/InSe bilayer in Se vapour at  $600^\circ\text{C}$  for minutes.

A dramatic improvement in structural properties was obtained when Mo/InSe/Cu/InSe precursor layers were selenized under identical conditions ( $T_s = 600^\circ\text{C}$  for 60 minutes) in elemental selenium vapour. In this case it is important to note that the layer sequence was terminated with an InSe layer and the Cu layers were either in the middle of stack or at the Mo back contact. Fig. 5.5 are representative SEM micrographs of the typical surface morphology of a  $\text{CuInSe}_2$  thin film produced by the reaction of a Mo/Cu/InSe bilayer to elemental selenium at  $600^\circ\text{C}$ . The most striking difference between these films and that shown in Fig. 5.3 is the large reduction in the average grain size and increase in packing

density. Selenized Mo/Cu/InSe precursors were characterized by excellent structural properties (homogeneous and dense films) with an average grain size around 1 $\mu$ m. The crystallites were clearly faceted with relatively sharp edges. The composition of the specific film, shown in Fig. 5.5, is 23.17 at.% Cu, 26.59 at.% In and 50.25 at.% Se. The superior structural properties of these films were confirmed by XRD studies (Fig. 5.6).

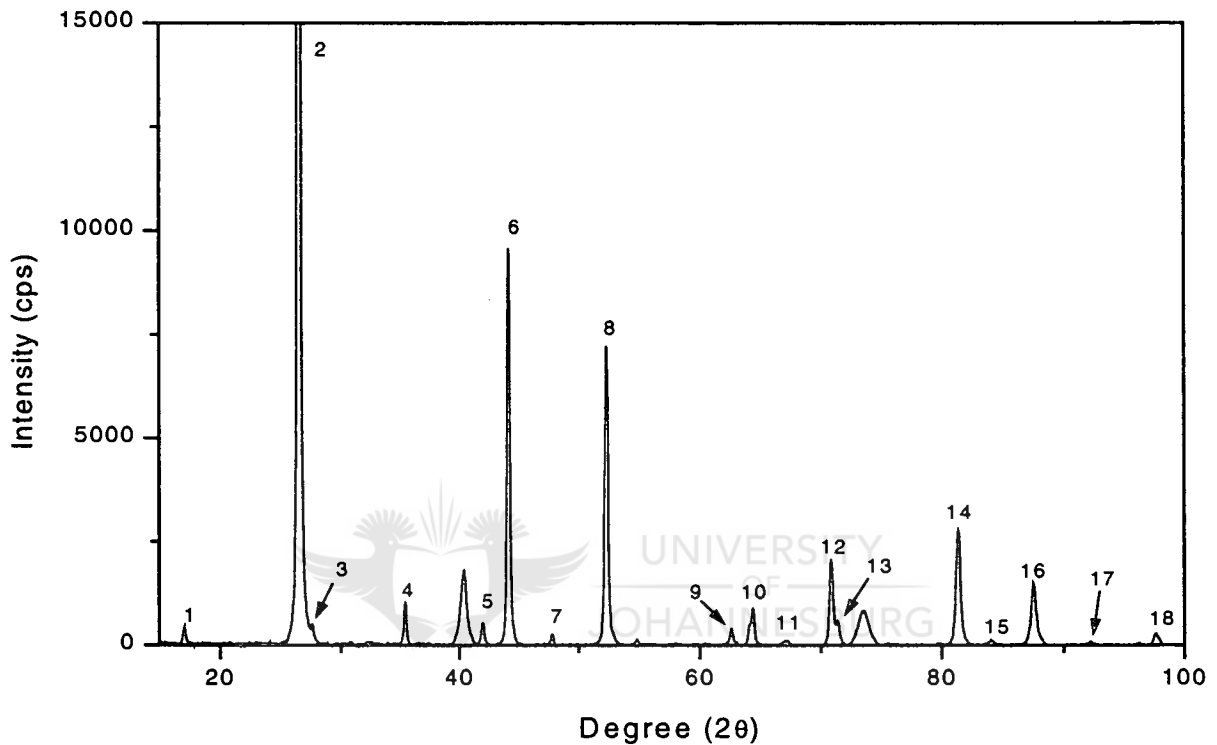


Figure 5.6: XRD pattern obtained from a selenized Mo/Cu/InSe film in Se vapour.

All the major peaks associated with the chalcopyrite phase are clearly visible along with a preferred (112) orientation which is characteristic of this phase. The excellent agreement between the observed d spacing (for example in Fig. 5.6) and the predicted values from published work (Parker et al., 1973) is illustrated in Table 5.1. In addition, virtually no evidence of secondary phases could be detected from these specific films.

Literature			Observed		
<i>d</i> (nm)	<i>I</i> (%)	<i>hkl</i>	<i>d</i> (nm)	<i>I</i> (%)	<i>Peak no</i>
0.5170	6	101	0.5180	0.55	1
0.3351	100	112	0.3349	100	2
0.3220	4	103	0.3224	0.71	3
0.2528	7	211	0.2527	1.30	4
0.2154	2	213	0.2154	0.80	5
0.2046	51	220	0.2044	11.99	6
0.1903	3	301	0.1897	0.34	7
0.1745	25	312	0.1746	8.81	8
0.1482	3	323	0.1481	0.59	9
0.1446	6	400	0.1445	1.22	10
0.1394	1	411	0.1395	0.21	11
0.1330	6	316	0.1329	2.52	12
0.1320	2	413	0.1319	0.80	13
0.1182	10	424	0.1182	3.32	14
0.1152	1	501	0.1152	0.25	15
0.1115	2	336	0.1114	1.85	16
0.1069	1	417	0.1070	0.21	17
0.1025	2	408	0.1024	0.42	18

Table 5.1: Summary of CuInSe<sub>2</sub> X-ray diffraction data as shown in Fig. 5.6. For the purpose of comparison the theoretical expected values are also given.

The morphological properties of a selenized (in Se vapour at 600°C for 1h) Mo/InSe/Cu/InSe precursor are shown in Fig. 5.7. On a morphological level these film appeared similar to selenized Mo/Cu/InSe films with an average grain size around 1µm. The structures were in general dense with no significant evidence of inhomogeneous growth formation. XRD patterns from these layers were similar to that shown in Fig. 5.6.

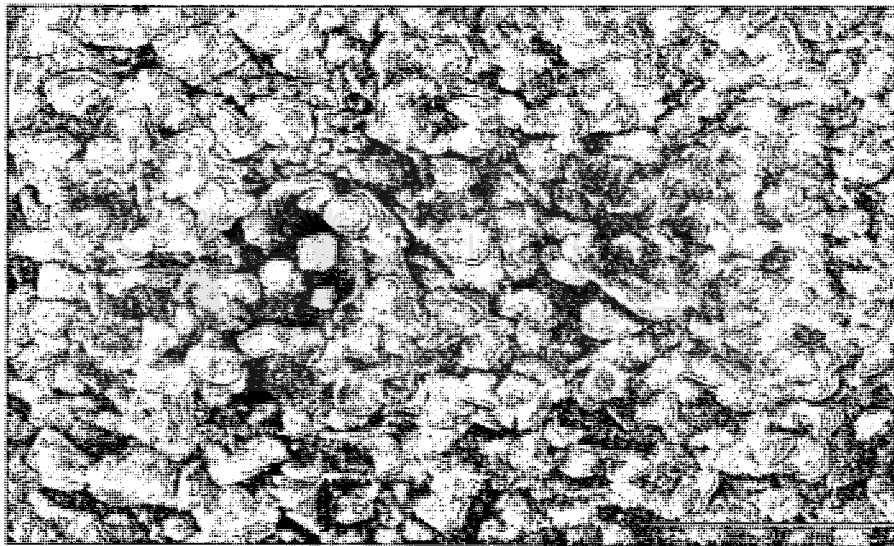
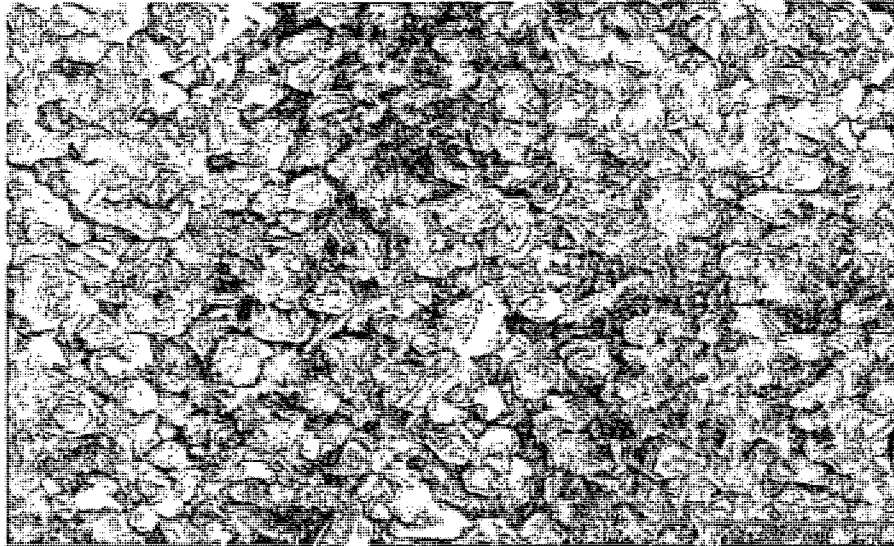


Figure 5.7: SEM micrographs of a typical CuInSe<sub>2</sub> film produced by reaction of a Mo/InSe/Cu/InSe precursor to Se vapour. The composition of this film is 23.2 at.% Cu, 26.1 at.% In and 50.7 at.% Se.

An important aspect in the characterization of thin film chalcopyrite absorber films is composition measurements. As discussed in detail in Section 4.6.2.3, X-ray fluorescence (XRF) is a reliable tool for the measurements of thin film compositions and thicknesses. For typical chalcopyrite absorbers the measured  $K\alpha_{1,2}$  fluorescence intensities are practically linear to the material amount of the respective elements in the sample (Klenk et al., 1999).



This enables the determination of the total film thickness, the composition of the sample and also possible material losses during film processing. Bromium methanol is a well-known etchant for compound semiconductors. This technique was first used in InP processing technologies (Löwe et al., 1990), but has also recently been applied to chalcopyrite materials (Klenk et al., 1991). Although there are more sensitive methods to obtain depth profiles, for example SIMS measurements, interesting conclusions can be drawn from these etching experiments. In this study, samples were repeatedly etched (7 to 10 times) in bromium methanol, followed by measurements of the  $K\alpha_{1,2}$  and  $L\alpha_1$  lines after each etching step. Figs. 5.8 and 5.9 depict the etching profiles of  $\text{CuInSe}_2$  absorber films, prepared by the reaction of  $\text{Mo/InSe/Cu}$  and  $\text{Mo/InSe/Cu/InSe}$  precursors to elemental selenium vapour at  $600^\circ\text{C}$ . The morphological properties of these specific films are shown in Figs. 5.3 and 5.7, respectively. The initial thicknesses of the films were between  $2.2\text{-}2.5\ \mu\text{m}$  and they were simultaneously etched to final thicknesses between  $0.3$  and  $0.5\ \mu\text{m}$ . Due to the proportionality of the  $K\alpha_{1,2}$  line intensity to the material amount of a thin film, a straight line should be obtained for a homogeneous sample in a  $K\alpha_{1,2}$  intensity versus thickness plot. Deviations from this behaviour, caused by sample inhomogeneities, can therefore be observed directly from  $K\alpha$  - line intensity plots. From Figs. 5.8 (a) and 5.9 (a) it can be seen that the  $K\alpha$  - line plots are straight lines, as is to be expected from homogeneous samples. The  $L\alpha$ - line plots in Fig. 5.8 (b) and 5.9 (b) represents more information about the upper part of the layer after each of the etching steps and the signals are by for more influenced by shielding effects than the stronger  $K\alpha_{1,2}$ - lines. In both cases, the behaviour is again typical of what is expected from homogeneous samples (Klenk et al., 1999). The resulting element concentrations as function of material mass per square ( $\text{mg}/\text{cm}^2$ ) are depicted in Fig. 5.8 (c) and 5.9 (c), respectively. From this data, using the density of  $\text{CuInSe}_2$  (Table 2.3), the thickness is then calculated. For the purpose of comparison, the element concentrations as function of calculated layer thickness after each etching step, are given in Figs. 5.8 (d) and 5.9 (d). From this data it is clear that these selenized films are characterized by a relatively high degree of compositional uniformity through the thicknesses of the samples. In both cases ( $\text{Mo/InSe/Cu}$  and  $\text{Mo/InSe/Cu/InSe}$ ), a slight variation in composition ( $\text{Cu/In}$  atomic ratio) was only detected in the region close to the Mo back contact. It can also be seen that the selenium concentration, as function of depth, remained fairly constant around 50 atomic percentage. A summary of the XRF results, depicted in Figs. 5.8 and 5.9, is given in Tables 5.2 and 5.3, respectively.

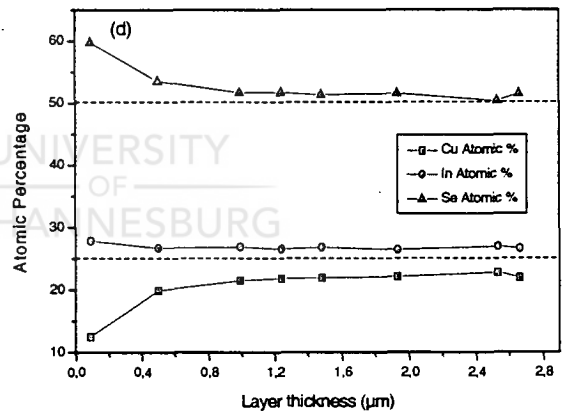
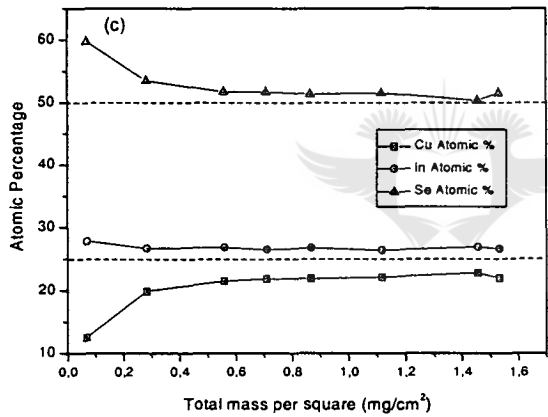
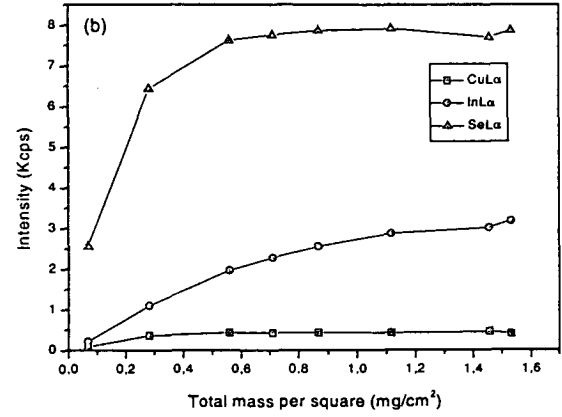
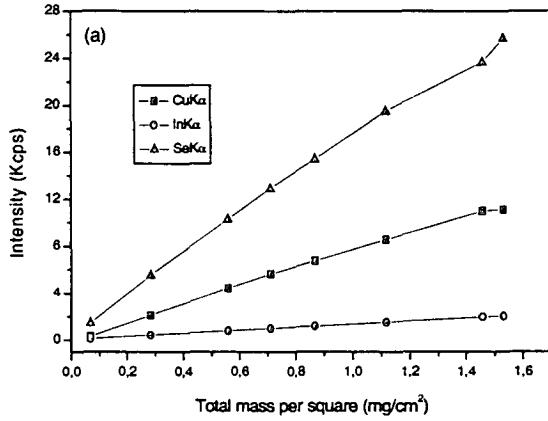


Figure 5.8: Intensity versus mass per square of a repeatedly etched CuInSe<sub>2</sub> sample, prepared by the reaction of a Mo/InSe/Cu precursor to Se vapour. In (a) the Kα<sub>1,2</sub> intensities are shown, while in (b) the Lα<sub>1</sub> intensities. The variation in element concentration as function of total material mass is depicted in (c), while the variation in element concentration as function of total layer thickness is shown in (d).

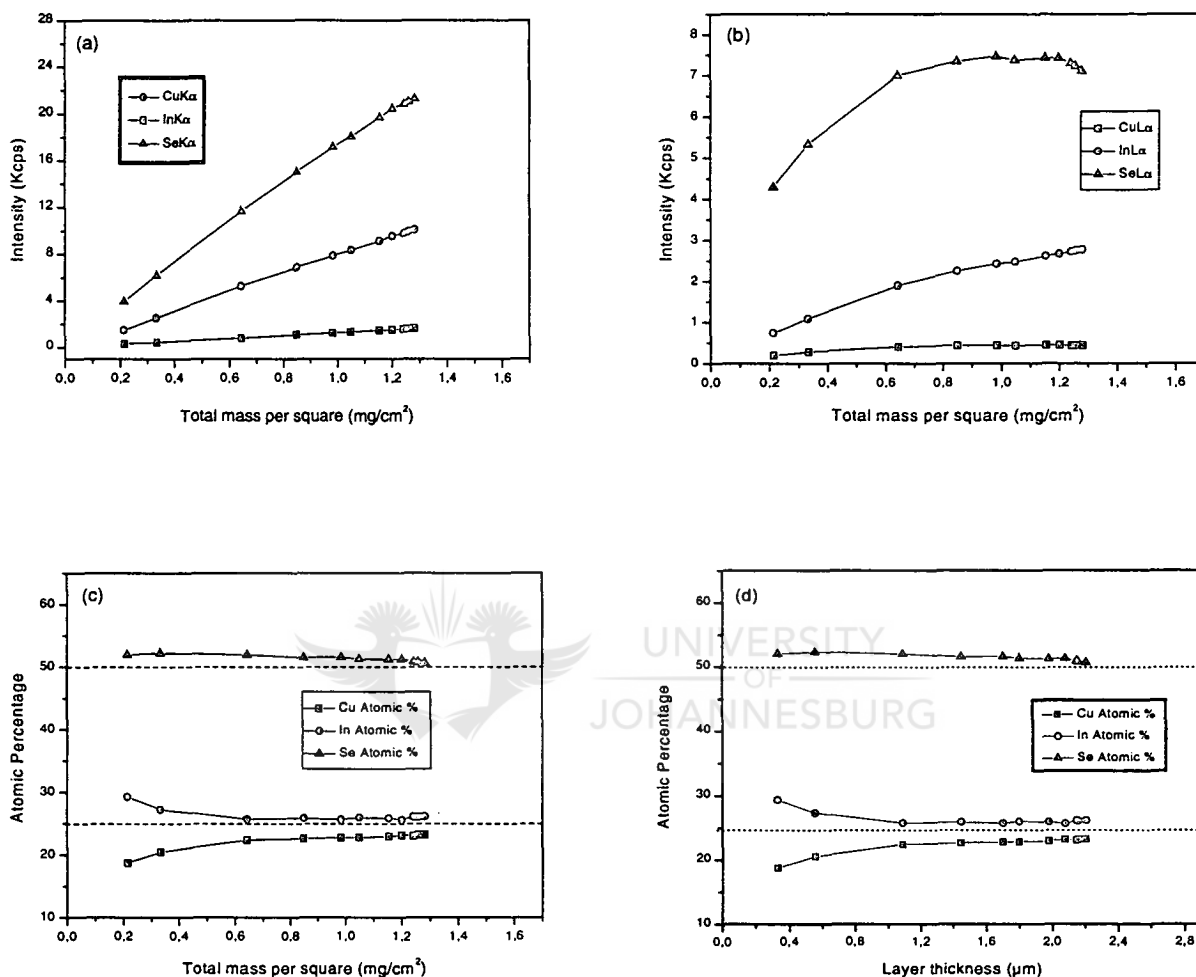


Figure 5.9: Intensity versus mass per square of a repeatedly etched CuInSe<sub>2</sub> sample, prepared by the reaction of a Mo/InSe/Cu/InSe precursor to Se vapour. In (a) the K $\alpha$ 1,2 intensities are shown, while in (b) the L $\alpha$ 1 intensities. The variation in element concentration as function of total material mass is depicted in (c), while the variation in element concentration as function of total layer thickness is shown in (d).

Etching Step	Film Mass (mgcm <sup>-2</sup> )	Film Thickness (μm)	Atomic % Cu	Atomic % In	Atomic % Se	Atomic Ratio [Cu]/[In]
0	1.531	2.66	21.90	26.60	51.50	0.82
1	1.457	2.53	22.75	26.90	50.34	0.85
2	1.117	1.93	22.06	26.40	51.53	0.84
3	0.867	1.48	21.87	26.78	51.35	0.82
4	0.710	1.24	21.81	26.51	51.69	0.82
5	0.559	0.99	21.47	26.83	51.70	0.80
6	0.283	0.50	19.82	26.67	53.51	0.74
7	0.068	0.09	12.44	27.84	59.72	0.44

Table 5.2: Summary of the data obtained from an etched sample, followed by XRF measurements. The sample was prepared by reacting a Mo/InSe/Cu precursor to Se vapour at 600°C.

Etching Step	Film Mass (mgcm <sup>-2</sup> )	Film Thickness (μm)	Atomic % Cu	Atomic % In	Atomic % Se	Atomic Ratio [Cu]/[In]
0	1.281	2.21	23.21	26.1	50.68	0.89
1	1.26	2.16	23.17	26.02	50.81	0.89
2	1.243	2.15	23.01	26.08	50.9	0.88
3	1.201	2.08	23.1	25.6	51.3	0.90
4	1.154	1.98	22.9	25.83	51.26	0.89
5	1.048	1.80	22.75	25.92	51.32	0.88
6	0.983	1.70	22.72	25.66	51.62	0.87
7	0.849	1.45	22.59	25.84	51.56	0.87
8	0.642	1.09	22.34	25.68	51.98	0.87
9	0.332	0.556	20.47	27.25	52.29	0.75
10	0.213	0.33	18.68	29.31	52.02	0.64

Table 5.3: Summary of the data obtained from an etched sample, followed by XRF measurements. The sample was prepared by reacting a Mo/InSe/Cu/InSe precursor to Se vapour at 600°C.

### 5.2.3.2 Reaction of metallic precursors to H<sub>2</sub>Se/Ar

In a second approach, the various metallic precursors depicted in Fig. 4.3 were reacted to a controlled H<sub>2</sub>Se/Ar atmosphere at atmospheric pressure. The experimental procedure followed during this process is discussed in detail in Section 4.4.2.2. In general, it was found that this selenization process is more reactive compared to the previous case (i.e. Se vapour in vacuum). Fully selenized films (i.e. complete transition from metallic to semiconductor behaviour) were obtained at selenization temperatures as low as 450°C. The reaction period was varied between 45 and 60 minutes.

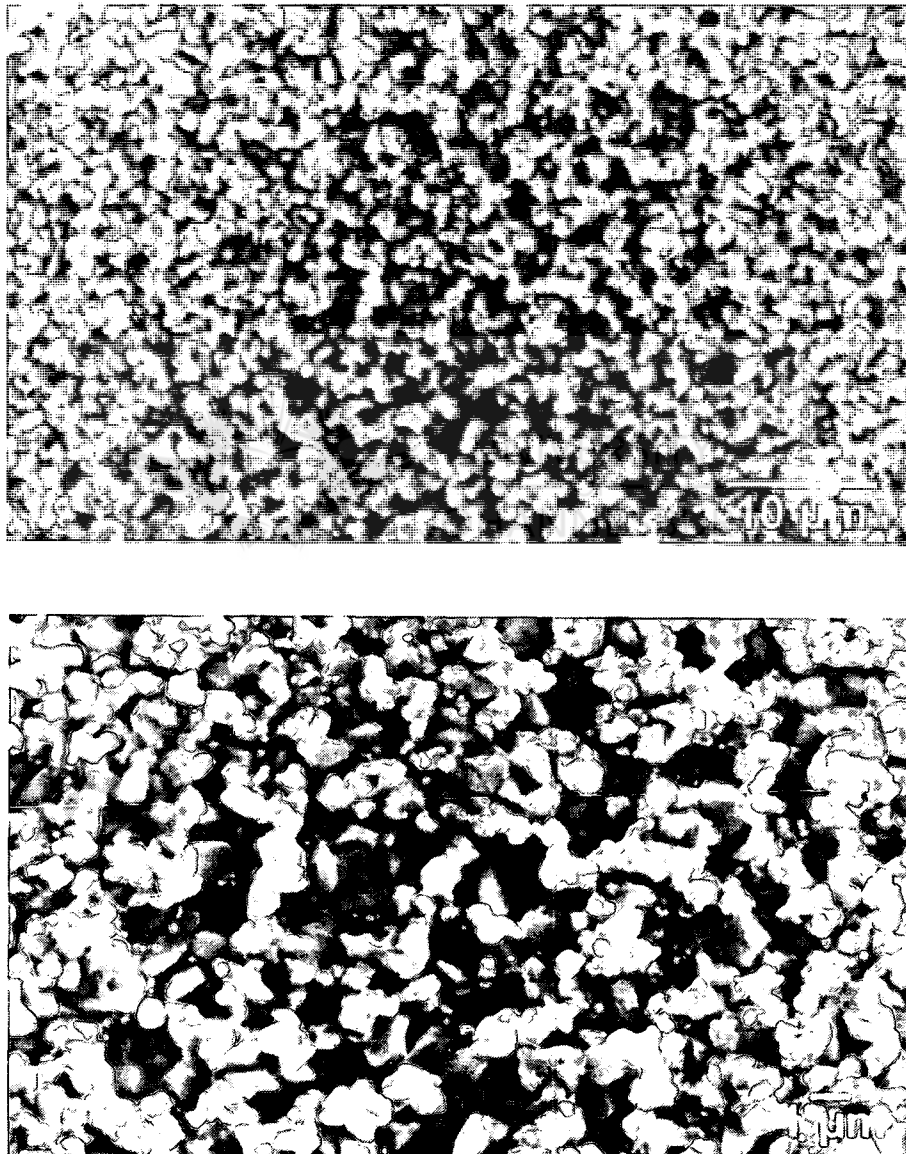


Figure 5.10: SEM micrographs of a H<sub>2</sub>Se treated (at 450°C for 1h) Mo/InSe/Cu/InSe precursor.

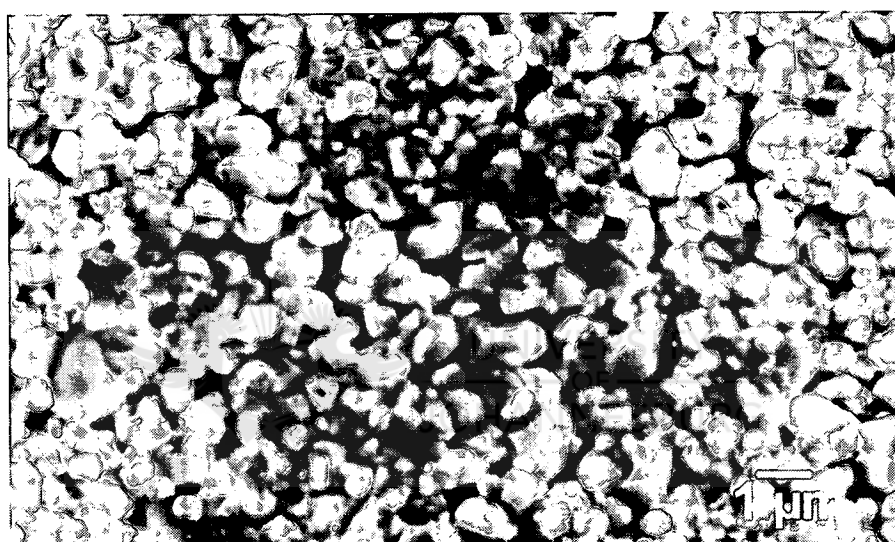
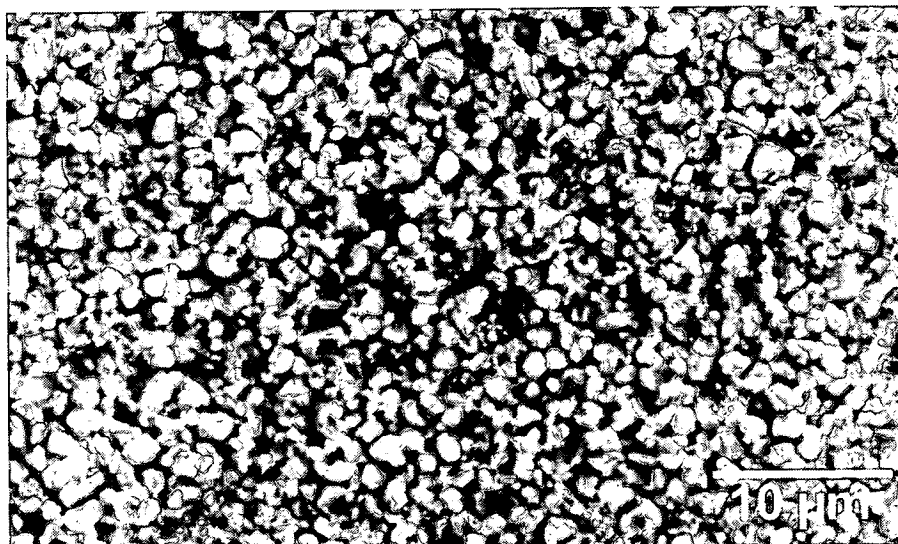


Figure 5.11: SEM micrographs of a  $H_2Se$  treated (at  $450^\circ C$  for 1h) Mo/Cu/InSe/Cu precursor.

The final material quality (i.e. morphological properties and formation of crystalline phases) was again influenced by the stacking order of the metallic films during the precursor formation step. As in the previous case, significant differences were observed when the growth sequence was terminated with a Cu or InSe layer during the precursor formation step. The use of bilayers or triple layers had marginal influences on the material quality of  $H_2Se/Ar$  treated films. Figs. 5.10 and 5.11 are representative SEM micrographs of  $H_2Se/Ar$  treated Mo/InSe/Cu/InSe and Mo/Cu/InSe/Cu precursors, respectively. In both cases, relatively uniform films were obtained with an average grain size around  $1 \mu m$ . Both films were selenized at  $450^\circ C$  for 1h and the Cu/In atomic ratio was around 0.85. The most significant

difference between these two films was the packing density. In the case of selenized Mo/Cu/InSe/Cu films, the selenized films appeared less compact with clear evidence of cavities in between the grains. The presence of these holes are problematic and could result in shunting paths between the front and back contacts which critically influence the performance of solar cell devices. It is interesting to note that similar problems were encountered when these Mo/Cu/InSe/Cu precursors were reacted to Se vapour (Fig.5.3). Comparison of Figs. 5.3 and 5.11, however, reveals a significant difference in structural properties when employing the two different selenization schemes. This difference in morphological properties can be explained by the presence of CuSe flux in samples, selenized in the presence of Se vapour. In the case of elemental Se vapour, a reaction temperature around 600°C was required to obtain fully selenized films. Since this temperature is well above the melting point of CuSe it is reasonable to assume that molten CuSe would be present during the selenization process and hence the formation of large, irregular grain structures (Fig. 5.3). In the case of H<sub>2</sub>Se treatment, maximum temperatures around 450°C were required to produce single-phase material. Since this reaction temperature is well below the melting point of CuSe, it is highly unlikely that CuSe flux would be present during the selenization process. Taking this into account, the observed differences in morphological properties between the respective layers (Figs 5.3 and 5.11) is to be expected.

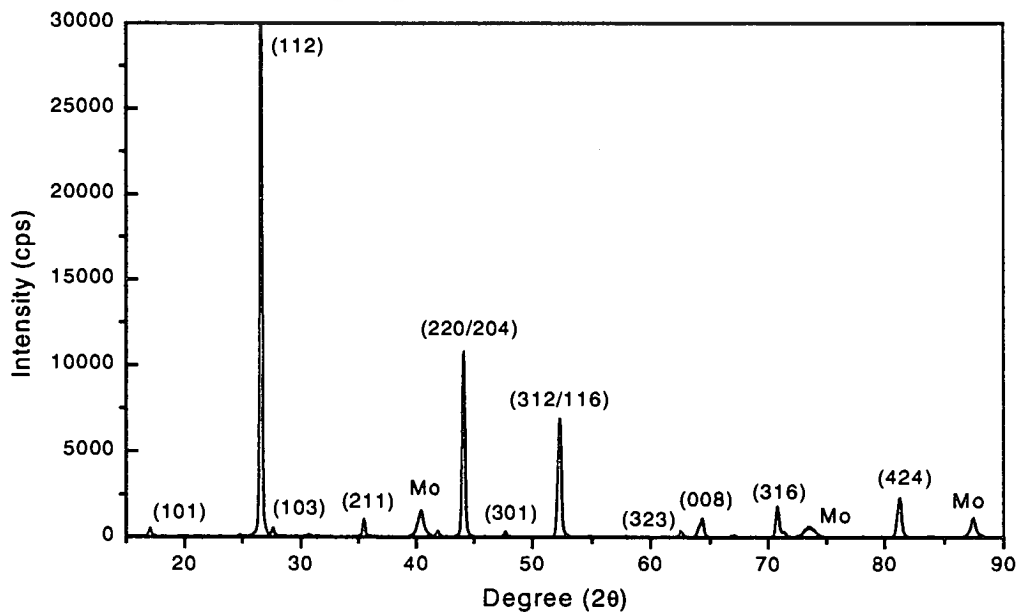


Figure 5.12: XRD pattern obtained from a H<sub>2</sub>Se/Ar treated metallic precursor.



A typical XRD pattern, taken from  $H_2Se/Ar$  treated  $Mo/InSe/Cu/InSe$  or  $Mo/Cu/InSe/Cu$  precursors, are shown in Fig. 5.12. The superior structural properties of these films are clearly reflected by the sharp, well-defined chalcopyrite peaks with a strong (112) preferred orientation. In the case of slightly In-rich films (as depicted in Fig. 5.12), no evidence of secondary phases could be detected.

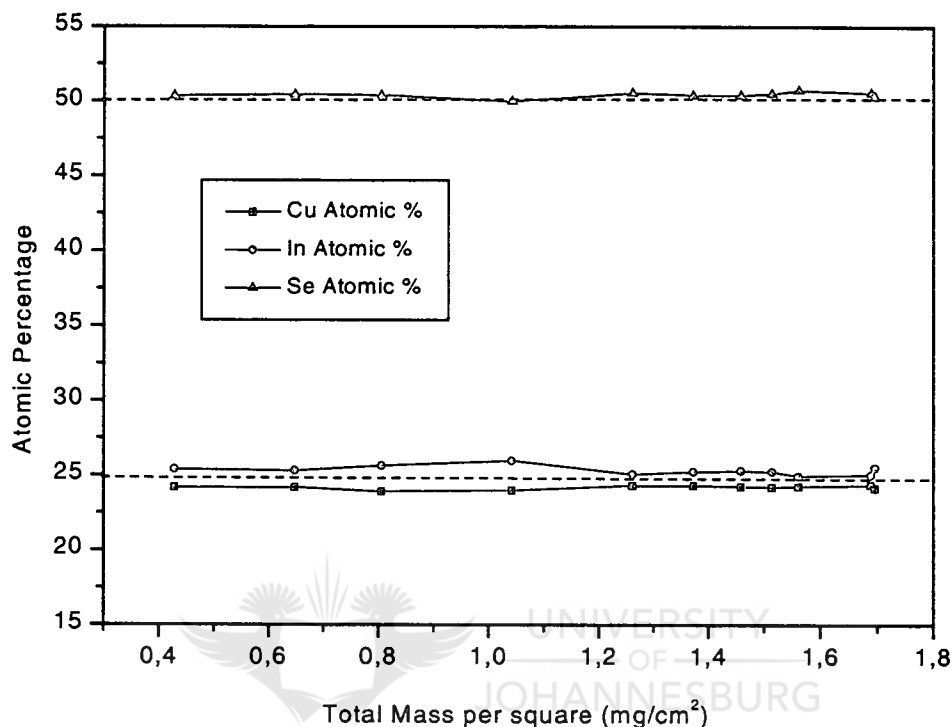


Figure 5.13: Compositional uniformity of a typical  $H_2Se/Ar$  treated metallic precursor. The sample was repeatedly etched in bromium methanol, followed by XRF measurements.

The most striking feature of these specific absorber layers was the extremely high degree of compositional uniformity through the total thickness of the films. A typical example is shown in Fig. 5. 13 in which it can be seen that the concentration of all three elements remained virtually unchanged as function of sample thickness (or the total mass per square). It is important to mention that these results are representative and several etching studies of  $H_2Se/Ar$  treated films showed a similar trend. This high degree of compositional uniformity was also independent of the sample composition and the stacking order of the metallic layers in the precursors prior to selenization.

### 5.3.3.3 Rapid thermal treatment (RTP) of metallic alloys

As an alternative to the use of Se vapour and  $\text{H}_2\text{Se}/\text{Ar}$ ,  $\text{CuInSe}_2$  absorber films were prepared by the rapid thermal processing of the thermally evaporated precursors, depicted in Fig.4.3. In addition, a low thermal budget is assured compared to conventional growth techniques. The most serious draw back of this processing approach was the lost of Se during the fast, high temperature treatment of the metallic precursors. In order to compensate for the loss of Se during RTP treatment, the various stacked precursors (Fig. 4.3) were covered with 1  $\mu\text{m}$  thick Se layer. In this study, the precursors were rapidly heated to  $200^\circ\text{C}$  in 10s and kept at that temperature for 180s. Finally, the temperature was increased to  $550^\circ\text{C}$  in 10s. The duration of the high temperature annealing step at  $550^\circ\text{C}$  was again 180s and that of the total process only 380s. The typical morphological properties of a  $\text{CuInSe}_2$  film, produced by rapid thermal processing, are depicted in Fig. 5.14.

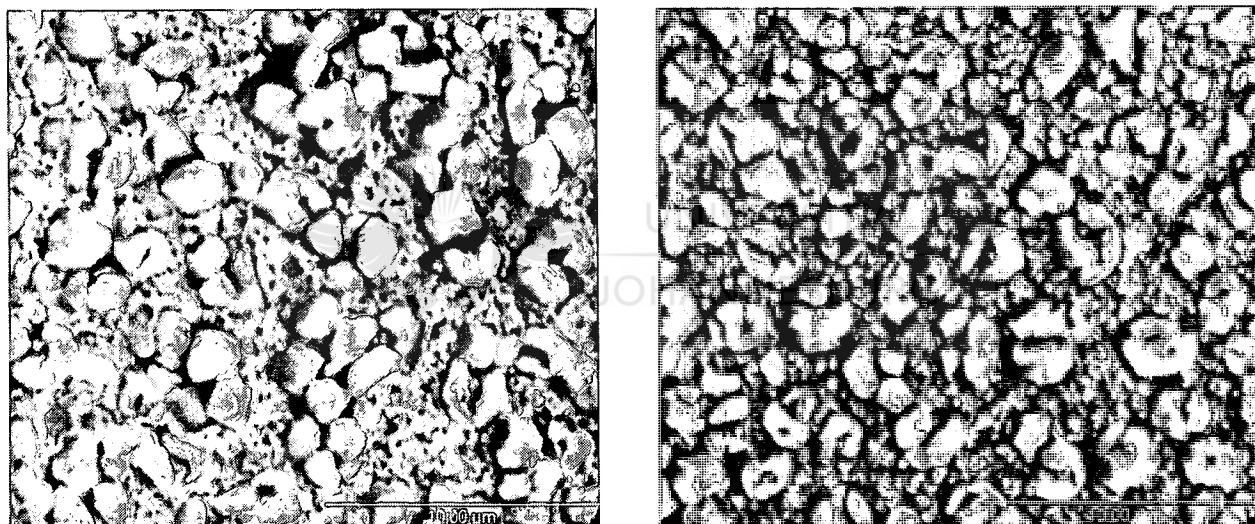


Figure 5.14: Morphological features of a rapid thermal treated metallic precursor.

The final films were generally characterized by inhomogeneous film morphologies with a large variation in grain sizes across the film surface. Careful analysis revealed the presence of large ( $> 1\mu\text{m}$ ), irregular grain structures, superimposed on a relatively flat and smooth background. The composition of the precursors, prior to RTP treatment, was 20.78 at.% Cu, 25.85 at.% In and 53.36 at.% Se. After RTP treatment the final composition of the layers was 21.05 at.% Cu, 29.06 at.% In and 49.88 at.% Se. These results indicated that the RTP treatment resulted in a significant loss of Se and a slight decrease in the Cu/In atomic ratio.

However, it is important to note that the final Se concentration is very close to the required value of 50 at.%, which indicate that it is possible to compensate for the loss of Se by the addition of extra Se to the precursor stack, prior to high temperature processing. If the 1  $\mu\text{m}$  Se layer was omitted from the precursor stack, the final Se content after RTP treatment was below 40 at. %. The stacking order of precursor films had virtually no influence on the  $\text{CuInSe}_2$  film morphology. Figs 5.15 (a) and (b) are XRD patterns taken from a typical precursor, prior to and after RTP treatment, respectively.

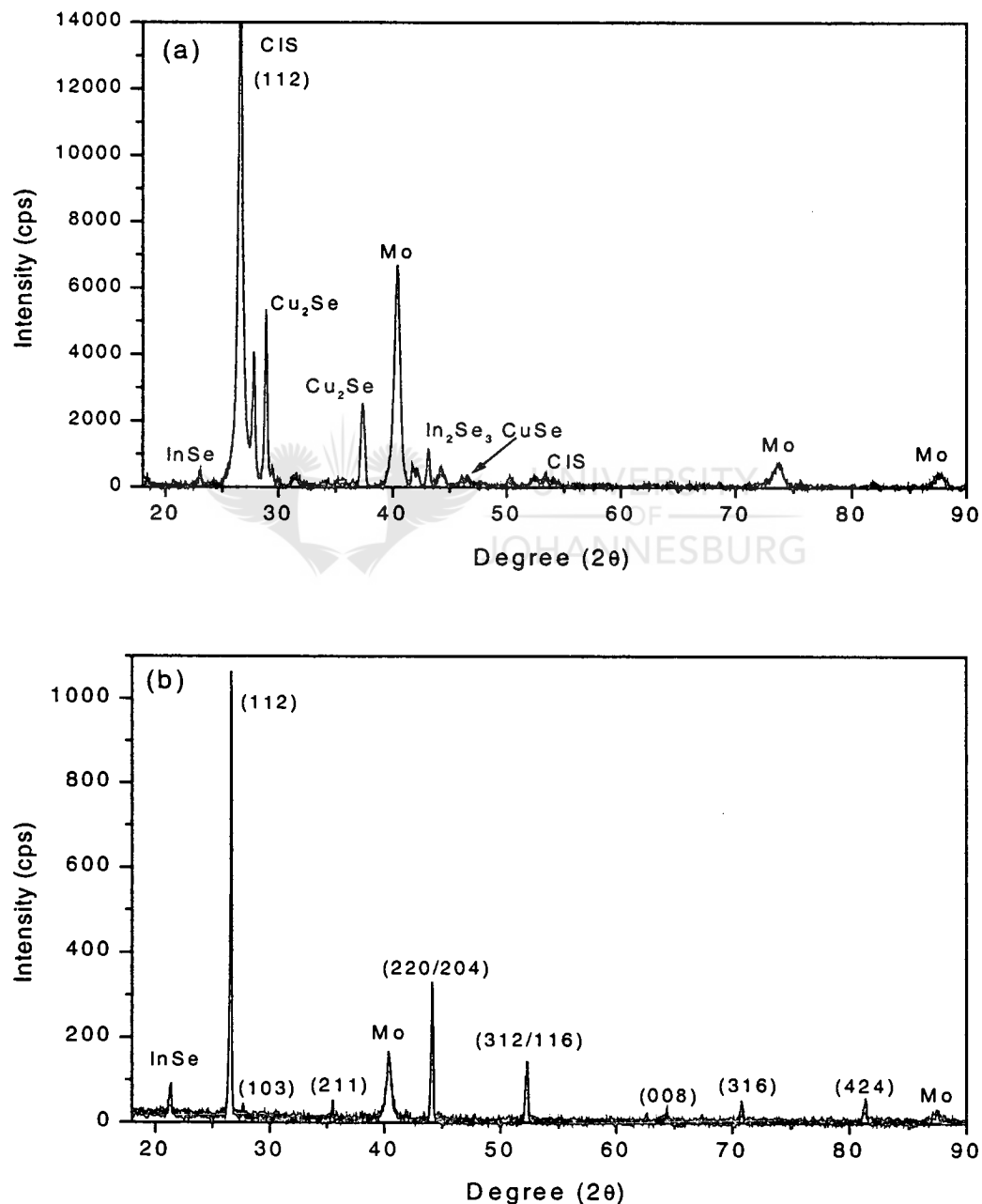


Figure 5.15: XRD patterns from a metallic precursor (a) prior to RTP treatment and (b) after RTP treatment.

As discussed in Section 5.2.2, the precursor structure is dominated by the presence of a large number of binary phases and some evidence of  $\text{CuInSe}_2$  ternary phases (Fig. 5.15(a)). After RTP treatment the crystalline structure changed significantly and XRD studies (Fig. 5.15 (b)) revealed more characteristic chalcopyrite peaks with a corresponding reduction in binary phases. The characteristic (112) peak is also narrower and the (220/204) and (312/116) peaks are better defined after RTP treatment. These observations are indicative of an improvement in crystalline quality. However, it is important to note that the intensities of the chalcopyrite peaks after RTP treatment were still very low and strong evidence of  $\text{InSe}$  binary phases was also detected. Based on these results it is believed that the bulk of the material consists of two separate phases (i.e. Cu-rich  $\text{CuInSe}_2$  and  $\text{InSe}$ ). This is represented on a morphological level by the presence of the large, irregular-shaped grains ( $\text{Cu-rich CuInSe}_2$  grains) and the flat, smooth background (almost pure  $\text{InSe}$  material). This inference was confirmed by XRF measurements.

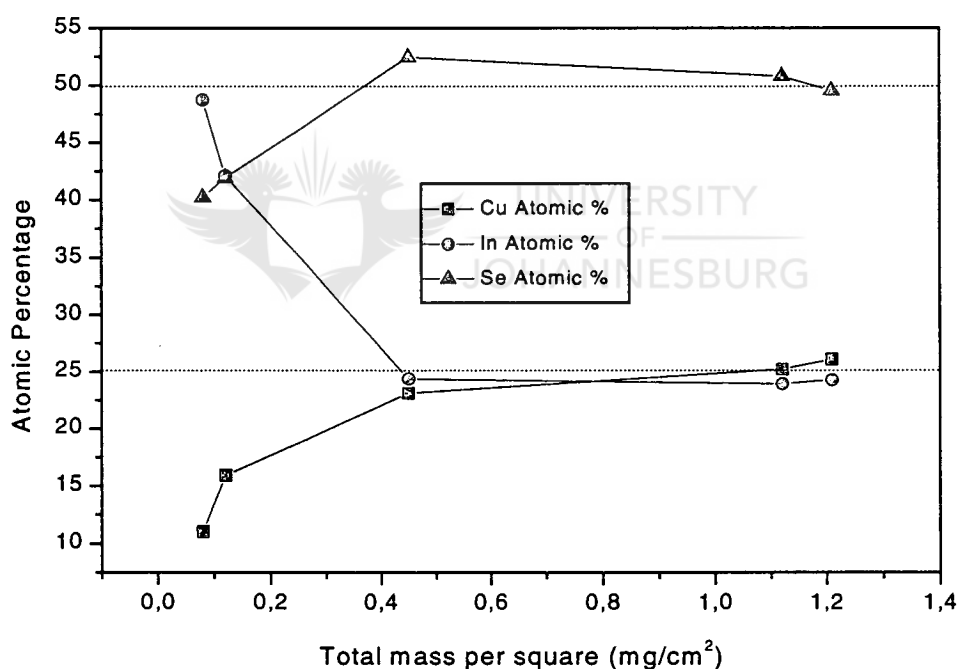


Figure 5.16: Composition versus total mass of material after different etching steps, followed by XRF measurements. The sample was prepared by RTP treatment of a metallic precursor alloy.

It can be seen from Fig. 5.16 that these specific films are characterized by a large variation in compositional uniformity as function of sample depth. The most pronounced difference is in terms of the  $\text{Cu/In}$  atomic ratio. This variation in composition is caused by a sharp increase in

the In content towards the Mo back contact and a corresponding drop in the Cu content. At the surface the film is slightly Cu-rich, while at the region close to the back contact the film contain virtually no Cu. This result is in agreement with SEM and XRD studies, revealing the presence of two separate phases. It can also be seen that the diffusion of Se into the precursor during RTP treatment is non-uniform. After an initial rise in Se content there is a sudden drop in the same region where the In content sharply increases. This phenomenon was observed for all RTP samples.

## **5.2.4 Optical and Electrical Properties of CuInSe<sub>2</sub> Absorber Films**

### **5.2.4.1 Introduction**

The opto-electronical properties of chalcopyrite thin films are critically influenced by the overall bulk compositions of the films. Small deviations from perfect stoichiometry (i.e. Cu/In atomic ratio = 1) critically influence the optical and electrical properties of the CuInSe<sub>2</sub> absorber layers. A clear understanding and optimization of the experimental conditions, influencing the opto-electronic properties, is therefore a prerequisite for the fabrication of high efficiency devices. In this study, the optical and electrical properties of the CuInSe<sub>2</sub> absorber films were evaluated mainly as function of film composition.

### **5.2.4.2 Influence of film composition on the optical and electrical properties**

The presence of intrinsic defect levels influences the photovoltaic properties of CuInSe<sub>2</sub>-based solar cells. The most probable intrinsic defect levels in CuInSe<sub>2</sub> semiconductor materials are given in Table 2.5. As pointed out in Section 4.6.3.3, low temperature photoluminescence (PL) is well suited for the determination of these defect levels in semiconductor materials. As expected, the PL response (energy positions and intensities) depended strongly on the film composition. Fig. 5.17 shows the PL spectrum at 10K from a typical Cu-rich (Cu/In atomic ratio > 1) sample. Small variations in composition (Cu/In atomic ratio = 1.0, 1.5) of Cu-rich samples had no significant influence on the peak positions of the emission lines. In general, these samples were characterized by the presence of two well-defined emission lines at 0.969eV and 0.942 eV. Intensity dependent measurements indicated no shift in the position of these peaks. These transitions are therefore considered as bound to free transitions. The energy separation of 27meV between these peaks are comparable to the reported value for the longitudinal optical (LO) phonon energy in CuInSe<sub>2</sub> (Tanino et al., 1992). It is therefore reasonable to assume that the peak at 0.942 eV is a LO phonon replica of the peak at 0.969

eV. Assuming a band gap value of 1.041 eV, the ionization energy of the peak at 0.969eV is 72meV. Considering the formation energy of defects (Wasim, 1986) and the composition of the specific film, this peak could be attributed to a transition from the bottom of the conductance band (CB) to a  $\text{Cu}_{\text{In}}$  antisite (energy of formation 1.5 eV), which is regarded as an acceptor site (Sites and Hollingsworth, 1987).

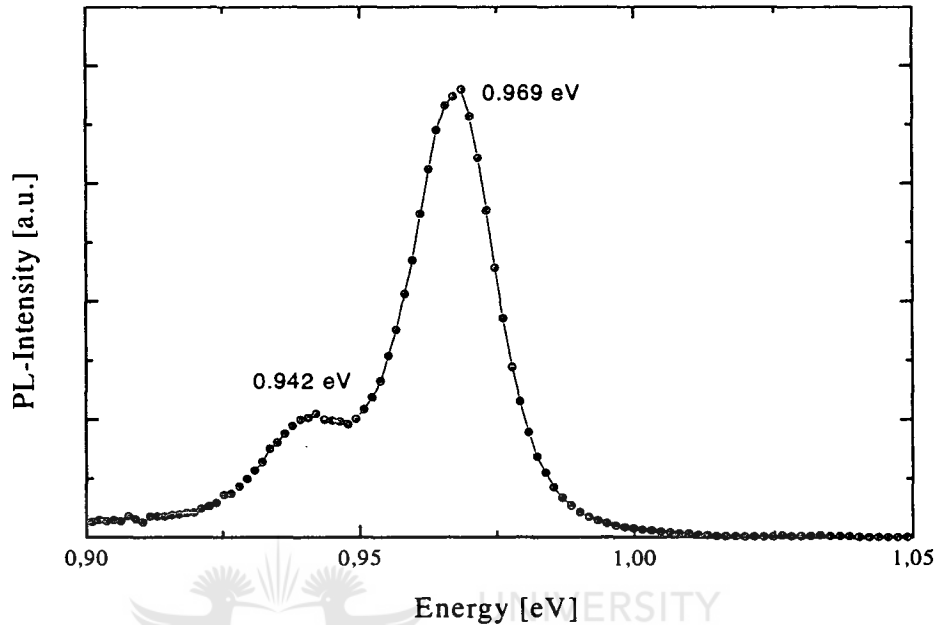


Figure 5.17: PL spectra of a typical Cu-rich  $\text{CuInSe}_2$  sample. Measurements were carried out at 10K with 40 mW excitation power.

The typical PL spectra from various slightly In-rich  $\text{CuInSe}_2$  absorber films (Cu/In atomic ratio = 0.90- 0.92) are depicted in Fig. 5.18. The optical properties of these specific films were characterized by the presence of only one broad emission line at about 0.95 eV, which shifted to higher energies with increasing excitation power. This behaviour is typical for donor-acceptor pair transitions, and in accordance with other workers (Zott et al., 1996) this defect level is attributed to the acceptor level of a copper vacancy ( $V_{\text{Cu}}$ ) and the donor level of a selenium vacancy ( $V_{\text{Se}}$ ). The energy of an emitted photon in a donor-acceptor-pair transition is given by equation (4.7):

$$\hbar\omega = E_g - (E_a + E_d) + \frac{e^2}{4\pi\epsilon_r\epsilon_0 r}$$

where  $E_g$  is the energy of the band gap,  $E_a$  and  $E_d$  are the activation energies of the acceptor and donor level, respectively and the last term is given by the Coulomb interaction of the donor-acceptor-pair at a distance  $r$ .

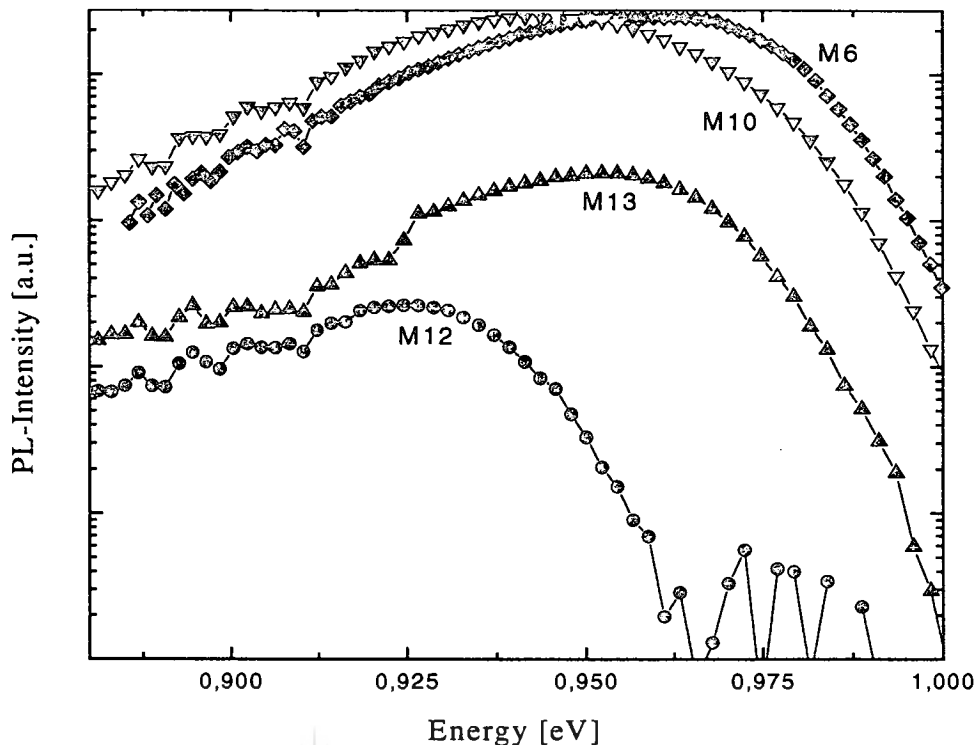


Figure 5.18: PL spectra of various slightly In-rich  $\text{CuInSe}_2$  absorber films, prepared by the reaction of metallic precursors to Se vapour and  $\text{H}_2\text{Se}/\text{Ar}$ . Measurements were taken at 10K.

It is interesting to note from Fig. 5.18 that the position and intensity of the donor-acceptor-pair transition varies from sample to sample. The specific compositions and the measured emission lines from the respective samples are summarized in Table 5.4.

Sample	Composition			[Cu]/[In]	PL Response (eV)
	Cu	In	Se		
M6	24.48	26.68	48.84	0.92	0.962
M10	24.10	26.54	49.36	0.91	0.952
M12	23.44	25.80	50.76	0.91	0.930
M13	24.06	26.10	49.84	0.92	0.946

Table 5.4: Summary of composition and PL response from samples indicated in Fig. 5. 18.

The exact compositions of the samples were determined from XRF measurements. According to equation (4.7), the shift of the maximum of this transition must be related to a change in the Coulombic interaction. In this case, this phenomenon can be explained by the variation of the concentration of one of the possible intrinsic defect levels (i.e.  $V_{Se}$  or  $V_{Cu}$ ). It can be seen from Table 5.4 that the selenium content of samples varies significantly, while the Cu/In atomic ratio remained virtually unchanged. Based on these results the observed PL can be explained. It is based on the following assumptions. The density of the dominating acceptor states ( $V_{Cu}$ ) is constant in these specific samples. It is also reasonable to assume that the Se content influence the concentration of  $V_{Se}$  and hence the PL response. A lower Se content in the bulk of the film should result in an increase in the concentration of  $V_{Se}$ . The higher density of  $V_{Se}$  in turn results in a higher Coulombic interaction between the donor-acceptor-pair, and therefore in a shift of the peaks to higher energies and an increased PL intensity, as observed in Fig. 5.18. These PL results emphasize the fact that the optical properties of polycrystalline CIS is critically influenced by the selenization conditions and therefore require careful optimization.

The electrical parameters, including resistivity and carrier concentrations, were determined by four-point probe and Hall measurements. The theoretical aspects of these characterization techniques are discussed in detail in Section 4.6.4. In these electrical studies, samples were used in which the Mo layers were omitted. As indicated in Table 5.5, the electrical properties were strongly dependent on their bulk compositions, as determined by XRF studies.

[Cu]/[In]	Resistivity ( $\Omega$ cm)	Carrier Density ( $\text{cm}^{-3}$ )
1.1 - 1.3	< 0.01	$10^{19} - 10^{20}$
0.85 - 0.95	20 - 40	$2 - 5 \times 10^{16}$
0.4 - 0.6	100 - 200	$< 5 \times 10^{15}$

Table 5.5: Electrical properties of  $\text{CuInSe}_2$  polycrystalline thin films as function of composition.

Cu- rich films (Cu/In atomic ratio > 1) were characterized by low resistivities in the  $10^{-1} - 10^{-3}$   $\Omega$  cm range at room temperature. The low resistivity values for Cu-rich samples are attributed to the presence of Cu-rich secondary phases (e.g.  $\text{CuSe}$ ,  $\text{CuSe}_2$  and  $\text{Cu}_{2-x}\text{Se}$ ) which exhibit



quasi-metallic behaviour. The resulting carrier concentration of the Cu-rich absorber films generally ranges between  $10^{19}$  and  $10^{20}$   $\text{cm}^{-3}$ . In-rich films (Cu/In atomic ratio = 0.4-0.6) of comparable thickness were characterized by relatively high resistivities ( $\rho \geq 100 \Omega \text{ cm}$ ) with the net acceptor concentrations below  $5 \times 10^{15}$   $\text{cm}^{-3}$ . Hall measurements conducted on slightly In-rich films (Cu/In atomic ratio = 0.85-0.95) films yielded carrier densities of  $2\text{-}5 \times 10^{16}$   $\text{cm}^{-3}$ .

### 5.3 Growth and Characterization of CdS and ZnO

#### 5.3.1 Introduction

Another important aspect of this study was the development of a standard CdS/ZnO window layer technology in our laboratories. It is known that the material properties of the CdS buffer layer and ZnO window layer critically influence the performance of the completed solar cell device. If deposited under sub-optimized condition, the performances of devices can be reduced significantly or in the worse scenario devices could even fail to function. In this study, the structural, optical and electrical properties of CdS and ZnO layers were evaluated and correlated against various growth parameters. From these studies growth parameters were determined for the deposition of high quality CdS and ZnO thin films.

#### 5.3.2 Optimization of CdS Layer Thicknesses

The CdS buffer layers were deposited by means of a chemical bath depositions (CBD) process. The experimental details followed during this process are given in Section 4.5.1. For optical characterization layers were deposited on glass substrates. The most crucial parameter influencing device performance is the CdS layer thickness. From literature an optimum layer thickness around 50nm is suggested. If the buffer layer thickness is far below (10–20nm) this critical value, incomplete coverage of the relatively rough CIS absorber layer results. If the buffer layer thickness is far above (80-100nm) this critical value around 50nm, absorption in the CdS buffer layers increases significantly. The thickness of CdS films deposited by CBD on both sides of a glass substrate can be determined with a mechanical stylus instrument, but this requires a step in the film and is therefore a destructive and time consuming method. It was thus decided to develop a technique to determine the thickness with a fast, non-destructive optical method.

The thickness  $d$  of a single uniform thin film on a transparent substrate can be determined from the optical transmission spectra by using analytical mathematical formula (Swanepoel, 1989). This, however, requires that at least one interference fringe must be observed in the spectrum, which means that  $d > \lambda/4n$ . The refractive index of the film and substrate must also be known or can be calculated from the transmission spectra if at least 2 interference fringes can be observed. In this study, the optical system consists of *two* identical uniform layers CdS on both sides of a non-uniform transparent substrate. The thickness of each film is less than 50nm, which means that no interference fringes will be observed in the near infrared and optical region of the spectrum. The usual optical methods for determining  $d$  and  $n(\lambda)$  can thus not be applied. This situation is now treated as follows: assuming the refractive index  $n(\lambda)$  and extinction coefficient  $k(\lambda)$  is known for CdS from the literature, a series of  $T(\lambda)$  curves are calculated for thicknesses  $d = 10, 20, 30, \dots, 100\text{nm}$  of CdS films on both sides of the glass. Both glass and CdS are fairly transparent in the wavelength range 600nm to 2000nm and for this range the extinction coefficient  $k$  for both CdS and glass can be taken as zero, resulting in simpler mathematical expressions for  $T(\lambda)$ . The transmission of the double layer CdS films on glass is measured and this spectrum is superimposed on the template of calculated theoretical values of  $T(d, \lambda)$ . By inspecting the position of the experimental spectrum relative to the theoretical curves, a very good estimate of the thickness  $d$  can be made. It was found that the accuracy of this method was better than  $\pm 5\%$  for CdS films with thicknesses between 10 and 50nm.

The value of  $T$  for a multilayer structure cannot be obtained as an analytical expressions and the matrix formalism has to be used (Swanepoel, 1989): layer 1 being the front CdS film with thickness  $d$ ; layer 2 the thick glass substrate and layer 3 an identical rear CdS film also with thickness  $d$ . It is assumed that the system is surrounded by air with refractive index  $n_0 = 1$ . It must be emphasised that the transmission of the above system is not equivalent to a system air/CdS/glass/air with the thickness of the CdS film of  $2d$ .

The complex scattering matrix  $S$  for the air/CdS/glass/CdS/air system is now given by (Swanepoel, 1989):

$$S = I_{01} L_1 I_{12} L_2 I_{23} L_3 I_{30}$$

where, for example,

$$I_{01} = \begin{pmatrix} 1 & r_{01} \\ r_{01} & 1 \end{pmatrix} \quad L_1 = \begin{pmatrix} e^{i\beta_1} & 0 \\ 0 & e^{-i\beta_1} \end{pmatrix}$$

and

$$r_{01} = \frac{n_0 - n_1}{n_0 + n_1} \quad \beta_1 = 2\pi n_1 d_1 / \lambda$$

with similar expressions for  $I_{12}$ ,  $I_{23}$ ,  $I_{30}$ ,  $L_2$  and  $L_3 = L_1$ .

The transmission is now given by:

$$T = SS^* / \tau\tau^*$$

where

$$\tau = (1 - r_{01})(1 - r_{12})(1 - r_{23})(1 - r_{30})$$

The above expression for  $T$  gives the transmission for 3 perfectly parallel and homogeneous films. The calculated  $T$  will thus display the interference fringes of both the two CdS films as well as that of the glass, since the term  $L_2$  in the scattering matrix  $S$  contains the phase information of the glass substrate. In this study of the air/CdS/glass/CdS/air system, the glass substrate was thick and non-uniform, resulting in the destruction of the coherent combination of the multiple reflections in the glass. This effect can be modelled by numerically integrating out the phase contribution of layer 2. This is done by calculating  $T$  for a large number of phase angles  $\beta_2$  in the range between 0 and  $\pi$ . The transmission  $T$  for each  $\lambda$  is then given by:

$$T = \frac{1}{N} \sum_{j=1}^N T_j$$

The above expression gives the theoretical value of two coherent films with an incoherent film in between. Due to the periodic nature of the trigonometric functions, it was found that a value of  $N = 8$  yields a precision of better than 0.01%, which is well within the experimental accuracy. The 8 values of  $\beta_2$  used in the numerical integration thus were  $\beta_2 = 0, \pi/8, 2\pi/8,$

$3\pi/8 \dots 7\pi/8$  radians. The refractive index for the glass was determined by measuring the transmission of the substrate  $T_g$  alone and calculating  $n_2(\lambda)$  from the formula:

$$n_g(\lambda) = \left(1/T_g^2(\lambda) - 1\right)^{1/2} + 1/T_g(\lambda)$$

In the wavelength range 600 to 2000nm the refractive index for the glass substrates used can be represented by the following mathematical expression:

$$n_2(\lambda) = 1.514 + 1.008 \times 10^4 / \lambda^2 - 2.194 \times 10^8 / \lambda^4$$

The refractive index of crystalline CdS was obtained from the literature (Palik, 1985). In the wavelength range 600 to 2000nm it can be represented by the following analytical expression:

$$n_1(\lambda) = n_3(\lambda) = 2.3031 + 1.0539 \times 10^4 / \lambda^2 + 2.0121 \times 10^{10} / \lambda^4$$

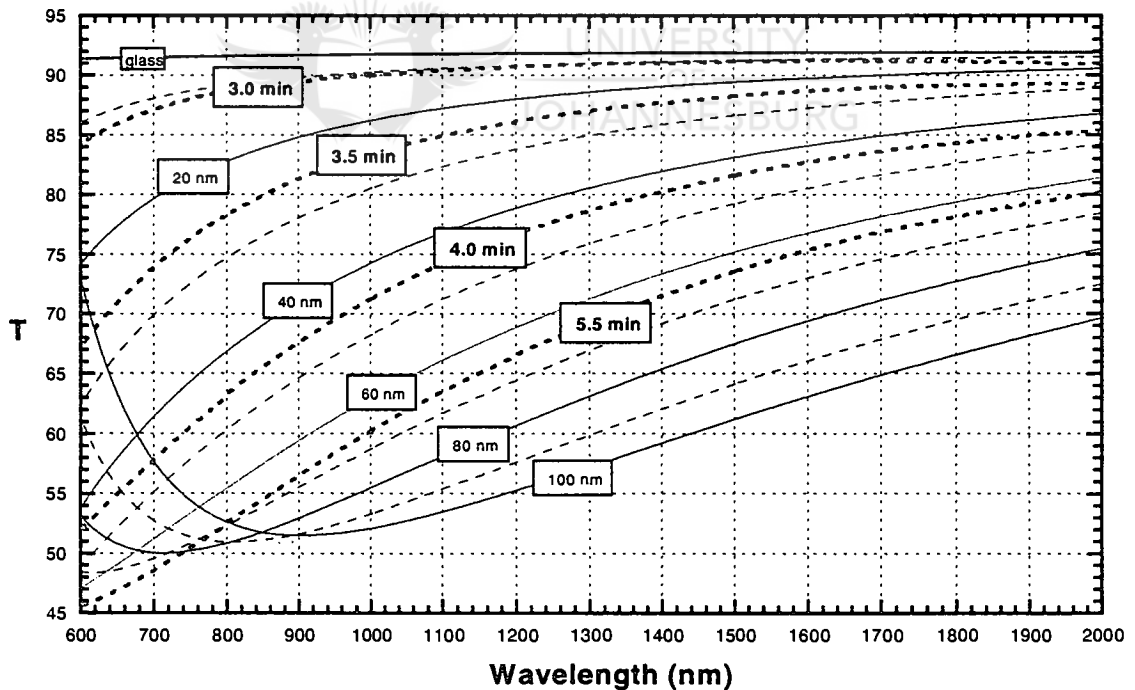


Figure 5.19: Calculated transmission spectra for the system air/CdS/glass/CdS/air for various thicknesses of the CdS layers (thin lines). The heavy broken red lines are the experimental spectra for CdS films grown for different times.

Figure 5.19 shows the theoretical calculated transmission spectra for the air/CdS/glass/CdS/air system for thicknesses of both CdS films of 10, 20, 30, 40, 50, 60, 70, 80, 90 and 100nm in the wavelength range 600nm to 2000nm. Superimposed on the spectra are the experimental spectra of CdS films grown for 3.0, 3.5, 4.0 and 5.5 minutes. By inspection of Fig. 5.19, the following thicknesses were obtained:

Dep. Time (min)	Thickness (nm)	Dep. Rate (nm/min)
3.0	11	3.67
3.5	25	7.14
4.0	44	11.00
5.5	65	11.81

Table 5.6: Summary of the experimental CdS layer thicknesses for different deposition periods, as determined from Fig. 5. 19.

The deposition rate is not linear with time, being slower during the initial growth stages, but seems to be constant for thicknesses larger than 40 nm. This can be explained in terms of initial island growth and once the individual islands coalesce to cover the substrate completely, growth is faster and the growth rate remains constant. If a CdS film of 50nm is required, the deposition time should be about 5 minutes, for the specific conditions under which these films were deposited. It can therefore be seen from Fig. 5.19 that the optical method developed for determining the experimental thicknesses of CdS buffer layers works very well. The values were in some cases compared to those obtained with a stylus instrument and the results were in good agreement. However, the advantages of the optical method are that it is fast and non-destructive. The fact that the experimental spectra follow the expected shapes of the theoretical transmission spectra also indicates that the refractive indices of the films are the same as those of pure polycrystalline CdS. The films are therefore of good structural and compositional quality polycrystalline CdS. Slight deviations from the theoretical spectra are probably due to the inclusion of some unwanted impurities in the film or residual chemicals on the surface of the films. The films were furthermore very uniform, as was also confirmed by SEM studies.

Figure 5.20 shows the experimental transmission spectra in the wavelength range 300 to 2500 nm. For the purpose of comparison, the transmission spectrum of the glass substrate is also

shown. The films were grown for 3, 3.5, 4, 4.5 and 5.5 minutes, respectively. All films show the start of strong absorption at about 500nm, corresponding to the optical gap of 2.48eV for CdS.

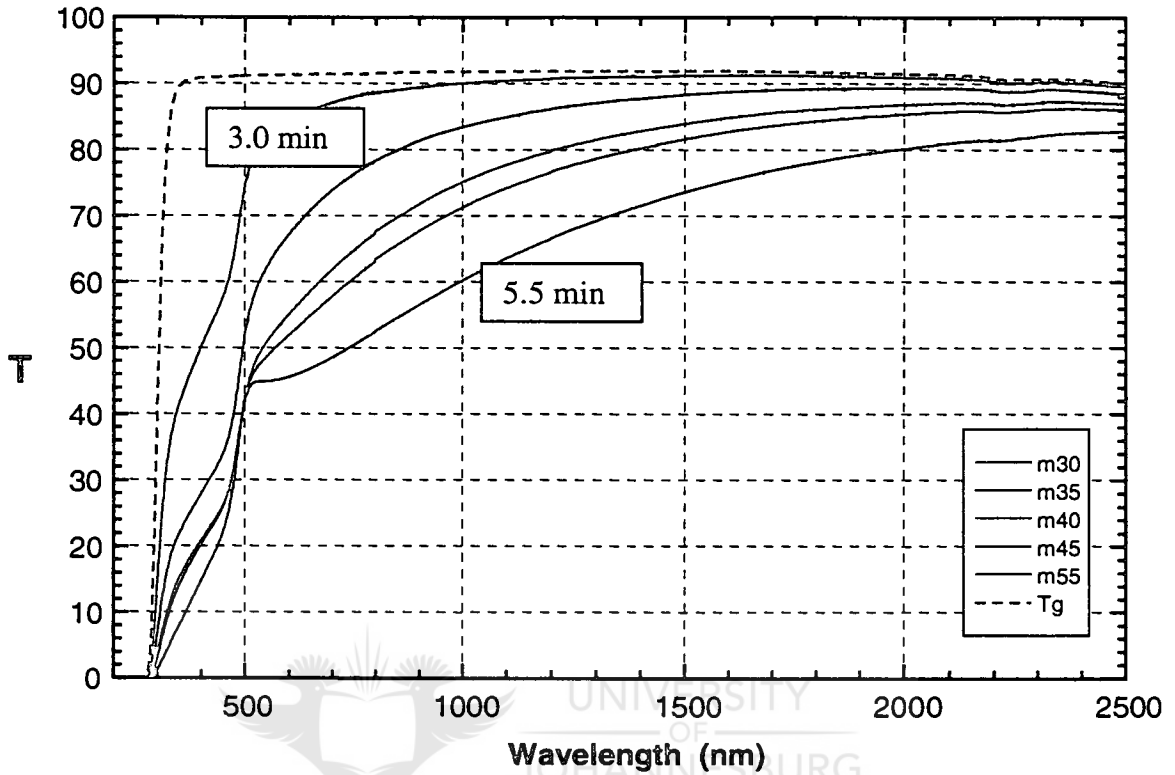


Figure 5.20: Transmission spectra of CdS films grown for different times with CBD on glass. The broken black line represents the spectrum of the glass substrate.

The non-linear behaviour of the transmission curves for wavelengths shorter than 500nm is the result of the known somewhat peculiar behaviour of  $n(\lambda)$  and  $k(\lambda)$  for CdS in this region (Palik, 1985). It is, however, clear that CdS shows strong absorption below 500nm, which will have a serious influence on the performance of CIS solar cells. The CdS layer should thus be as thin as possible. It should be noted that the thicknesses cited here are the individual thicknesses of two layers on both sides of a glass substrate. The absorption for a single layer CdS in a CIS solar cell will thus approximately only be half of that indicated in Fig. 5.19 for a corresponding thickness. Figure 5.20 also shows a large decrease in the transmission with increase in film thickness for wavelengths larger than 500nm. This should not be confused with absorption, since it is just a manifestation of the thin film interference effect. It can be seen in Fig. 5.19 that for a film with thickness of 100nm, the first interference minimum

occurs at about 900nm and that there is then again an increase in transmission for smaller wavelengths. The spectra shown in the figures must thus only be interpreted for the air/CdS/glass/CdS/air system and cannot directly be used for predictions for the ZnO/CdS/CIS system in a solar cell. The transmission into the CIS absorber of the latter system will not only depend on the optical properties and thickness of the CdS layer, but also on the optical properties and thicknesses of the ZnO film and CIS absorber material. Further study and simulations are required in order to make predictions about this somewhat more complicated system.

### **5.3.3 ZnO Material Properties**

#### **5.3.3.1 Introduction**

Transparent conductive zinc oxide (ZnO) films have recently attracted a great deal of attention due to their applications as transparent electrodes for thin film solar cells such as amorphous silicon ( $\alpha$ -Si) or copper indium diselenide ( $\text{CuInSe}_2$ ). In addition, their low material cost, relatively low deposition temperature and stability in a hydrogen plasma are important advantages for thin film applications. For thin film heterojunction solar cells, not only the absorber materials (for example  $\text{CuInSe}_2$ ,  $\text{CuGaSe}_2$ ,  $\text{CdTe}$ , etc) have to be optimized, but the properties of the window layers and contact materials also play an important role for obtaining high efficiencies. Generally, the window layer consists of a wide band degenerate semiconductor with low sheet resistance ( $R_s \leq 10 \Omega/\text{square}$ ) and high transparency ( $T \geq 85\%$ ) in the visible and near infrared wavelength range.

In this study, DC magnetron sputtering from ceramic ZnO targets was chosen as method of deposition. This technique (Section 4.5.2) produced good quality films at a relatively high deposition rate and low temperatures, once the process parameters have been optimized. The process parameters investigated in this study included the substrate position under the target, screening of the target, magnetic fields at the substrate, substrate temperature and doping of the films.

#### **5.3.3.2 Structural properties**

The structural properties of the sputtered ZnO films were critically influenced especially by the position and angle of the samples with respect to the target. A systematic study was therefore conducted in order to determine experimental conditions to produce highly

transparent ZnO thin films with optimum structural and electrical properties. In order to conduct these fundamental studies, ZnO films were deposited on glass substrates.

### **Structural properties as function of sample position and orientation**

SEM and XRD studies indicated that the sample position with respect to the target plays an important role in determining the structural quality of the ZnO films. Fig. 5.21 and 5.22 are SEM micrographs of undoped ZnO films, grown directly under the centre of the target and 80cm away from the centre, respectively.

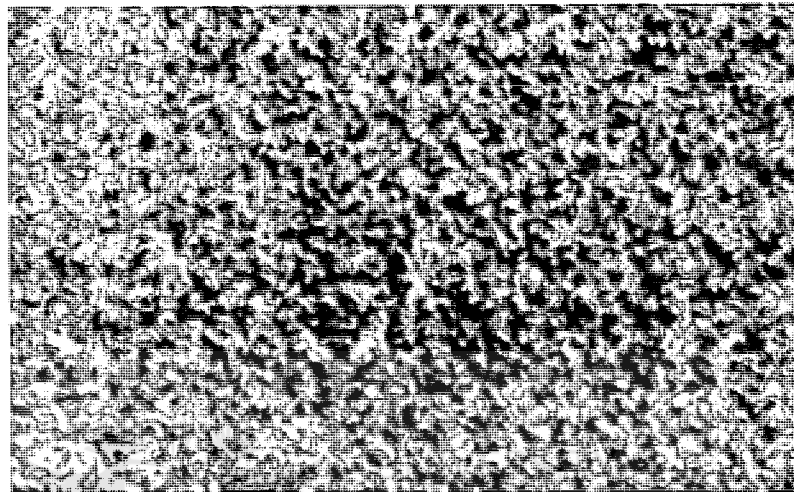


Figure 5.21: SEM micrograph of an undoped ZnO film grown right under the centre of the target. In this figure  $1\mu\text{m}$  represents  $1\text{cm}$ .

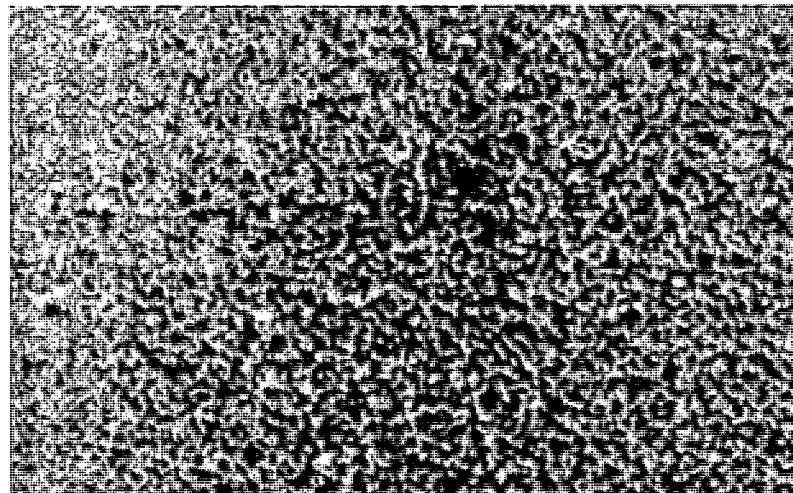


Figure 5.22: SEM micrograph of an undoped ZnO film grown 80 mm away of the centre of the target. In this figure  $1\mu\text{m}$  represents  $1\text{cm}$ .



The films deposited directly under the target were characterized by a fairly rough structure with relatively large grains. In the case of the sample deposited outside the bombardment range (Fig. 5.22), much smoother and dense films were obtained. These morphological differences, as function of sample position, were also clearly reflected by XRD studies. Fig. 5.23 show the XRD spectra of ZnO samples in different positions with respect to the target.

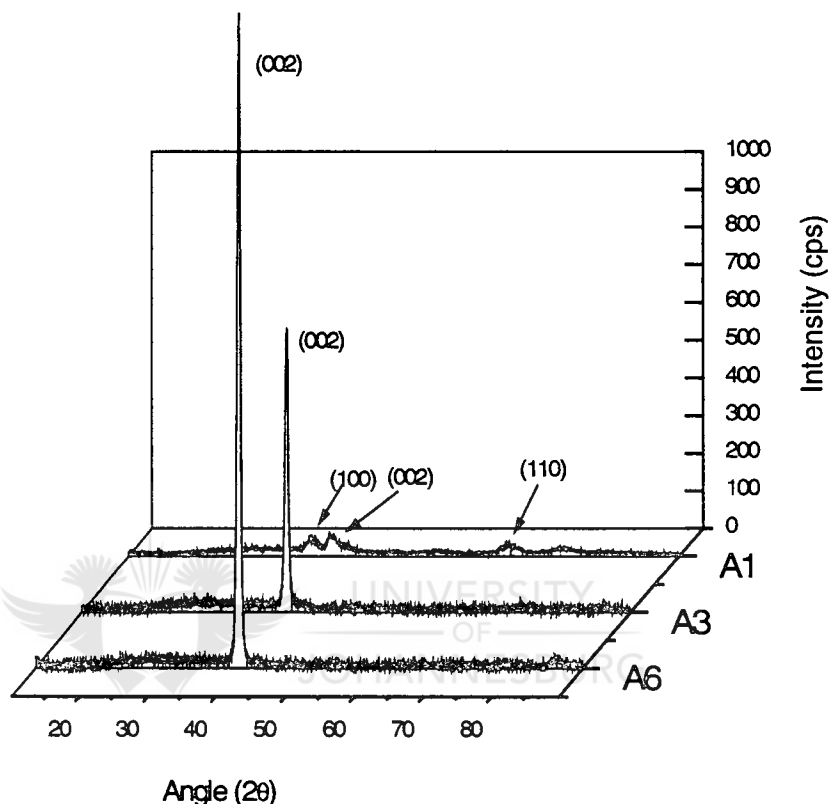


Fig. 5.23: XRD patterns of ZnO films grown under the centre of target (A1), 50mm away from the target centre (A3) and about 80mm away from the target centre (A6).

It is clear that film A1 (right under the center of the target) does not display a preferred orientation with weak lines from several planes present. At a position 50mm away from the centre of the target (A3), the (002) orientation becomes predominant, but still with relatively low intensity. At position A6, the (002) line is very strong with the other orientations almost completely absent. It is clear from these studies that films deposited at positions directly underneath the erosion zone were damaged by bombardment of electrons and negative oxygen ions, while good polycrystalline material was obtained at positions outside the erosion zone of the target.

The influence of the sample orientation on the structural properties of the ZnO films was also investigated by XRD. Fig 5.24 depicts XRD patterns, obtained from ZnO samples, deposited 50cm away from the centre of the target zone. The samples were oriented in a horizontal flat position, at an angle of  $10^\circ$  and vertical upright ( $90^\circ$ ) with respect to the target. In all three cases, relatively strong (002) preferred orientation were observed. The intensity of the (002) line was the strongest in the case of samples positioned at a  $10^\circ$  angle with respect to target. The appearance of the (004) peak in the case of these samples is a further indication of high crystalline quality.

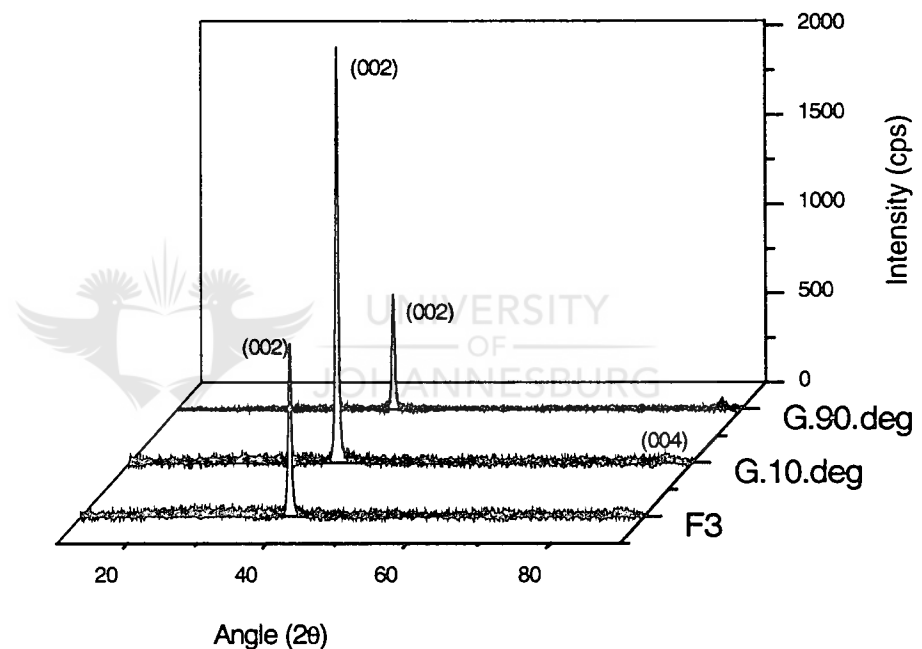


Figure 5.24: XRD patterns of ZnO films as function of different orientations in the plasma: F3 represents the flat position, the middle pattern the  $10^\circ$  orientation and the top pattern the  $90^\circ$  orientation (vertical).

### Structural properties as function of substrate temperature

Figure 5.25 shows the XRD spectra of films deposited at different substrate temperatures ( $25^\circ\text{C}$ ,  $100^\circ\text{C}$ ,  $125^\circ\text{C}$ ,  $150^\circ\text{C}$  and  $200^\circ\text{C}$ ). It is clear that the substrate temperature does not have a significant influence on the structure of the films. All films exhibited a strong to very

strong (002) peak and thus display good structural quality. From the literature it is known that considerable structural changes can take place at temperatures higher than 200°C, but this temperature range was not investigated in this study.

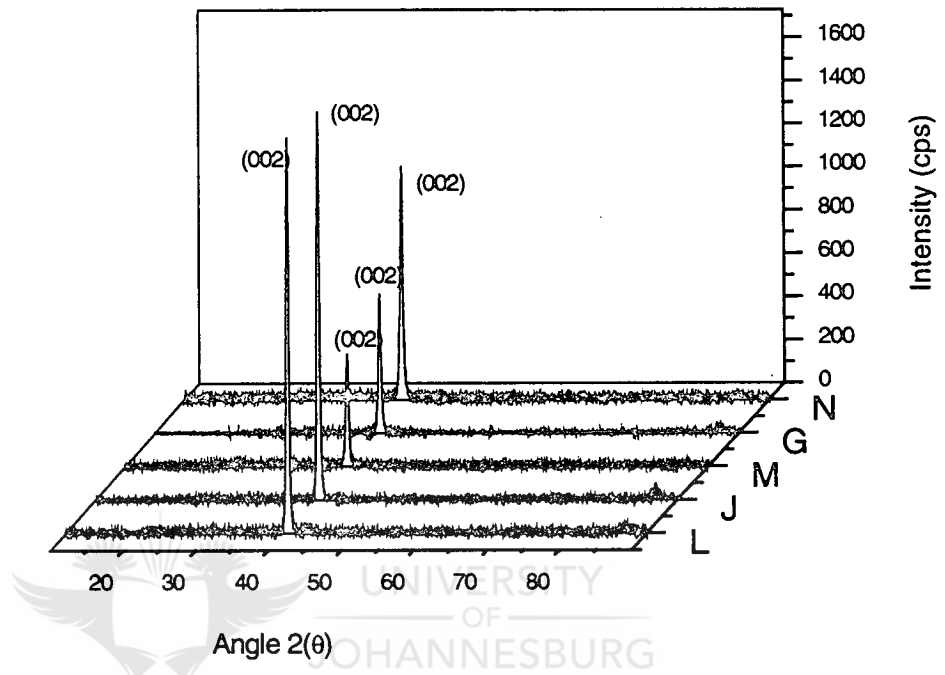


Figure 5.25: XRD patterns of ZnO layers grown at different substrate temperatures, from room temperature (N) up to 200°C (L).

### Structural properties as function of screened target

Due to the bombardment damage of the ZnO films deposited right under the centre of the target, attempts to screen the target were performed by placing a small (15 mm diameter) grounded screen a few millimeters below the center of the target. Figure 5.26. shows XRD spectra of the ZnO films deposited without the screen (A1) and with the screen (B1). A magnetic field was also applied at the substrate by placing a strong permanent magnet at various positions under the substrate. Spectrum E1 in Fig. 5.26 shows the XRD spectrum from one of these films. The attempt to screen the target or apply a magnetic field to the plasma above the substrate did not influence the structural properties of these specific ZnO films. It is clear from these results presented in Fig. 5.26 that no preferred orientation could be

obtained and that the structural quality of these layers, deposited directed under the erosion zone, were still inferior.

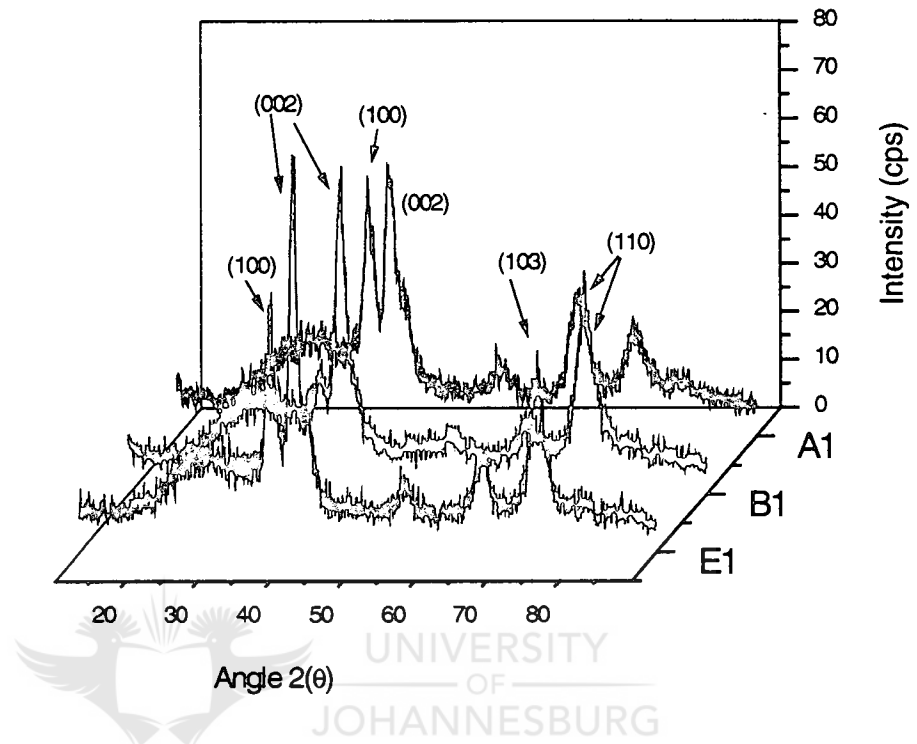


Figure 5.26: XRD patterns of ZnO films deposited right under the center of the target: unscreened (A1), screened (B1) and with external magnetic field (E1).

### 5.3.3.3 Electrical Properties

The electrical behaviour of doped and undoped ZnO films was studied by four-point probe and Hall measurements. Figure 5.27 shows the dependence of resistivity  $\rho$  versus distance  $d$  from the center of the target. All the samples were placed in a horizontal orientation with respect to the target. Samples A, B, E and F represent undoped ZnO layers, while samples C and D are Al doped films. These results clearly indicate that the electrical properties are influenced, not only by doping, but also by the position of the samples with respect to the target. In the region close to the erosion zone (0-20mm), undoped samples were non-conductive. In the same region, doped samples (samples C and D) were fairly conductive with resistivities varying between  $2.1 \times 10^{-2}$  and  $5.0 \times 10^{-3} \Omega \text{ cm}$ .

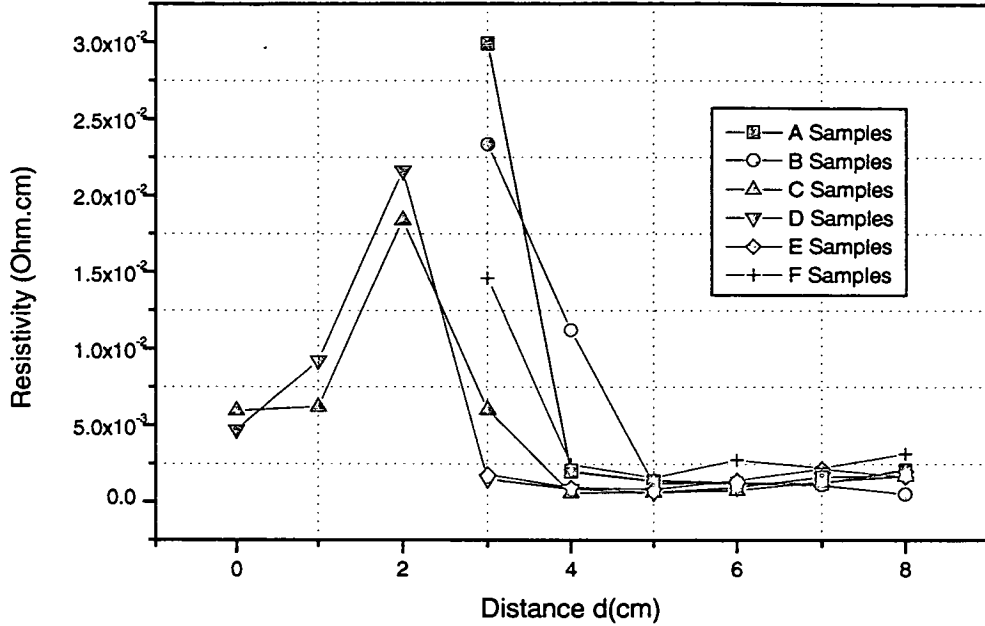


Figure 5.27: Resistivity of samples grown in horizontal positions as function of distance from the center of the target. The data were collected by four-point probe measurements.

The relatively poor electrical properties of especially doped samples in this sputtering region are most probably related to bombardment damage. It is also important to note that the electrical properties of both types of films (doped and undoped) changed significantly in the region 40 to 80mm away from the centre of the target. In both cases relatively low resistivity values between  $0.5 \times 10^{-3} \Omega\text{cm}$  to  $2.0 \times 10^{-3} \Omega\text{cm}$  were obtained. This relatively good conductivity of the undoped samples is unexpected and is most probably related to extensive defect doping (e.g. oxygen) during sputtering.

The electrical properties of the ZnO films were studied in more detail by Hall measurements. The Hall data from 5 different samples are summarized in Table 5.7. All samples were placed at a distance of 75mm away from the centre of the target zone in order to prevent bombardment damage. Samples 1 to 4 were vertically upright, while sample 5 was mounted at an angle of 10 degrees. The substrate temperature was varied from  $100^\circ\text{C}$  to  $200^\circ\text{C}$ , as indicated in Table 5.7.

<i>Parameter</i>	<i>Sample 1</i>	<i>Sample 2</i>	<i>Sample 3</i>	<i>Sample 4</i>	<i>Sample 5</i>
Temperature (°C)	100	125	150	200	100
Distance (mm)	75	75	75	75	75
Angle	90°	90°	90°	90°	10°
$\rho$ ( $\times 10^{-3} \Omega \text{ cm}$ )	0.77	4.45	0.95	0.72	1.59
$n$ ( $\times 10^{19} \text{ cm}^{-3}$ )	14.60	5.51	12.60	17.70	6.17
$R_H$	0.004	0.113	0.049	0.035	0.101
$\mu$ ( $\text{cm}^2/\text{V.s}$ )	55.70	25.44	51.82	48.99	63.52

Table 5.7: Electrical parameters obtained from Hall measurements for ZnO samples as function of substrate temperature and orientation.

In the case of samples deposited at room temperature there was no Hall signal, which indicated that these specific layers were non-conductive. In the temperature range between 100°C and 200°C, no significant changes were observed with most of the films showing fairly good electrical properties. The highest mobility was obtained in the case of samples, deposited at 100°C at an angle of 10° with respect to the target. All samples were n-type with low resistivity values suitable for device applications.

#### 5.3.3.4 Optical Characterization

The optical properties of the ZnO films were determined by analysis of transmission spectra, obtained by a Varian Cary 500 spectrophotometer in the wavelength range 300 to 3000 nm. This optical characterization technique was discussed in Section 4.6.3.2.

Figs. 5.28 (a) and (b) depict typical optical transmission spectra of two undoped samples, grown directly under the target and 30mm away from the centre of the erosion zone, respectively. All other deposition parameters (sputter pressure, power and growth time) were kept constant. Electrical measurements (Fig. 5.27) indicated significant differences between these specific samples. The optical behaviour of these samples, however, appeared similar with high transmission values around 80% in the region between 500nm and 2800nm. It is important to mention though that the thickness of the ZnO film decreased from 1680nm to 1270nm when the sample was moved away from the centre of the erosion zone.

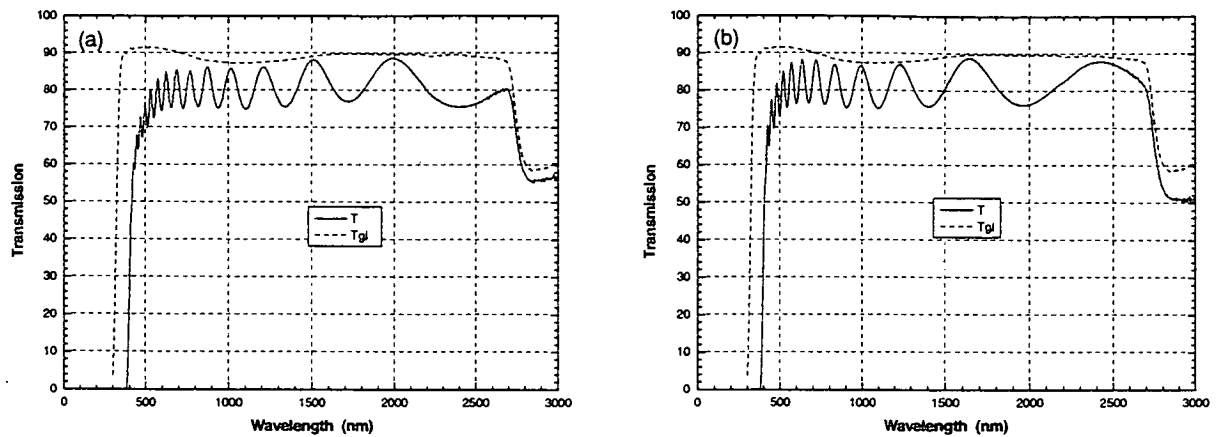


Figure 5.28: Transmission spectra of two undoped samples sputtered (a) directly under the target and (b) 30mm away from the centre of the erosion zone. The dotted red lines are the corresponding transmission spectra from clean glass substrates.

A dramatic change in the optical behaviour was observed in the case of Al doped ZnO films. Fig. 5.29 shows the transmission spectra from a doped film, sputtered under the same experimental conditions as the films shown in Fig. 5.28 (b). It is clear that there is a sharp decrease in transmission, especially in the wavelength range from 500nm to 2000nm. This change in the optical properties of ZnO with doping is expected and is attributed to an increase in free carrier absorption in the case of doped samples.

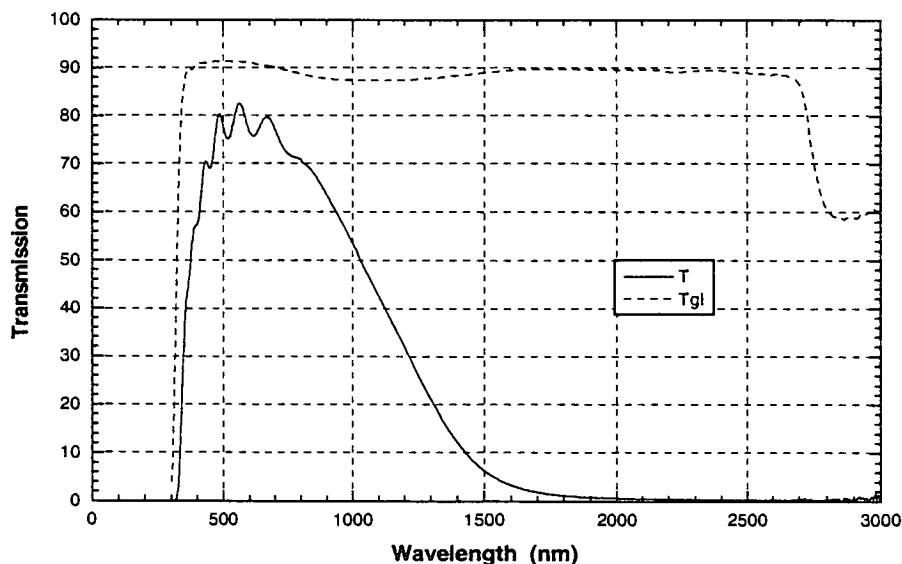


Figure 5.29: Transmission spectrum of a 2.5% Al<sub>2</sub>O<sub>3</sub>-doped ZnO film grown 30 mm away from the target center.

Using the envelope method (Swanepoel, 1981) the refractive indices were obtained for all ZnO samples grown in this study. Figure 5.30 shows refractive indices as function of wavelength for several undoped and doped ZnO films. Figs. 5.30 (a) and (c) are representative of undoped and doped samples, sputtered directly under the erosion zone. In the case of (b) and (d) the undoped and doped samples were positioned 75mm away from the centre of the bombardment region. Values between 1.65 and 2.0 were obtained in the optical region, depending on the deposition parameters.

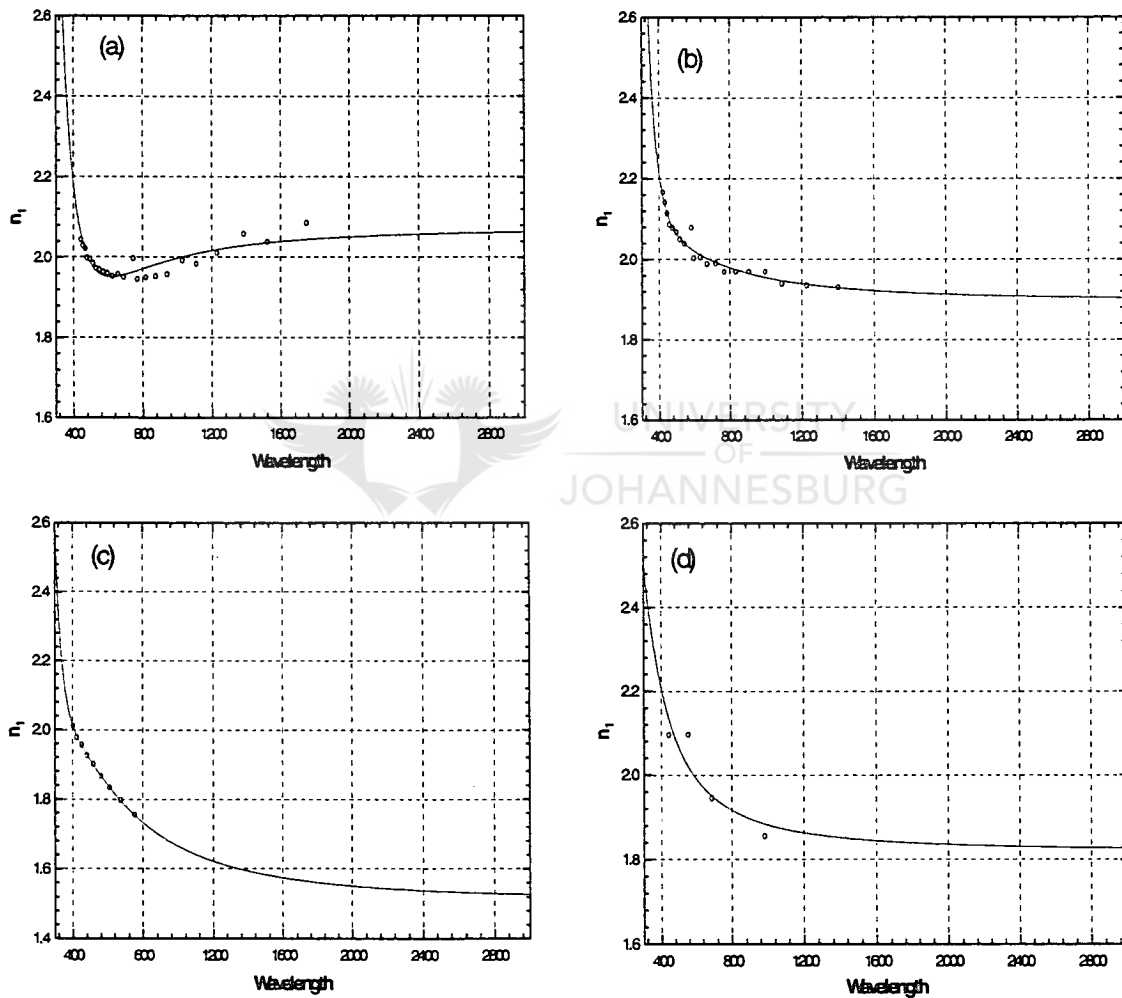


Figure 5.30: Refractive indices for undoped ZnO films deposited at a flat orientation are presented in graphs (a) and (b). The values for typical doped samples are shown in (c) and (d).



The optical bandgap values of the ZnO films were estimated by the extrapolation of the linear portions of  $(\alpha h\nu)^2$  versus  $h\nu$  curves. Figs. 5.31(a) and (b) are examples of such curves for a typical doped and undoped film, respectively. The Al-doped ZnO films displayed a significantly larger optical band gap than that of undoped films. This can be explained in terms of the effect of carrier concentration on the band gap according to the Burstein-Moss theory (Burstein, 1954). According to this theory, variations in optical gaps can be explained by a variation in free carrier concentration and the corresponding downward or upward shift of the Fermi level in the conduction band of n-type material.

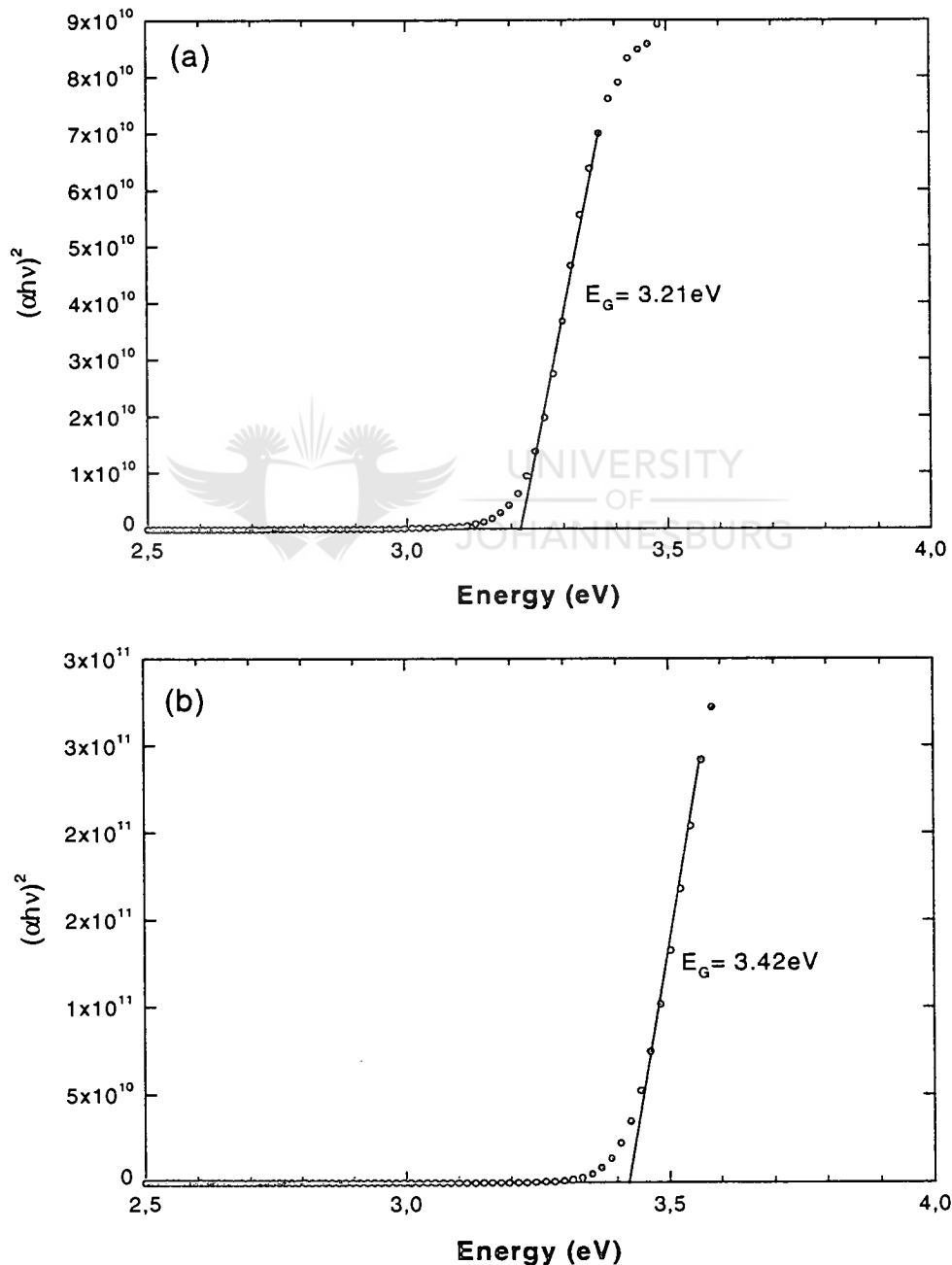


Figure 5.31: Optical band gap values for (a) undoped and (b) doped ZnO films.

## 5.3.4 Optimization of CdS/ZnO Window Layer Material

### 5.3.4.1 Introduction

CuInSe<sub>2</sub>-based solar cells require a window layer to form the heterojunction contact. It is known that the appropriate window layer for these cells is a combination of two thin films: a CdS layer and a transparent conductive oxide (ZnO) for the front contact (Tuttle et al., 1995). CdS is a very suitable buffer layer in CIS solar cells and it is prepared as thin as possible to avoid optical transmission losses. These films are generally characterized by a high sheet resistance and the deposition of a transparent conductive oxide (ZnO) film on the CdS layer is therefore necessary in order to decrease the overall sheet resistance in photovoltaic devices. Optical and electrical studies were thus performed in this work with relation to the CdS/ZnO window layer material.

### 5.3.4.2 Optical Properties

The optical transmission of the (CdS/ZnO) film on a glass substrate is shown in Fig. 5.32. These layers were obtained by the growth of a CdS film for about 5 minutes in a CBD process, yielding a film with thickness of about 50nm (Section 5.3.2). On top of the CdS layer, a ZnO film with thickness of about 0.7 $\mu$ m was deposited by DC magnetron sputtering. From the transmission spectrum it is clear that the influence of the CdS is more pronounced in the wavelength range below 500nm, showing more absorption than the ZnO film alone (i.e. there is a sharp reduction in the transmission). This phenomenon is not present in ZnO layers alone (Fig. 5.28). In the visible region, the transmission is about 55%. The optical combination of the glass refractive index ( $n = 1.5$ ), CdS refractive index ( $n = 2.3$ ) and ZnO refractive index ( $n = 1.9$ ) causes a larger reflection than in the case of ZnO on glass and is the cause for the observed smaller transmission in this region. In the case of CIS/CdS/ZnO this effect will not be so pronounced as in this case, due to the optical behaviour caused by the higher refractive index of the CIS absorber material combined with the window layer (CdS/ZnO) material. This will give solar cell devices the necessary optical properties for the solar energy conversion. In the near-infrared region of the spectrum, a reduction in the transmission is again observed compared with the optical properties of ZnO film on glass (Fig. 5.28) from about 85% (for ZnO) to about 75% for CdS/ZnO material.

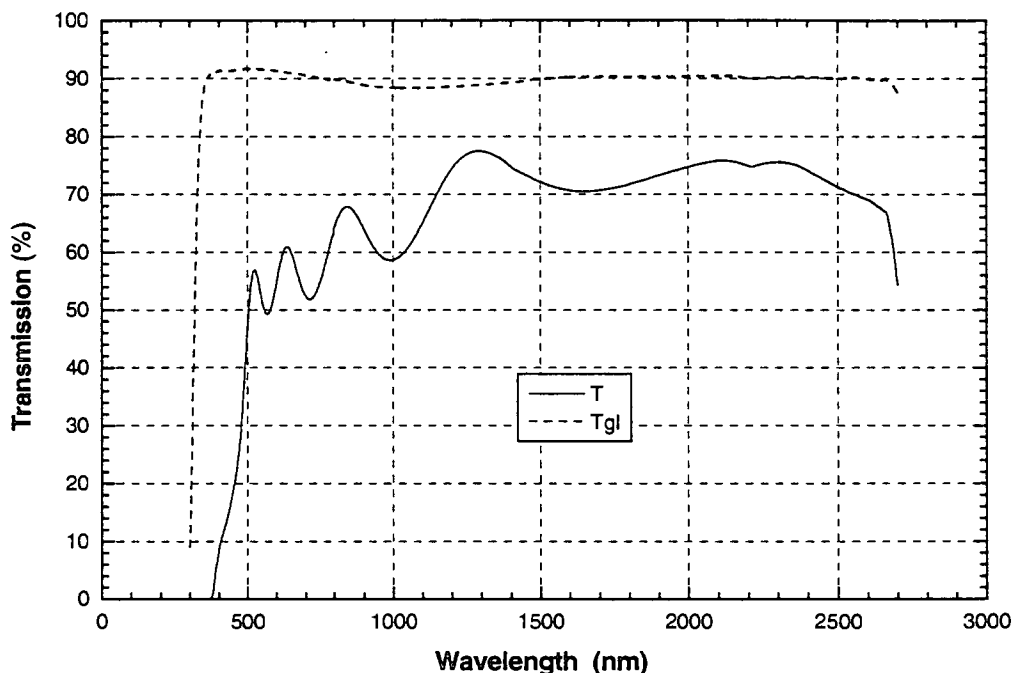


Figure 5.32: Transmission spectrum of a CdS/ZnO window layer deposited on glass.

### 5.3.4.3 Electrical properties

The electrical properties of the CdS/ZnO window layer on glass substrates were investigated by Hall measurements. Although CdS is a conductive material, the electrical properties obtained for the CdS/ZnO structure seemed to be similar to that of ZnO, with no contribution of the CdS due to the very small thickness of the CdS film (Table 5.8).

Type of film	$\rho$ ( $\Omega$ cm)	$n$ ( $\text{cm}^{-3}$ )	$\mu$ ( $\text{cm}^2/\text{V.s}$ )
CdS/ZnO	$3.85 \times 10^{-3}$	$3.65 \times 10^{19}$	44.4

Table 5.8: Electrical data of CdS/ZnO window layer from Hall measurements.

## 5.4 Device Fabrication

Preliminary  $\text{CuInSe}_2/\text{CdS}/\text{ZnO}$  heterojunction solar cells were fabricated and evaluated under A.M. 1.5 ( $100\text{mWcm}^{-2}$ ) conditions. As  $\text{CuInSe}_2$  absorber layer, a  $\text{H}_2\text{Se}/\text{Ar}$  treated  $\text{InSe}/\text{Cu}/\text{InSe}$  film was used. The material properties of this specific absorber film are

discussed in Section 5.2.3.2. The device properties of our preliminary cells are indicated in Table 5.9.

Cell No	$V_{oc}$ (mV)	$J_{sc}$ (mA cm <sup>-2</sup> )	FF (%)	$\eta$ (%)
1	513.0	40.40	72	14.8
2	459.9	33.60	66	10.2
3	354.4	16.70	42	5.0

Table 5.9: Summary of the performances from 3 cell structures. Cell 1 is the current world record cell, cell 2 was fabricated with a CdS/ZnO window layer from the University of Stuttgart and cell 3 was completely fabricated in our laboratories.

For the purpose of comparison, the device characteristics of the present world record cell (Cell 1, Stolt et al., 1993) are also included. In general, cells fabricated from Cu-rich absorber films showed no photovoltaic activity. This is attributed to the presence of segregated Cu<sub>x</sub>Se phases in these materials. In the case of very In-rich materials (Cu/In atomic ratio < 0.8), low conversion efficiencies between 1 and 2% were obtained. These cells were characterized by very low fill factors (10-20%), probably due to the high resistivity associated with very In-rich material (Table 5.5). The best results were obtained in cases where the absorbers were slightly In-rich (Cu/In atomic ratio = 0.85-0.9). In this case, cells with conversion efficiencies above 10% could be obtained (see for example cell 2 in Table 5.9). The absorber material of cell 2 was deposited in our laboratories, but the CdS/ZnO window layer was deposited at IPE at the University of Stuttgart in Germany. In the case of cell 3, the complete cell structure was fabricated in our laboratories. Identical absorber films were used in cell 2 and 3. A comparison of the cell parameters from these two devices clearly indicates that our CdS/ZnO window layer is not optimized at this stage.

## References

- U.C. Boehnke and G. Kühn (1987) *J. Mater. Sci.* **22**, p 1635.
- E. Burstein (1954) *Phys. Rev.* **93**, p 632.
- R. Klenk, H.W. Schock, D. Cahen, T. Engelhard and E. Mans (1991) 10<sup>th</sup> European PVSEC, Lissabon, p 101.
- M. Klenk, O. Schenker, U. Probst and E. Bucher (1999) *Solar Energy Materials & Solar Cells* **58**, p 299-319.
- H. Löwe, P. Keppel and D. Zach (1990) *Halbleiterätzverfahren*, Akademieverslag, Berlin, p 138-141.
- E. D. Palik (1985) *Handbook of Optical Constants of Solids*, Academic Press, London
- J. Parker, R.D. Tomlinson and M.J. Hampshire (1973) *J. Appl. Crystallogr.* **6**, p 414.
- J.R. Sites and R.E. Hollingsworth (1987) *Solar Cells* **21**, p 379.
- L. Stolt, J. Hedström, J. Kessler, M. Ruckh, K-O Velthaus and H. W. Schock (1993) *Appl. Phys. Lett.* **62(6)**, p 597-599.
- R. Swanepoel (1989) *SA Journal of Physics* **12**, p148.
- H. Tanino, T. Maeda, H. Fujukake, H. Nakanishi, S. Endo and T. Irie (1992) *Phys. Rev.* **B45**, p 13323.
- J. R. Tuttle, T. A. Berens, S. E. Asher, M. A. Contreras, K. R. Ramanathan, H. L. Tennant, R. Bhattacharya, J. Keane and R. Noufi (1995) *Proc. 13<sup>th</sup> EC Photovoltaic Solar Energy Conference*, Barcelona, p 2131.
- S.M. Wasim (1986) *Solar Cells* **16**, p 289.

## CHAPTER 6

### CONCLUSIONS AND SUGGESTIONS FOR FUTURE WORK

#### Conclusions:

The conversion efficiencies of CuInSe<sub>2</sub>/CdS/ZnO solar cell devices are critically influenced by the material quality of the thin film CuInSe<sub>2</sub> (CIS) absorber layers. In this study, attention was mainly focussed on two important aspects of research. Firstly, various novel growth schemes were investigated in order to develop a viable technological process for the production of device quality CuInSe<sub>2</sub> chalcopyrite thin films. As important, was the detailed characterization of these thin films in order to determine optimum growth parameters. In addition to these important aims, an attempt was also made to develop a standard CdS/ZnO window layer technology in our laboratories. The most important results that followed from these studies are summarized below:

CuInSe<sub>2</sub> semiconductor materials were fabricated by various two-stage growth techniques. The first step involved the preparation of various selenium containing metallic precursors by thermal evaporation, followed by a reaction step (in Se vapour, H<sub>2</sub>Se/Ar gas or rapid thermal processing) in order to produce the final CIS films. Both these stages of processing were found to be important in determining the final quality of the absorber films and therefore required careful optimization.

SEM and XRD studies clearly revealed that the structural properties of the thermally evaporated precursor alloys at 200°C are controlled mainly by the growth sequence. Other parameters such as substrate temperature, growth rate and layer thicknesses only marginally influenced the material properties of the precursors. In the case of bilayers and triple layers (InSe/Cu or Cu/InSe/Cu) in which the growth sequence was terminated with a Cu layer, fairly rough structures were obtained with clear evidence of a droplet morphology. On the other hand, well-interdiffused precursors with extremely smooth surface morphologies were obtained in cases where the growth sequence was terminated with an InSe layer (i.e. Cu/InSe

or InSe/Cu/InSe). XRD studies revealed the presence of ternary chalcopyrite peaks, indicating a certain degree of interdiffusion between the individual precursor elements.

In a first approach, the various precursor alloys were reacted to elemental Se vapour in vacuum. Relatively high processing temperatures (600°C for 60 minutes) were required to produce device quality material. Selenized InSe/Cu and Cu/InSe/Cu precursors were characterized by large, inhomogeneous grain structures with poor surface coverage. XRD studies from these layers indicated the presence of various Cu-rich binary phases, which promoted the assumption that molten CuSe acted as a flux agent for grain growth. Reaction of InSe/Cu/InSe or Cu/InSe alloys to Se vapour produced uniform and dense films with a high degree of compositional uniformity through the thickness of the layers. XRF studies revealed a small variation in composition only close to the Mo back contact. XRD studies confirmed the superior structural properties of these specific absorber films, indicating well-defined and sharp chalcopyrite peaks without any evidence of secondary phases.

Identical metallic precursors were also selenized in a mixture of H<sub>2</sub>Se and Ar gases at atmospheric pressure. In general, this selenization process was more reactive, producing single-phase material with superior structural properties at temperatures as low as 450°C. Marginal differences were observed when bilayers and triple layers were selenized. The order of InSe and Cu deposition during the precursor formation stage, again had a significant influence on the final quality of the CIS absorber films. In cases where the growth sequence was terminated with an InSe layer, a more dense structure was observed. However, it is important to point out that selenized InSe/Cu and Cu/InSe/Cu structures showed no inhomogeneous growth behaviour, as in the case when identical precursors were selenized in selenium vapour. The behaviour is attributed to the absence of a CuSe flux when precursors are selenized in H<sub>2</sub>Se/Ar at temperatures below 500°C. All selenized structures were relatively homogeneous with an average grain size around 1µm. XRF studies revealed a high degree of compositional uniformity and XRD studies indicated single-phase material in the case of slightly In-rich material. The production of CuInSe<sub>2</sub> absorbers with superior material properties at a low processing temperature around 450°C represents an important technological advantage.

In a final approach, CuInSe<sub>2</sub> absorber films were prepared by the rapid thermal processing of the thermally evaporated precursors. The total duration of this processing step was only 380s, thereby assuring a low thermal budget. A serious drawback of this specific reaction step was the inability to accurately control the composition of the films during RTP treatment. The most serious problem was the loss of Se during the fast, high temperature annealing step. It was, however, possible to compensate for these losses by covering the precursor layers with an additional 1 μm thick Se layer. XRD studies indicated a significant improvement in crystalline quality after RTP treatment, but single-phase material could not be obtained. XRF studies as function of sample depth revealed a clear separation of phases with a dramatic increase in In concentration towards the Mo back contact. This observation was confirmed by SEM studies, showing clear evidence of large, irregular grain structures (Cu-rich CuInSe<sub>2</sub> grains) superimposed on a relatively smooth background of almost pure InSe. This type of absorber film was not suitable for device application. However, it is believed that further optimization of the RTP process could result in improved absorber structures.

The opto-electronical properties of the CIS absorber films (independent of preparation method) were critically influenced by the bulk compositions of the films. Cu-rich films were characterized by very low resistivities, while very In-rich films were very resistive. In the case of slightly In-rich material (Cu/In atomic ratio = 0.85-0.9), the resistivity values varied between 20 and 40 Ω cm, which corresponded to an acceptor concentrations around 10<sup>16</sup> cm<sup>-3</sup>. The PL response from these slightly In-rich films was dominated by the presence of a single donor-acceptor pair transition around 0.95eV. This defect level was attributed to the acceptor level of a copper vacancy (V<sub>Cu</sub>) and the donor level of a selenium vacancy (V<sub>Se</sub>). An interesting result that followed from this study is that the position and intensity of this transition varied from sample to sample. This phenomenon was attributed to a variation in Se content, resulting in a variation in the density of selenium vacancies. The PL response from Cu-rich samples was dominated by two well-defined emission lines at 0.969eV and 0.942eV. Both these emission lines shifted in position with a variation in laser intensity and were therefore considered as bound to free transitions. The peak at 0.969eV was attributed to a transition from the bottom of the conduction band to a Cu<sub>In</sub> antisite, which is regarded as an acceptor site. The peak at 0.942eV was identified as a longitudinal optical phonon replica of the peak at 0.969eV.



High quality CdS buffer layers were successfully deposited by means of a wet chemical dip process. The thicknesses of the buffer layers were controlled by the duration of dipping in the chemical bath. The bath temperature was kept constant at 60°C. A non-destructive optical method was developed to determine the thicknesses of CdS films on glass substrates. It was established that the deposition rate is non-linear with time. During the initial stages of growth the growth rate was relatively slow (approximately 4nm/min), but increased significantly to above 10nm/minute once individual islands coalesced. These optical studies indicated that a dipping period of 5 minutes is required to produce 50nm thick CdS layers. The transmission of these films varied sharply, depending on the thicknesses of the CdS layers.

The material properties of ZnO window layers, deposited by DC magnetron sputtering, were studied as function of substrate position and orientation, substrate temperature and screening of the target. The structural properties of the films were critically influenced by the position of the samples with respect to the center of the target. Samples placed directly under the erosion zone displayed relatively rough structures and XRD studies revealed weak lines with no evidence of preferred orientation. Screening of the target with a grounded screen could not reduce the bombardment damage of samples directly under the target. A vast improvement in material properties was obtained when the samples were moved away from the erosion zone. In general, these films were more smooth and dense and XRD studies also indicated a strong preferred (002) orientation. Variation in the sample orientation and substrate temperature in these optimized regions did not significantly influence the quality of the ZnO films. The electrical properties of the films were also influence by the position of samples with respect to the target. In the region close to the erosion zone (0-20mm away), undoped samples were non-conductive. Doped samples were fairly conductive ( $2.1 \times 10^{-2}$ -  $5.0 \times 10^{-3} \Omega \text{ cm}$ ) in the same region. The electrical properties of doped and undoped samples improved significantly in the region 40 to 80mm away from the centre of the bombardment region. Resistivity values as low as  $0.5 \times 10^{-3} \Omega \text{ cm}$  were obtained in these regions, which are line with the reported values in literature. Undoped samples were characterized by high transmission values around 80% in the region between 500 and 2800nm. In the case of doped samples, a sharp decrease in transmission was observed, especially in the wavelength range from 500 to 2000nm. In addition, the band gap values of doped samples shifted to higher values, compared to undoped samples. This phenomena is explained in terms of the Burstein- Moss theory.

Preliminary CuInSe<sub>2</sub>/CdS/ZnO solar cell devices were fabricated and evaluated. Initial results are very promising and devices with efficiencies ranging between 5 to 10% were obtained. In the case of the 10% devices, the CdS/ZnO window layers were deposited at the University of Stuttgart. In the cases where the complete device structure was fabricated in our laboratories, the efficiency decreased to values around 5%. These results indicate that the quality of our absorber films is in line with best reported to date. The CdS/ZnO window layer technology, however, requires further optimization in order to produce above 10% devices in our laboratories.

**Suggestions for future work:**

Future attention will be focussed on the deposition of CuInSe<sub>2</sub> absorber films on large area substrates. Selenization processes, especially in H<sub>2</sub>Se/Ar gas, seem very promising for large-scale applications and will be investigated further. Another interesting possibility is the use of flexible substrates such as Mo and Kapton instead of standard glass substrates. The optimization of the CIS/CdS and CdS/ZnO heterointerfaces will also be an important focus area in future research.

